ISSN 2699-1020

Mohammad Sanayei Micromechanical modelling of piping erosion 79

RUHR-UNIVERSITÄT BOCHUM

Mohammad Hassan Sanayei

Micromechanical modelling for the analysis of piping erosion in cemented soils for suction-assisted offshore foundations

Bochum 2024

Heft 79

Schriftenreihe des Lehrstuhls für
Bodenmechanik, Grundbau und Umweltgeotechnik

Herausgeber: Torsten Wichtmann

ISSN 2699-1020

Ruhr-Universität Bochum
Schriftenreihe Bodenmechanik, Grundbau und Umweltgeotechnik
Heft 79

Herausgeber:
Prof. Dr.-Ing. habil. Torsten Wichtmann
Ruhr-Universität Bochum
Fakultät für Bau- und Umweltingenieurwissenschaften
Lehrstuhl für Bodenmechanik, Grundbau und Umweltgeotechnik
44801 Bochum
Telefon: 0234/ 3226135
Telefax: 0234/ 3214236
Internet: www.bgu.ruhr-uni-bochum.de

ISSN 2699-1020

Aix*Marseille université
Socialement engagée

RUHR UNIVERSITÄT BOCHUM
RUB

FAKULTÄT FÜR BAU- UND UMWELT-INGENIEURWISSENSCHAFTEN

THÈSE DE DOCTORAT

Soutenue à Aix-Marseille Université
en cotutelle avec Ruhr-Universität Bochum
le 13 décembre 2023 par

NNT/NL : 2020AIXM0001/001ED000

Mohammad Hassan Sanayei

Micromechanical modelling for the analysis of piping erosion in cemented soils for suction-assisted offshore foundations

Discipline
Sciences pour l'Ingénieur

Spécialité
Mécanique des solides

École doctorale
Sciences Pour l'Ingénieur (ED353)

Laboratoire/Partenaires de recherche
RECOVER, INRAE, Aix Marseille Univ.
BAM, Ruhr-Universität Bochum

Composition du jury

Vincent RICHEFEU MCF, UGA, France	Rapporteur
Vanessa MAGNANIMO Adj.Prof., Univ. of Twente, Netherlands	Rapporteure
Pascale AUSSILLOUS Prof., AMU, France	Examinatrice
Klaus HACKL Prof., RUB, Germany	Président
Pierre PHILIPPE DR., INRAE, FRANCE	Directeur de thése
Torsten WICHTMANN Prof., RUB, Germany	Codirecteur de thése

INRAE
la science pour la vie, l'humain, la terre

BAM

Preface of the editor

Internal erosion by pore fluid flow repeatedly led to failure of earthwork structures like dams or dikes in the past. Previous research was mainly restricted to granular soils without any bonding at the particle contacts. However, many natural granular soils exhibit some kind of cementation, e.g. due to calcite precipitation or the presence of cohesive fines. Considering the few information in the literature, the knowledge and understanding of erosion phenomena in cemented granular soils is limited so far.

This motivated the German Federal Institute for Materials Research and Testing (Bundesanstalt für Materialforschung und -prüfung, BAM) in Berlin and the French National Research Institute for Agriculture, Food and Environment (INRAE) in Aix-en-Provence to launch a scientific collaboration within the binational research project "Coupled micromechanical modelling for the analysis and prevention of erosion in hydraulic and offshore infrastructures" (COMET) funded by German Research Council (DFG) and French National Research Agency (ANR). Within this project two PhD theses have been prepared, one by Abbas Farhat at INRAE focussing on experimental research mainly supervised by Dr. Pierre Philippe, and another one by Mohammad Sanayei at BAM concentrating on numerical modeling under the main supervision of Dr. Pablo Cuéllar. The research was supported by Aix-Marseille University in France and Ruhr-Universität Bochum in Germany, leading to a binational PhD degree for both candidates.

The dissertation of Mohammad Sanayei is dedicated to the practical problem of erosion-induced failure occurring during the installation of suction caisson foundations in cemented granular soils. Suction caisson foundations are becoming increasingly popular for offshore wind turbines, because, in contrast to the conventional pile driving, their installation is not associated with the generation of large noise, and they can thus be considered as more environmentally friendly. Furthermore, in contrast to monopiles, suction caisson foundations can easily be de-installed at the end of their lifetime. The installation of the caisson foundations into the seabed is realized by the application of a suction to the inner of the caisson, as a result of pumping out water from the caisson. The progressively increasing pressure difference acting on the lid of the bucket due to the increase of the suction drives the bucket into the ground. However, the difference between the hydraulic heads outside and inside the bucket also causes seepage flow from the outer to the inner side, with upwards direction within the bucket. If the seepage forces exceed a certain threshold they may lead to erosion of the soil particles up to a localized fluidization of the granular assembly – the so-called "piping" phenomenon. In order to prevent a foundation failure during

installation due to erosion phenomena it is thus of crucial importance to design the installation process of a caisson foundation very carefully. Numerical prediction tools can support this design.

In his doctoral research Mohammad Sanayei has developed numerical tools that allow three-dimensional studies of erosion phenomena in cemented granular soils. He has applied a particle-based approach (Discrete Element Method, DEM) coupled with the Lattice-Boltzmann Method (LBM) to consider fluid flow in the pore space. The reason behind, and main advantage of, such grain-resolved "micromechanical" approach as compared to the more usual continuum-based modelling techniques is that it permits a physically sound simulation of the percolation flow and its influence on the granular soil skeleton with few model parameters and without the need of strong assumptions (e.g. concerning drag coefficients, constitutive models, etc..). The focus was laid on the 3D extension of a cohesive bond model to consider the cementation between particles, as well as the enhancement of the computational efficiency of the code by GPU and CPU parallelization. Mohammad Sanayei has validated the enhanced numerical tools by means of a comparison of his results with analytical solutions as well as the measurements in macro-scale traction experiments on biconical samples of bonded glass spheres performed in the twin doctoral thesis of Abbas Farhat, showing an overall good agreement. In his 3D DEM-LBM simulations he could qualitatively reproduce the erosion phenomena observed in a previous 2D numerical study on an embedded wall segment from the literature. His simulation results demonstrate that cementation of sandy soils can reduce piping erosion.

The numerical tools developed in the framework of the doctoral research of Mohammad Sanayei allow a closer insight into the micromechanics of erosion phenomena in cemented granular soils and are thus of value for further research on this field. Furthermore, they may support geotechnical engineers in the design of erosion-prone structures, like suction caisson foundations for offshore wind turbines during the installation process. It should be mentioned that Mohammad Sanayei has published all developed code as open source on GitHub.

Torsten Wichtmann

Acknowledgement

This thesis is the result of a collaborative effort involving the German Federal Institute for Materials Research and Testing (Bundesanstalt für Materialforschung und -prüfung, BAM) in Berlin, the Chair of Foundation Engineering, Soil and Rock Mechanics at Ruhr-Universität Bochum, and the French National Research Institute for Agriculture, Food and Environment (INRAE) in Aix-en-Provence, and it was funded by German Research Council (DFG).

Working within such a collaborative and interdisciplinary environment has enriched my PhD journey, making it both challenging and profoundly rewarding. This path has deepened my expertise in my field while imparting invaluable lessons in perseverance, critical thinking, and the pursuit of knowledge. The intellectual and personal growth I have experienced through this research has been remarkable, and it has been a privilege to contribute to the academic community.

First, I am profoundly grateful to my supervisors, Prof. Torsten Wichtmann and Dr. Pierre Philippe, for their unwavering support and mentorship throughout this journey. Their guidance has been instrumental, providing both inspiration and direction at every step.

I would like to express my sincere gratitude to my co-supervisor, Dr. Pablo Cuellar, for his invaluable guidance, patience, and encouragement throughout my PhD. His insightful feedback and constant support have been crucial to my progress.

I would also like to express my sincere appreciation to the members of my dissertation committee—Prof. Vanessa Magnanimo, Prof. Pascale Aussillous, Prof. Klaus Hackl, and Vincent Richefeu—for their time, constructive feedback, and for challenging me to expand the boundaries of my work.

I am thankful to my colleagues and fellow researchers at the Bundesanstalt für Materialforschung for fostering a collaborative environment that made this journey more enjoyable.

Last but not least, I extend my deepest gratitude to my beloved parents. Their encouragement, unwavering support, and unconditional love have been invaluable throughout this journey. I also wish to thank my family for their consistent support during the various challenges I encountered.

Mohammad Hassan Sanayei

Résumé

L'érosion par fluidisation lors de l'installation de structures hydrauliques, en particulier au niveau des caissons de succion, pose d'importants défis. Ces caissons de succion sont de plus en plus utilisées pour la mise en place d'éoliennes off-shore et cette nouvelle technique d'installation présente de nombreux avantages par rapport aux méthodes traditionnelles. L'objectif de cette thèse est d'étudier les conditions d'initiation d'une fluidisation localisée dans le sol de l'installation d'un caisson de succion, en se focalisant sur les sables cohésifs et non cohésifs. Pour cela, nous avons développé un modèle numérique couplé solide-fluide en utilisant la méthode des éléments discrets (DEM) pour simuler les constituants solides et la méthode de Boltzmann sur réseau (LBM) pour simuler le fluide. Cette approche nous permet de simuler chaque particule individuellement ainsi que l'écoulement fluide environnant, ce qui est indispensable pour l'étude locale de la fluidisation des grains. Des recherches antérieures sur ce sujet indiquent que les effets de stratification ou de cémentation dans les fonds marins sablonneux ne sont pas encore bien compris, en particulier en ce qui concerne l'initiation de fluidisation locale, et qu'ils doivent donc être étudiés plus en détail. Dans cette étude, nous avons étendu à 3D un modèle de cohésion déjà fonctionnel à 2D. Dans un premier temps, nous avons testé le nouveau modèle de cohésion et évalué ses performances en comparant la déflexion des particules collées en collier à la prédiction issue de la théorie des poutres de Timoshenko. Après avoir validé avec succès les tests initiaux, nous avons fait passer notre modèle au niveau supérieur en introduisant des scénarios plus complexes. En particulier, nous avons développé un modèle numérique dans une configuration d'essai de traction macroscopique. Nous avons ensuite créé plusieurs tailles d'échantillons et comparé ces résultats numériques avec des résultats expérimentaux réalisés à l'unité RECOVER (INRAE, Aix Marseille Université). Étant donné que la génération d'échantillons de grande taille peut s'avérer coûteux en temps de calcul, nous avons amélioré notre modèle grâce au calcul parallèle, en utilisant la puissance d'un cluster de CPU (basé sur le modèle fork-join) et de nombreux threads sur un GPU, le tout en programmation C/CUDA. Une fois que le modèle a été validé par de résultats réalistes, nous l'avons intégré dans une plateforme logicielle libre appelée waLBerla. Cela nous a permis de coupler ce modèle purement DEM à un solver fluide LBM avant de finalement étudier l'occurrence de la fluidisation localisée lors de l'installation d'un caisson de succion dans des sables pouvant être cohésifs ou non cohésifs.

Mots-clés : Caisson de succion, érosion par fluidisation localisée, cohésion, DEM, LBM, waLBerla, calcul parallèle

Abstract

Piping erosion during installation of offshore foundations, particularly suction buckets, poses significant challenges. Suction buckets are increasingly being used for the installation of wind turbines and this new method of installation has many advantages compared to traditional methods. The objective of this thesis is to develop a set of micromechanical simulation tools that permit the analysis of complex coupled phenomena such as local piping erosion during the installation of suction buckets in cemented and non-cemented sands. For simulating the solid components, the Discrete Element Method (DEM) was used, while the Lattice Boltzmann Method (LBM) was employed for the fluid simulations.This approach enables to simulate each particle individually as well as the fluid flow through the void space between particles permitting the study of localized erosion. Previous research on this topic indicates that the effects of various soil layers and cementation in sandy seabeds are not yet well understood, particularly concerning the emergence of piping, and therefore require further investigation. In this study, a well-functioning 2D cohesion model was extended to 3D conditions. Initially, the newly developed cohesion model was tested and its performance was evaluated by comparing the deflections of a cantilever chain of bonded particles with predictions from Timoshenko beam theory. Afterwards, more complex models at a larger (macroscopic) scale were introduced. In particular, a numerical model was developed to reproduce the experimental data of a set of macromechanical tests on cemented granular samples under traction. Then a variety of sample sizes was studied comparing the numerical findings with actual results of experiments conducted at University of Marseille. As generating large-sized samples can be computationally demanding, the model was improved through parallel computing, utilizing the power of a CPU cluster (using the fork-join model) and numerous working threads on a GPU, with C/CUDA programming. Once the 3D cohesion model was validated and shown to produce realistic results, it was integrated into the LBM-DEM coupled framework of the academic open-source simulation platform waLBerla. This allowed coupling of the newly developed DEM model for cemented granular materials with a percolating fluid flow in 3D. Finally, some practical scenarios of a stationary bucket wall section partially embedded in either frictional or cemented sand under imposed hydraulic gradients across the wall was simulated in full 3D conditions. The simulations reproduce in essence the percolating flow and granular displacements observed in steady suction bucket tests, and also the appearance of the quicksand (piping) condition. This thesis thus provides the tools and demonstrates the promising potential of fully-resolved micromechanical simulations for addressing complex geotechnical problems.

Keywords: Suction bucket, piping erosion, cohesion, DEM, LBM, waLBerla, parallel-computing

Table of Contents

List of Figures

List of Tables

General Introduction

The main goal of this thesis is to develop a 3D coupled soil-fluid model for the analysis of local erosive phenomena during the installation of suction buckets in either frictional or cemented soils. This thesis is divided into five main chapters. The first chapter introduces a brief history and description of suction buckets. It then summarizes the findings of some relevant studies and experiments performed on the installation of these buckets in clay and sand. According to TRAN 2005, the installation in sand is emphasized as trickier compared to clay, due to the insufficiently understood behavior of sand during installation. This chapter also includes a review of the study by TRAN 2005, in which the deformation of sand during bucket installation is examined. Tran's study investigates various factors affecting sand behavior, such as soil layering, different pumping rates, and bucket geometries. Finally, the objectives of this thesis will be outlined.

The second chapter discusses the numerical models developed and used in this study, with particular emphasis on the 3D cohesion model. This model is an extension of a well-known 2D model from DELENNE et al. 2004, which has been validated in jet erosion studies, as demonstrated by BENSEGHIER 2019.

The third chapter explains the parallel computing methods employed in this study, which make the 3D model more time-efficient. The first method is C/CUDA programming, harnessing the power of the GPU and its many threads for sample generation. The second part explains the Linked-Cell algorithm, which greatly simplifies and speeds up the investigation of potential overlaps between particles, reducing the model's time complexity from $O(N^2)$ to $O(N)$. Lastly, the Fork-Join model is explained, which uses the C++ library OpenMP to enable multi-threading inside the CPU, making the simulations more time-efficient.

The fourth chapter focuses on two test cases to validate the newly developed 3D cohesion model. The first test involves reproducing the deflection approximation of a cantilever beam made of bonded particles, comparing it to other well-known models and Timoshenko's beam theory. The second test presents a more challenging scenario: the creation of a numerical model for macro traction tests, with results compared to experiments conducted at INRAE's geomechanical laboratory in Aix-en-Provence.

The fifth chapter demonstrates some capabilities of the coupled model focusing on relevant 3D scenarios of percolation flow and piping erosion underneath an embedded wall section subject to different cross-wall hydraulic gradients. It evaluates the deformation of sand within the bucket and investigates the factors leading to the formation of quicksand (piping erosion), which can cause installation failures. Finally,

the influence of the bucket's geometry on the magnitude of heave creation inside the bucket in cemented seabeds is briefly investigated.

All developments related to this study are available in a global repository on GitHub. The link to this repository can be found in SANAYEI 2023.

1 State of the art

Contents

1.1 Introduction

Offshore foundations can encounter erosion-related challenges during installation, especially in sandy seabeds. The primary focus of this thesis is to develop numerical tools that permit the exploration of one of the most important challenges faced during the installation of suction buckets, also referred to as suction caissons. As noted by RAGNI et al. 2020, these offshore foundations are a promising choice for wind turbines, which can be used either as a mono-bucket or as multi-bucket jacket structures (see Figure 1.1).

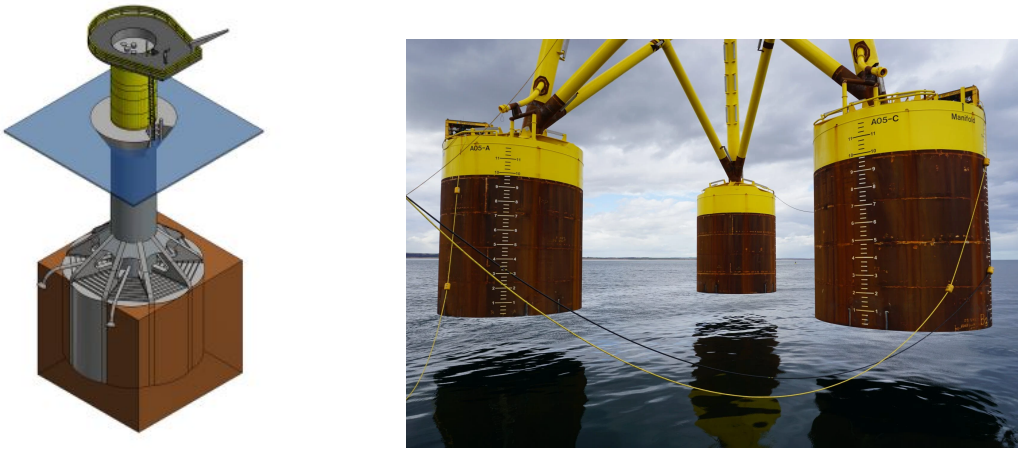

Mono-Bucket Multi-Bucket

FIGURE 1.1 – (left) Mono bucket (GONZÁLEZ 2017) ; (right) Suction buckets as part of a jacket structure (SPTOFFSHORE 2024).

This type of foundations are open-ended cylinders, closed at the top, equipped with a valve that allows for the control of water flow by adjusting the internal pressure. Compared to other methods, the installation of this foundation is more straightforward, time-efficient and environmentally friendly (low noise emissions). Initially, the bucket is lowered to the seabed, and it begins to penetrate the bed under its self-weight. Water is then pumped out of the bucket, creating a pressure difference between the inside and the outside. This pressure difference serves as the driving force, allowing the bucket to penetrate further until it reaches the desired depth (see Figure 1.2). Additionally, these foundations can be retrieved and reused through reverse pumping.

TRAN 2005 noted that installing a suction bucket in a clay bed is uncomplicated, and there's extensive research on this. However, when compared to clay layers, research on sandy soil beds is limited. RAGNI et al. 2020 mentioned that while installation in a sand bed is relatively straightforward, however, there is limited understanding regarding the changes in the soil state. Many aspects concerning the bucket's size, properties, and their impact during installation, as well as the effects of soil layering and cementation, remain under-explored. This research aims to study local erosion during the installation of suction buckets and examine the influence of soil cementation on this

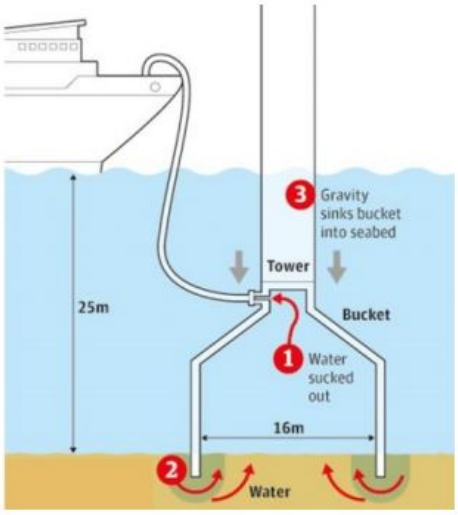

FIGURE 1.2 – How suction buckets are installed (GONZÁLEZ 2017)

process.

1.2 History & advantages of suction buckets

According to TRAN 2005, the suction bucket is still regarded as a relatively new concept, with the earliest appearance of this foundation type tracing back to the 1950s. The initial reported instance was a portable core sampler device introduced by MACKERETH 1958. This device featured a sampling tube that was lowered to the lake bottom and then retrieved using reverse pumping. Another application of this infrastructure type was noted in 1972 in the North Sea on a minor temporary scale. It wasn't until 1980 in the North Sea that suction buckets were employed on a larger scale, with 12 buckets utilized for anchoring mooring buoys. Field observations during these installations revealed excessive sand movement inside the bucket when situated in sandy seabeds. However, these applications were for temporary structures. In 1989, suction buckets were used as a permanent foundation system for the first time in the Gullfaks C platform. At the time of ANDERSEN et al. 2005 report, over 500 buckets have been installed in more than 50 locations worldwide, ranging from shallow to deep waters. Buckets are used in military applications and, as previously discussed, for offshore wind turbines either as mono-buckets or as part of multi-bucket jacket structures (see Figure 1.1).

This foundation type presents several advantages over traditional methods. As TRAN et al. 2005 mentioned, they are simple, flexible and cost-effective. The expense associated with establishing a foundation on the seabed can be categorized into three portions: (i) geotechnical investigation costs, (ii) fabrication costs, and (iii) installation costs. For both suction buckets and traditional methods, the geotechnical investigation costs remain the same. In comparison to traditional methods, while the fabrication of specialized buckets with anchoring and other unique prerequisites might

seem costlier, the installation costs for suction buckets are significantly lower. This difference not only compensates for the higher fabrication costs but also makes them more economical overall. As mentioned earlier, these structures are self-installing foundations that use their own weight and the pressure difference generated by pumping water from within the bucket. Additionally, they can be retrieved and reused in subsequent projects by reversing the pumping process.

In another study conducted by BÖHM et al. 2024, this type of foundation was compared to other methods and found to have lower weight, higher stiffness, and reduced hydrodynamic drag, making it ideal for soil conditions where monopiles cannot be installed. Furthermore, the installation of suction buckets has low noise emissions, minimizing the impact on marine mammals.

1.3 Previous installation studies

A pioneering research on suction buckets was conducted by GOODMAN et al. 1961, driven by military requirements for high mobility and rapid field development in anchorage systems. At that time, gravity anchors were popular because their bearing capacity was easy to calculate. Nevertheless, these had limitations due to their low pullout force to weight ratios which meant larger and heavier anchors were needed. In contrast, suction buckets emerged as promising candidates due to more efficient design. The study of GOODMAN et al. 1961 indicated that these vacuum systems perform effectively in clayey soils. However, in more permeable soils like sand, issues such as localized piping at the wall skirt tip could arise, leading to vacuum loss or fluidization due to increased soil permeability. Subsequent studies on this system were conducted by BROWN and NACCI 1971, and WANG et al. 1977, with Wang proposing a breakout capacity equation using the Mohr-Colomb failure theory. Initially, the primary focus of these investigations was the short-term utility of such anchorage. But from the 1980s onward, with advancements in computing technology, there was a shift toward exploring these systems for long-term use. This research mainly concentrated on two areas: (i) the installation process of suction buckets and (ii) their capacity and performance under both monotonic and cyclic loads. This lead to many numerical modelings and physical tests in standard gravity and enhanced gravity in centrifuges.

Experimental tests examined a range of soil types, from clay to sand, including layered and diverse soil compositions. Comprehensive details about these tests are available in BYRNE et al. 2002, ISKANDER et al. 2002, KELLY et al. 2004, TRAN 2005, RAGNI et al. 2020, and MA et al. 2022. Regarding numerical investigations, they can be found in the work of DENG and CARTER 2000, ZDRAVKOVIC et al. 2001, ZHOU et al. 2021, and ZHANG et al. 2024.

From this body of work, it became clear that to optimize these systems, they must be installed both accurately and effectively. The installation procedure can significantly impact the performance of the bucket. According to TRAN 2005, installing these systems in sandy soils poses more challenges than in clayey ones, mainly due to seepage flows from the outer to the inner side of the bucket (see Fig 1.2). RAGNI et al. 2020 also

mention that there is limited understanding of soil behavior during the installation of suction buckets in sandy seabed. The seepage can induce excessive heave within the bucket, leading to piping failures, as observed in the Gorm field in 1982. In that particular project, water jets were employed to mitigate heave, and this experience created a subsequent negative impact on suction caisson use in the field. As mentioned by TRAN 2005, research on sandy soils is comparatively limited, and much of the field data remains unpublished. Additionally, RAGNI et al. 2020 noted that there is limited understanding of the soil state evolution during the installation of the bucket. Thus, there is still much to learn about sandy soil behavior, necessitating further research and exploration. HOGERVORST 1980 described various field tests involving small-scale suction buckets and later, larger-scale tests with suction buckets of 3.8 m diameter and height ranging from 5 to 10 m. In his studies, Hogervorst noted that minor tilting during installation or the presence of obstacles didn't pose significant challenges. Additionally, it was mentioned that the soil inside the bucket could become liquefied during installation, leading to reduced friction between the bucket's inner surface and the soil. However, specific details about the influence of bucket size and heave characteristics during installation under different conditions were not provided.
Recent studies have also investigated the installation of suction buckets in sandy seabeds. WU et al. 2020 conducted limit analysis to estimate penetration resistance and critical suction in sand and clay. WU et al. 2018 developed methods for obtaining maximum and minimum suctions required for bucket installation in sand. ZHANG et al. 2022 investigated the installation of suction caissons in saturated dense fine sand.

1.4 Remaining issues

In previous sections, the general installation process for suction buckets was described and it was mentioned that compared to the other methods it can be considered as straightforward specially in clayey soil. However, there are several remaining issues that motivate further research and investigation. First, the pumping rate, which is the only controllable parameter during the installation, needs further investigation regarding its effect on the installation process. Second, there is limited data concerning the impact of the bucket's geometry on the installation. Third, while seepage flow plays a significant role during installation, the effects of this flow are not fully understood. Fourth, the formation of sand heave within the bucket remains not well known. It is unclear whether this formation arises from the soil's expansion inside the bucket, the interaction of the inner wall with the sand during penetration, or the inflow of additional sand through seepage flow from outside of the bucket into the bucket. In practical scenarios, the soil might be multi-layered, possibly with layers of silt or cemented sand. The presence of silt and cemented sand might hinder the water flow and the bucket's penetration, causing increased resistance to the penetration of thicker walls into the soil. Furthermore, the behavior of cemented soil and the formation of heave within a bucket in such soil is not fully understood. Several of

these issues are explored in the work of TRAN 2005 which will be explained briefly in the next sections. In the study of TRAN 2005, the behavior of both homogeneous sand and layered sand-silt mixtures was investigated during the installation of a small-scale bucket in either a normal gravity (1g) or centrifuge setup. In the following sections, the results from the 1g tests are briefly presented.

1.5 Installation behaviour at normal gravity (1g)

1.5.1 The PIV method

Particle Image Velocimetry (PIV) is an image-based technique originally developed for fluid dynamics to track object movements within fluids. In suction bucket experiments, this technique can be employed to observe heave formation within the bucket and to study soil deformation. This is achieved by capturing images of moving particles with a digital camera and then analyzing the results using specific post-processing software such as GeoPIV, a tool developed at Cambridge University. It is important to note that this method can have some inaccuracies. Being aware of these potential issues before starting an experiment can help to ensure more accurate results. More information regarding this technique can be found in the work of WHITE et al. 2003.

1.5.2 The PIV test setup

In the work of TRAN 2005, sand heave formation within the bucket was investigated using the PIV method. For this research, a half-bucket (Figure 1.3) was utilized, which had a diameter D and length of 100 mm and a wall thickness t of 1.2 mm ($t/D = 1.2\%$).

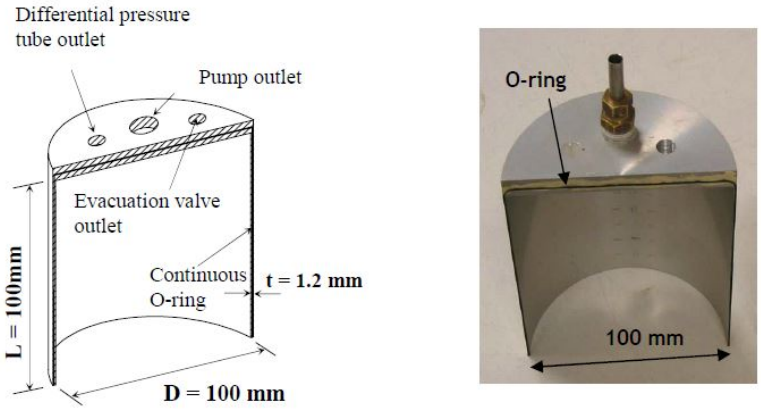

FIGURE 1.3 – Half bucket used in PIV test (TRAN 2005)

As it can be seen in Figure 1.4 the sand heave formation PIV test was carried out in a chamber with dimensions of 370 × 220 × 400 mm (width × thickness × height). A

transparent window was installed at the front of the chamber to allow the recording of soil movements. The soil sample depth was 200 mm, and the water depth was 170 mm. The bucket was positioned within the chamber using a guiding system. At the top of the bucket, a valve connected to a hose enabled the pumping out of water. The evacuated water was continuously weighed, enabling the calculation of the flow rate. Additionally, a pressure sensor was used to measure the pressure difference between the inside and outside of the bucket. Throughout the experiment, soil movements were captured every two seconds using a 4-megapixel digital camera. The results were subsequently analyzed using GeoPIV. Different tests were performed with different wall embedment. According to Tran, upon initiating a test and water pumping, soil deformation occurred almost instantly, however, no immediate signs of piping phenomena were detected.

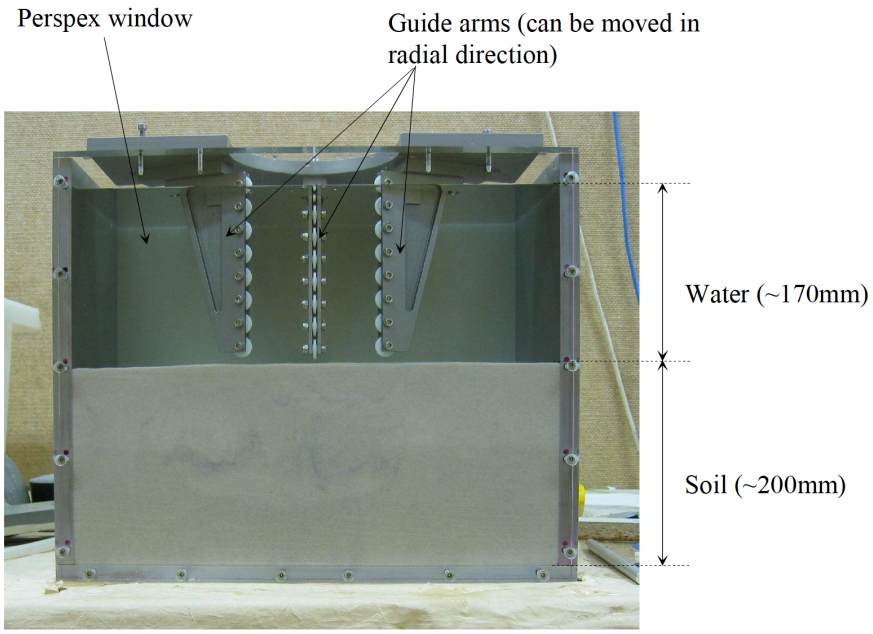

FIGURE 1.4 – Test chamber used in the PIV tests on bucket installation (TRAN 2005)

1.5.3 Soil deformation investigation

1- Installation in homogeneous silica sand

The first test series of TRAN 2005 was focused on homogeneous silica sand. The tests were conducted using three distinct bucket embedments. Initially, a setup with an embedment of $L/D = 0.1$, corresponding to a depth of 10 mm, was examined. It should be mentioned that, in this setup, the bucket stayed stationary and it could not move upward or downward. The pumping of the water started corresponding to the bucket penetration rate of 0.5, 0.8 and 1.0 mm/s. In this scenario, the upward movement (or "heave") of the sand primarily occurred near the inner wall, leaving the majority of the area with negligible movement (Figure 1.5). The normalized pressure $P/(\gamma' D)$ for this test is recorded as 0.75, where γ' is the submerged unit weight of the soil (= 10 kN/m^3),

D = 80 mm, and P is the suction pressure. Notably, this test showed minimal sand inflow from the outside to the inside of the bucket. This means the primary cause of the heave was identified as the expansion of the inner sand.

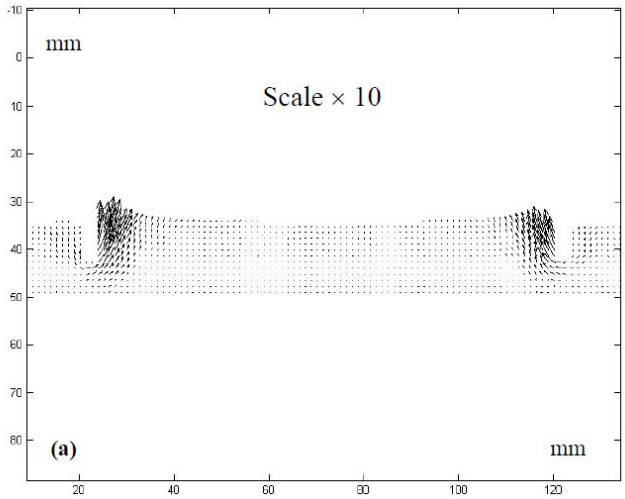

FIGURE 1.5 – Soil deformation for $L/D = 0.1$ (TRAN 2005)

Subsequent tests with embedments of $L/D = 0.2$ (20 mm) and $L/D = 0.3$ (30 mm) yielded similar observations (Figure 1.6). In these setups, the entire inner sand within the bucket moved upward. However, similar to the 10 mm embedment scenario, the most noticeable movement was concentrated near the inner wall, while the rest of the inner sand plug displayed relatively uniform displacement. The corresponding normalised suction pressures for these two cases were 4.1 and 5.1. For both these tests, minor displacements were recorded around the outer bucket wall and beneath the wall tip. All three test setups were also evaluated using higher suction pressures. The findings indicate that, even under increased pressure, there was no significant sand inflow and the majority of heave was caused by the expansion of the inner soil.

2- Layered sand-silt soil

Using the same test setup, in the second series of tests, TRAN 2005 introduced a layer of silt soil in the middle of the soil sample composed of silica sand. The test was conducted under three different conditions: (i) the bucket tip was positioned above the silt layer, (ii) the bucket tip was inside the silt layer, and (iii) the bucket tip was situated below the silt layer. Similar to the previous tests, the bucket was not able to move in any direction. In the first setup, upon applying suction, the soil around the bucket's inner wall moved upwards. However, this movement was less pronounced than that observed in homogeneous sand. Moreover, the silt layer exhibited a uniform and slight upward bend. Notably, this upward movement of the silt was confined to the area directly beneath the bucket, with no significant displacement observed in the silt layer outside the bucket's zone. The normalised suction pressure in this test was recorded as 5.77. Consistent with previous experiments, there was negligible sand inflow into the bucket. The soil deformation for this setup can be seen in Figure 1.7.

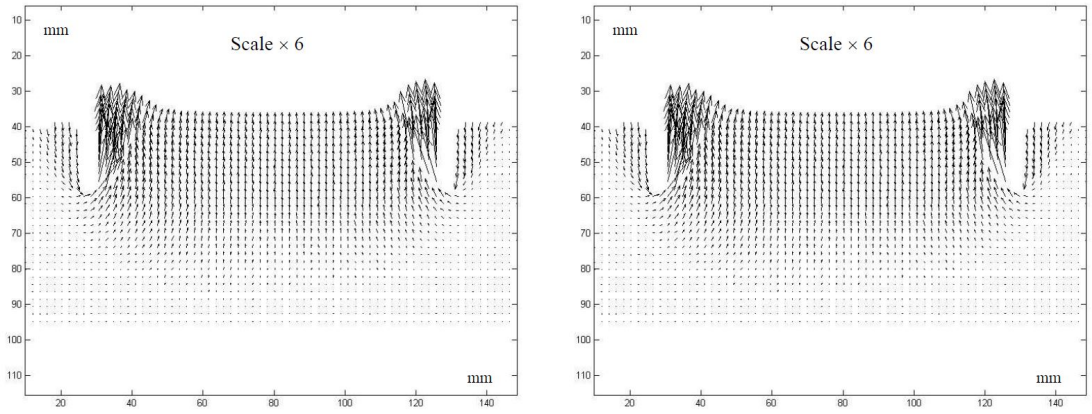

$L/D = 0.2$ $L/D = 0.3$

FIGURE 1.6 – Soil deformation for $L/D = 0.2$ and $L/D = 0.3$ (TRAN 2005)

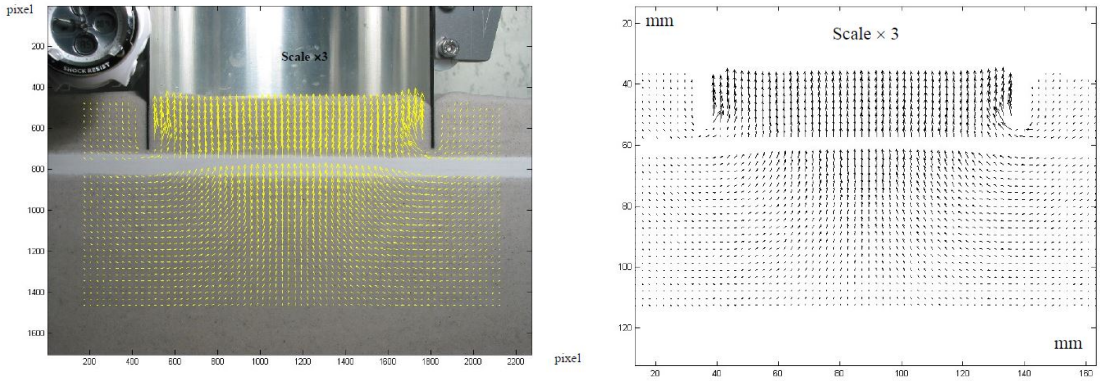

FIGURE 1.7 – Soil deformation for bucket above silt layer (TRAN 2005)

In the subsequent setup, the bucket tip was positioned inside the silt layer before suction was applied. Inside the bucket, the soil shifted upwards, with the displacement at the center being more pronounced than that near the inner wall. The silt layer also moved upwards uniformly. Given that the bucket tip was situated inside a soil type with lower permeability compared to sand, the seepage flow into the bucket decreased. The extent of sand movement observed in this scenario is quite significant, and it is unlikely to be attributed solely to seepage flow or the introduction of external soils into the bucket or internal soil expansion. Instead, it is primarily due to the upward motion of the silt layer. Displacement was also noted in the sand beneath the silt layer, forming a conical zone that extends to a depth of approximately 100% of the wall embedment. The recorded normalized suction pressure for this setup was 12.3, which was much higher than when the wall tip was above the silt layer. The soil displacement for this particular setup is illustrated in Figure 1.8.

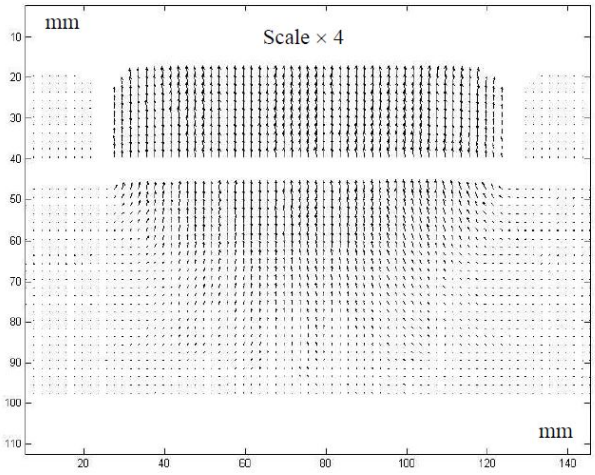

FIGURE 1.8 – Soil deformation for bucket inside silt layer (TRAN 2005)

In the final setup, the bucket tip was positioned below the silt layer, followed by the application of suction. As observed in the previous test, the silt layer within the bucket moved upwards. Additionally, sand movement beneath the silt layer was recorded, attributed to the creation of a pressure difference across the silt layer and the subsequent loosening of the sand. Furthermore, the sand located above the silt showed significant upward movement, primarily concentrated at the center of the soil plug. The normalized suction pressure for this test was recorded as 10.9, which is higher than when the wall tip was above the silt layer and slightly lower than when the wall tip was inside the silt layer. The soil deformation for this setup is depicted in Figure 1.9.

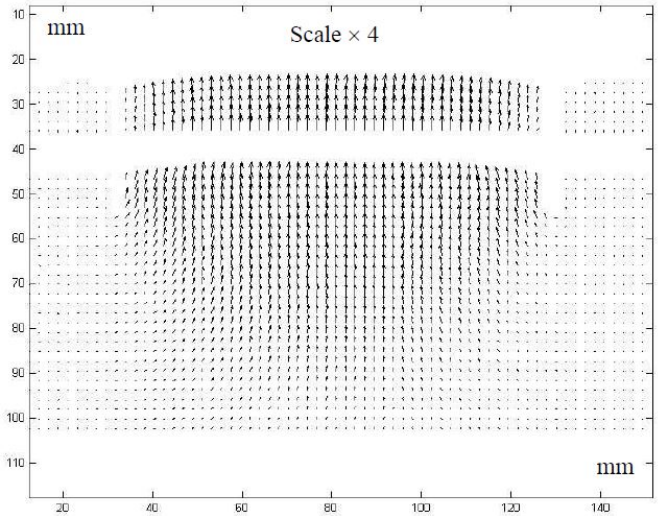

FIGURE 1.9 – Soil deformation for suction below silt layer (TRAN 2005)

3- Effect of different pumping rate

As it was mentioned in previous sections, according to TRAN 2005, the effect of different pumping rate on the installation of the buckets needs further investigation and research. In the subsequent tests, TRAN 2005 investigated varying pumping rates during the installation of the bucket (slow: 0.5 mm/s and fast: 6-7 mm/s) within homogeneous silica sand and layered sand-silt soil. In contrast to the previous test series, in these tests the bucket was allowed to penetrate into the soil.

When installing the bucket in homogeneous sand at both slow and fast rates, the process was successful with no piping incidents. The results suggest that changes in pumping rate significantly influence suction pressure, and rapid pumping might lead to a notable increase in differential pressure. As observed in Figure 1.10, when considering different bucket geometries, and using a constant pumping rate for both slow and fast installations, there is an initial sharp rise in internal suction pressure (until $L/D = 0.1$). Following this, the pressure changes linearly with the wall penetration depth. In this plot, as explained before, the pressure is represented by $\frac{P}{\gamma' D}$ where P is the measured peak pressure, γ' is the soil's buoyant (or submerged) unit weight, and D is the diameter of the bucket. Also in Figure 1.10, S1g-70-260-S refers to a 1g test for a bucket with a diameter of 70 mm and a weight of 260 grams during slow installation denoted as "S", whereas in other test cases, "F" denotes fast installation. In a related study by KIM et al. 2019, an investigation revealed a sudden and significant increase in internal suction pressure during both slow and fast installation processes. It was observed that a faster pumping rate led to higher suction pressure, but interestingly, the slope at which the suction pressure increased with embedding consistently appeared to be parallel between the faster and slower pumping rates.

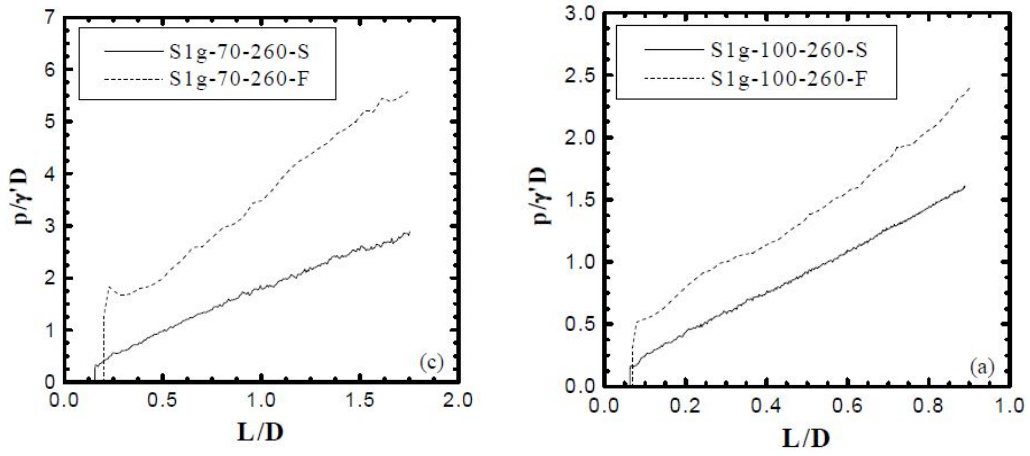

70 mm bucket 100 mm bucket

FIGURE 1.10 – Comparison of suction pressure development during slow (S) and fast (F) installations for buckets with diameters of 70 mm and 100 mm and mass of 260 grams in homogeneous sand (TRAN 2005)

Furthermore, in further tests, the pumping rate was either increased gradually or

suddenly. The results indicate that suction pressure correlates with the pumping rate's magnitude and remains unaffected by the order of changes in the pumping rate. The comparison of pressure changes due to either a gradual or sudden alteration in the pumping rate is presented in Figure 1.11. From these diagrams, it is evident that the final pressure inside the bucket is consistent with the pressure measured for the fast installations using constant pumping rate. When there is a sudden increase in pumping rate at $L/D = 0.5$, a corresponding abrupt rise in pressure is noted. Conversely, when the pumping rate rises gradually, the pressure follows accordingly.

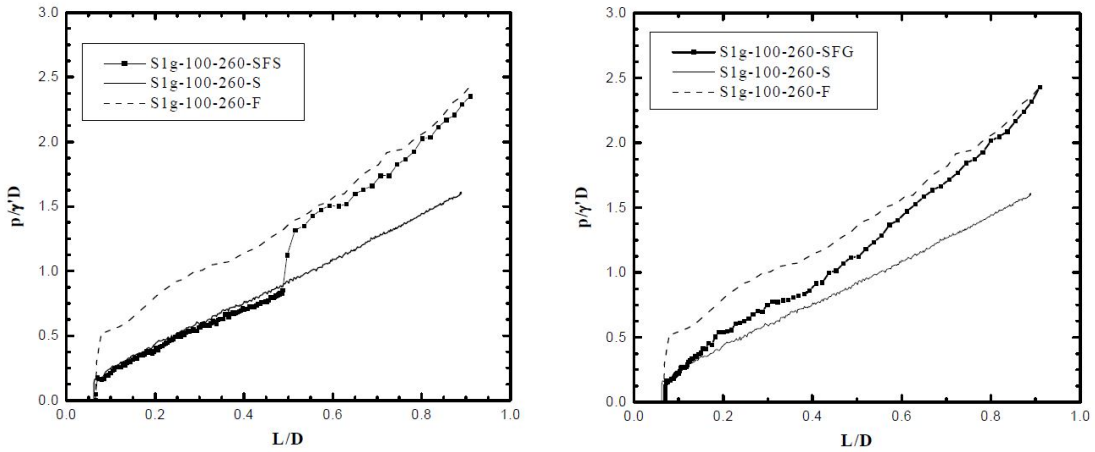

Sudden pumping rate change

Gradual pumping rate change

FIGURE 1.11 – Effects of Pumping Rate Variations: S (Slow), F (Fast), SFG (Gradual Transition from Slow to Fast), and SFS (Sudden Shift from Slow to Fast) in homogeneous sand for buckets with diameter of 100 mm and mass of 260 grams (TRAN 2005)

In layered sand-silt soil, two scenarios were examined: (i) the silt layer is at the very top, requiring the bucket to penetrate through it initially, and (ii) the silt layer is positioned in the middle of the silica sand (refer to Figure 1.12). For the first scenario, using a slow pumping rate of 0.1 – 0.4 mm/s, the bucket's penetration into the soil was unsuccessful and resulted in piping. This method was tested three times, each with the same outcome. As observed in Figure 1.13, there was an immediate rise in pressure at the start of the test, quickly followed by a decline. This decrease in pressure signals the occurrence of piping. The findings indicate that to successfully penetrate the soil, the bucket requires a greater driving force than what is achievable with the slow pumping rate.

Using a fast pumping rate of 6 – 7 mm/s for this test setup, the installation was successful. However, the generated suction pressure was considerably higher than in tests performed on homogeneous sand. This increased pressure may be attributed to hydraulic blockage caused by the silt layer at the top of the sample, resulting in increased penetration resistance for the bucket (see Figure 1.14).

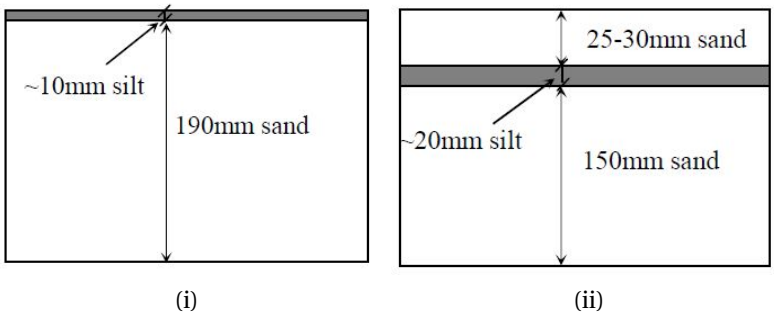

FIGURE 1.12 – Soil profile (i) and (ii) for pumping rate tests in layered soil (TRAN 2005)

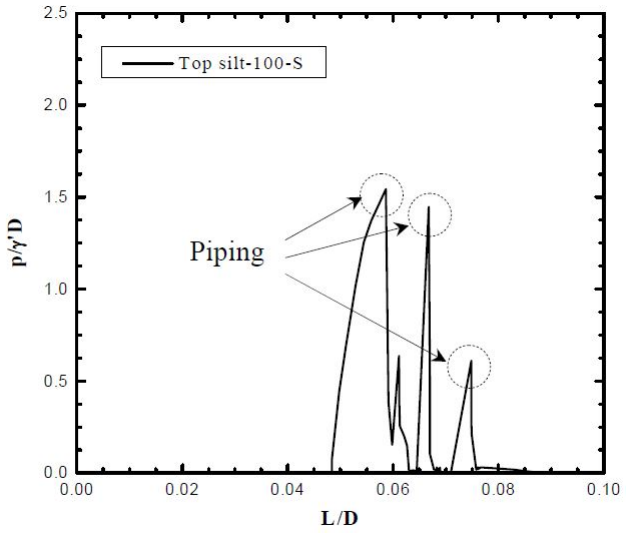

FIGURE 1.13 – Piping erosion in slow installation in soil with 10 mm silt layer at the top (TRAN 2005)

The installation continued with soil profile (ii), where a silt layer of 20 mm thickness was situated 25 – 30 mm below the top sand layer (refer to Figure 1.12 (ii)). Initially, a slow pumping method was examined. As the bucket penetrated the sand layer, the suction pressure mirrored the results observed during slow installation in homogeneous sand. However, as the bucket approached the silt layer, a greater force was needed for penetration. This requirement led to a sudden increase in suction pressure, resulting in piping failure (see Figure 1.15).

In this setup, the bucket's penetration using a fast pumping rate was also examined. Initially, the suction pressure rose linearly until it encountered the silt layer, at which point a noticeable spike was observed. This spike suggests that more force was required for the bucket to penetrate through the soil. As illustrated in Figure 1.16, after this sharp rise in pressure at the end of the silt layer, there was a swift decrease. According to Tran, this signifies a notable shift in the penetration resistance faced by the bucket.

Additionally, in another study conducted by IBSEN and THILSTED 2010, a numerical

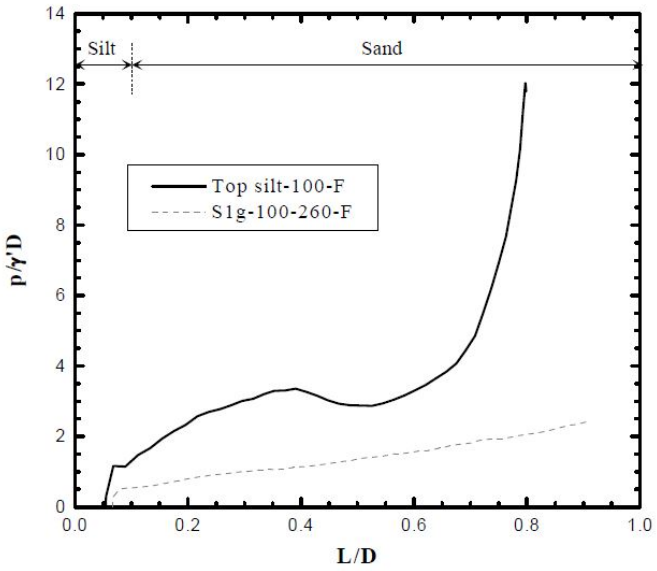

FIGURE 1.14 – Bucket penetration with diameter of 100 mm and mass of 260 grams in soil with 10 mm silt layer at the top using fast pumping (TRAN 2005)

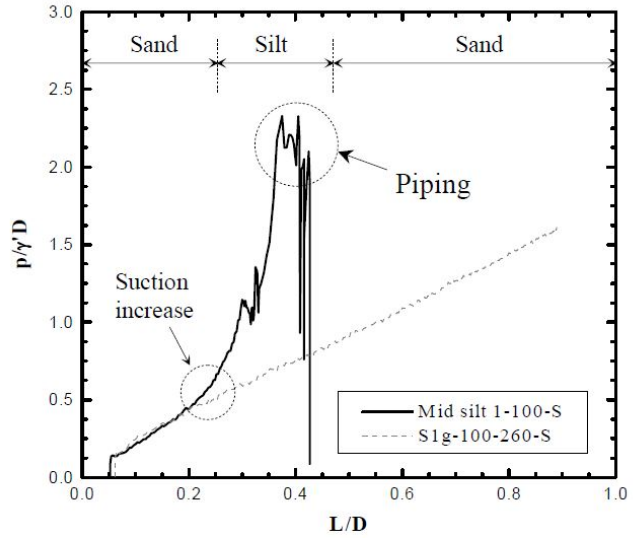

FIGURE 1.15 – Piping failure in soil with 20 mm silt layer in the middle using slow pumping for the bucket with diameter of 100 mm and mass of 260 grams (TRAN 2005)

flow analysis was carried out to investigate the installation of suction buckets in both homogeneous and layered soils. This analysis aimed to examine the development of the hydraulic gradient in response to the applied suction and explore the criteria that lead to the formation of piping channels and liquefaction of the sand inside the bucket. Based on this research, piping occurs due to the flow of water near the edge

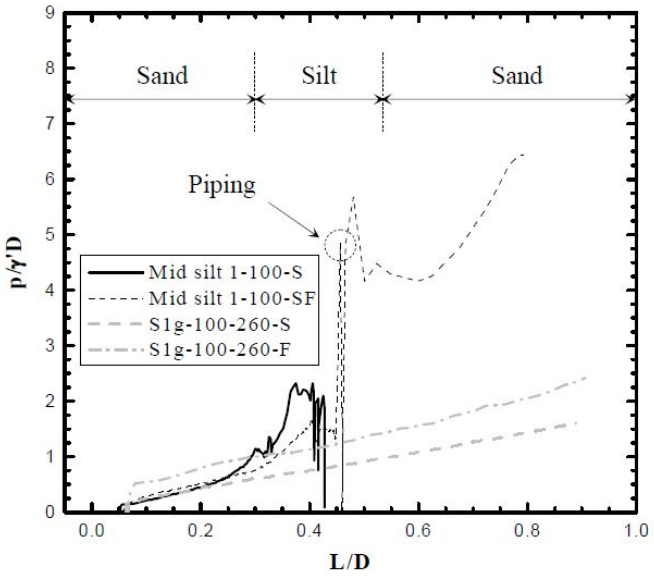

FIGURE 1.16 – Bucket penetration with 20 mm silt layer in the middle with slow and fast pumping for the buckets with diameter of 100 mm and mass of 260 grams (TRAN 2005)

and tip of the bucket. The study also highlights that the presence of a silt layer during installation can assist in preventing piping. This finding differs from the conclusions drawn in the study by TRAN 2005. This is because water doesn't easily penetrate this layer, leading to alterations in the water flow pattern at the wall's edge. Drawing from the TRAN 2005's findings, it is recommended to avoid an excessively slow pumping rate, as slow pumping can contribute to piping. As mentioned in TRAN 2005, slow pumping and slow motion of the caisson wall result in insufficient increase in effective wall cut-off, which does not prevent piping from occurring.

4- Effect of different bucket geometry

In another series, TRAN 2005 investigated the effect of different bucket geometries during installation. The tests were conducted under two different scenarios: in the first scenario (i) the bucket diameter was kept constant at 80 mm, while the wall thickness was adjusted from $t/D = 2\%$ (1.6 mm) to $t/D = 1\%$ (0.8 mm). The suction pressures during the installation of the buckets were then compared. It is important to mention that for both scenarios, the self-weight of the bucket remained the same at 2.6 N. The results in Figure 1.17, indicate that the bucket with a thicker wall required a slightly higher suction pressure to penetrate through the soil, though this difference was minimal. This could be attributed to the increased pressure required due to a larger wall tip area for the thicker bucket. For both thicknesses, the suction pressure exhibited a linear increase as the bucket penetrated the soil. In Figure 1.17, S1g-80(1.0)-260-S means a 1g test on a bucket with a diameter of 80 mm and $t/D = 1\%$, and mass of 260 grams during slow installation. Also in the study conducted by KIM et al. 2019 it was observed that thicker walls make it harder for the bucket to penetrate into the

ground because they need more pressure to break through the soil.

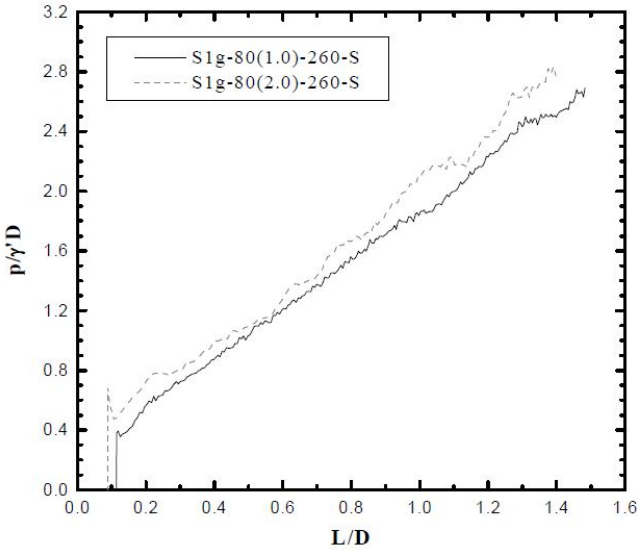

FIGURE 1.17 – Effect of wall thickness on the suction pressure for slow rate pumping for two buckets with diameter of 80 mm and mass of 260 grams(TRAN 2005)

In the second scenario (ii), while the wall thickness remained constant, the bucket diameter was altered from 100 mm to 70 mm. The impact of the varied diameter on the suction pressure was explored using a slow pumping rate. As observed in Figure 1.18, the normalized suction pressure displayed no noticeable difference. This might be attributed to the identical self-weight of the buckets. If the larger bucket were heavier, it might lead to increased suction pressure.

5- Investigation of internal heave

TRAN 2005 examined the formation of heave inside the bucket during installation and looked into various factors that could have a direct impact on it. According to TRAN 2005 the heave inside the bucket is caused by the seepage flow through the sand. Throughout performed tests, the heave inside the bucket was consistently monitored. In all installations, a consistent sand heave formation was observed. In the study conducted by TRAN 2005, further investigations were carried out to determine how different pumping rates affected heave formation. It was found that in all tests, except for those with $t/D = 2\%$, faster installation significantly reduced the internal heave. Additionally, wall thickness appeared to greatly influence heave formation. The effect of wall thickness was tested at a pumping rate of 0.4 mm/s and a self-weight of 2.6 N across all tests. As depicted in Figure 1.19, a larger heave was noticed inside the buckets with thicker walls. In Figure 1.19, the heave height is represented as h, and its ratio with the penetrated wall is calculated as h/L. In Figure 1.19, the test case S1g-70-260-S represents a 1g test for a bucket with a 70 mm diameter and a mass of 260 g. The "S" designation indicates a slow installation, whereas in other test cases, "F" denotes fast installation. In these tests, the bucket with a 70 mm diameter has a thickness of

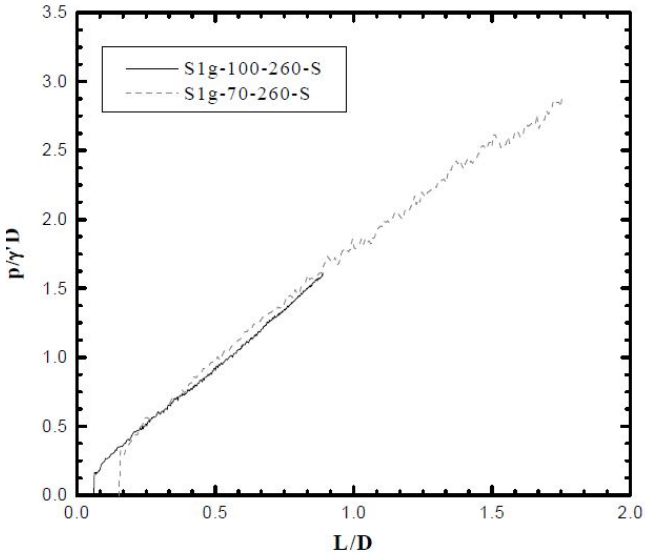

FIGURE 1.18 – Effect of bucket diameter on the suction pressure for slow rate pumping for two buckets with diameter of 100 mm and 70 mm and mass of 260 grams (TRAN 2005)

0.35 mm. In test cases such as S1g-80(1.0)-260-S, "1.0" denotes a thickness equivalent to 1 percent of the diameter, which corresponds to 8 mm. For shallow penetrations with $L/D \leq 1$, the heave ratio quickly increased with initial penetration but remained relatively stable during subsequent penetrations. The bucket with $t/D = 2\%$ showed a significantly larger heave than that with $t/D = 0.5\%$ (S1g-70-260-S).

If one assumes that all the sand displaced by the wall tip enters the bucket and that thicker walls displace more sand, the effective sand heave can be calculated by subtracting the penetrated wall volume from the total heave volume, as shown in Figure 1.19. Even after this consideration, buckets with thicker walls still produce a larger effective heave. Moreover, TRAN 2005 explored the effect of adding a surcharge to the buckets (see Figure 1.20). It was observed that applying external loads to the buckets (increasing the bucket mass) reduced the heave formation inside.
In another study conducted by RAGNI et al. 2020, it was indicated that the primary factor leading to plug heave in their experiments is attributed to the volume of soil displaced by the advancing skirts of the bucket. In contrast, the contribution of sand dilation, even in dense sand conditions, was found to be minor.

Recent studies have focused on investigating suction bucket installation in sandy seabeds. A study introducing an experimental methodology for visualizing and quantifying changes in the sandy soil state during suction bucket installation is presented in RAGNI et al. 2020. Another study examining the effects of suction pressure during installation, particularly addressing the soil heave phenomenon caused by upward seepage inside the bucket, can be found in KIM and KIM 2020. Additionally, SHENG et al. 2024 examined suction bucket installation in layered soils. A study by ZHANG et al.

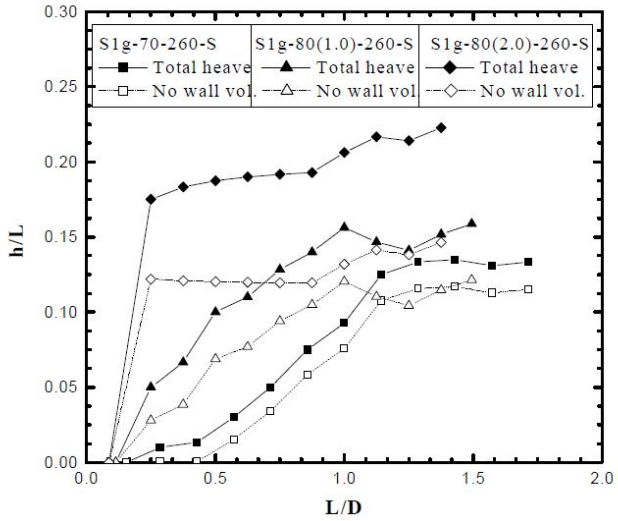

FIGURE 1.19 – The impact of wall thickness on the development of internal heave, where "S" indicates slow installation for a bucket with diameter of 70 mm and mass of 260 grams and two buckets with diameter of 80 mm and mass of 260 grams; (1.0) denotes $t/D = 1\%$ and (2.0) denotes $t/D = 2\%$ (TRAN 2005)

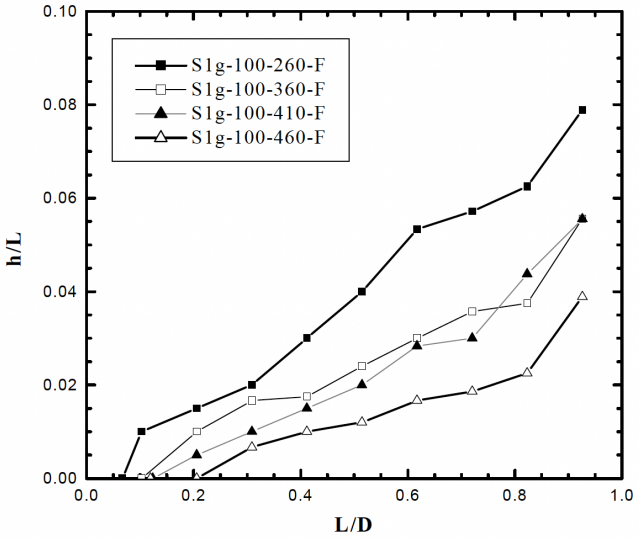

FIGURE 1.20 – The impact of surcharge on sand internal heave during fast installation for buckets with diameter of 100 mm and mass of 260, 360, 410, and 460 grams. (TRAN 2005)

2024 investigated bucket foundation installation in sand using different installation methods from a microscopic perspective.

1.6 Objectives of this study and thesis outline

As explored in the previous sections, piping may occur due to the seepage flow of water in the soil near the edges and tip of the bucket. This behavior can vary between homogeneous and layered sand. Different layers may have varied penetration capabilities, which can either facilitate or hinder the occurrence of piping, depending on the pumping rate. In this study, a set of micromechanical numerical models will be developed capable of dealing with localized piping erosion and heave formation in suction-bucket scenarios involving frictional and/or cemented granular soils. To achieve this, a granular 3D cohesion model will be introduced for the simulation of cemented sands in a DEM framework, followed by validation using macro traction tests performed at the University of Aix-Marseille (AMU). Once the model is validated, it will be integrated in the 3D open-source software called waLBerla from the FAU University of Erlangen-Nürnberg. This software is utilized for simulations coupling fluid dynamics using the Lattice Boltzmann method (LBM) with the Discrete element method (DEM) describing the mechanics of the granular particles. This framework is efficient, scalable, and optimized for high-performance computing. More information regarding this framework can be found in BAUER et al. 2021. Some first examples of bucket simulations in non-cemented and cemented sandy bed using this framework will be presented and analysed.

2 Numerical methods

Contents

2.1 Solid granular models

Solid granular models, specifically the Discrete Element Method (DEM), are numerical techniques used to model and study the movement and behavior of individual particles separately, rather than considering them as a continuous medium. The Discrete Element Method was first introduced by CUNDALL and STRACK 1979 and is derived from molecular dynamics. The DEM model describes the behavior of granular materials using Newton's equations of motion. The interactions between individual particles are governed by contact models. In these contact models, a small penetration is allowed between particles to calculate their interaction forces. However, according to LUDING 2008, the interaction force between particles is related to the overlap delta (δ) between them. The contact forces between two individual particles can be modeled using spring-dashpot systems to account for the contact deformation.

2.1.1 Equation of motion

According to LUDING 2008, the evolution of each particle in terms of position, velocity, and acceleration can be described by Newton's equation of motion. All the forces, denoted as f_i, acting on particle i, whether from boundaries or other particles, can be expressed as follows:

$$m_i \frac{d^2}{dt^2} r_i = f_i + m_i g, \quad \text{and} \quad I_i \frac{d^2}{dt^2} \phi_i = t_i \tag{2.1}$$

In this context, m_i denotes the mass of particle i, r_i represents its position, I_i stands for the moment of inertia, and ϕ_i indicates the angular velocity. The total force acting on particle i is given by $f_i = \sum_{i \neq j} f_{ij} + f_{\text{ext}}$, where f_{ij} represents the interaction force between particles i and j, and f_{ext} denotes external forces, such as those arising from fluid or interactions with boundaries. Also, the total torque is calculated from $t_i = \sum_c l_i^c \times f_i^c + q_i^c$, where q_i^c are torques resulting from rolling and torsion, and not from the tangential force, and l_i^c is the vector connecting the center of the particle with the contact point.

2.1.2 Normal contact force law

As it can be seen in Figure 2.1, the two particles i, and j are in contact where:

$$\delta = (a_i + a_j) \cdot (r_i - r_j) \cdot n, \quad \text{with } \delta > 0 \tag{2.2}$$

where $a_{i,j}$ are radii and $r_{i,j}$ are particle positions. In this equation, the contact normal is represented by $n = n_{ij} = \frac{r_i - r_j}{|r_i - r_j|}$ pointing from j to i at contact point c. Forces acting on the contact point c can be decomposed into the normal and tangential forces:

$$f^c = f_n n + f_t t \tag{2.3}$$

Using the spring dashpot model the normal force, f_n can be written as:

$$f_n = k_n \delta + \gamma_n v_n, \tag{2.4}$$

where k_n is the spring stiffness, with higher value k_n meaning more rigid particles, and a higher resistance to deformation. The damping coefficient γ_n controls the dissipation of energy, and v_n is the relative velocity between two particles, $v_n = -(v_i - v_j) \cdot n$ in the normal direction, and "." is the dot product also known as scalar product between two vectors. The damping coefficient adapted from TING and CORKUM 1992

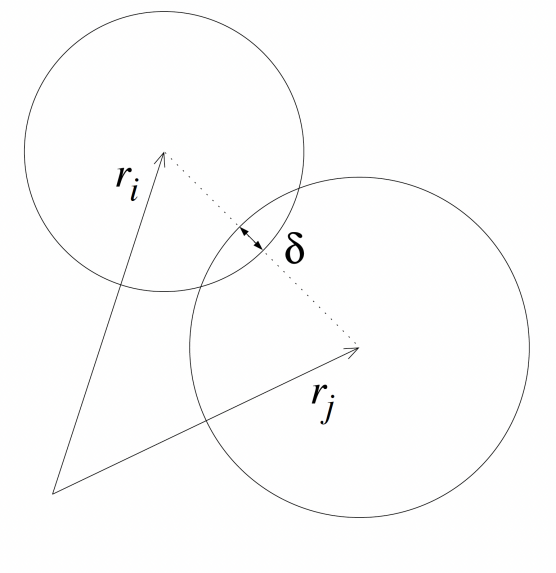

FIGURE 2.1 – Two particles in contact with overlap (LUDING 2008)

can be expressed as:

$$\gamma_n = 2\sqrt{k_n m_{\text{eff}}}\gamma \tag{2.5}$$

where k_n is particle stiffness, $m_{eff} = \frac{m_i m_j}{m_i + m_j}$ is called effective mass, $m_{i,j}$ are the masses of particles i and j, respectively, and $\gamma = -\frac{\ln(e)}{\sqrt{\ln(e)\cdot\ln(e)+\pi^2}}$. Here e is the coefficient of restitution which should be chosen between 0 and 1.

2.1.3 Tangential forces and torques

According to LUDING 2008, for the tangential degree of freedom, three different forces and torque laws have to be considered: (i) friction, (ii) rolling, and (iii) torsion resistance. To calculate forces and torques relative to sliding and static friction, the tangential velocity needs to be considered. This velocity is calculated as:

$$v_t = v_{ij} - n(n \cdot v_{ij}) \tag{2.6}$$

where v_{ij} is the relative velocity between particles, and "." is the dot product between two vectors. The relative velocity of the contact surface, v_{ij}, is calculated as:

$$v_{ij} = v_i - v_j + a'_i n \times \omega_i + a'_j n \times \omega_j \tag{2.7}$$

In this formula, for $\alpha = i, j$ (for particle i and j) a'_α is referred as the corrected radius and calculated as $a'_\alpha = a_\alpha - \delta/2$ where a_α is the particle radius and δ is the overlap between two particles, ω_α is angular velocity, and "×" is the cross product between two vectors. The tangential forces acting on particles are calculated based on the accumulated sliding at the contact point. Sliding between two particles occurs when both rotate with angular velocities in the same direction, perpendicular to the normal vector (Figure 2.2). Pure rolling happens when two particles rotate anti-parallel perpendicular to the normal vector (Figure 2.3). According to LUDING 2008 rolling velocity can be precisely determined by employing the following equation:

$$v_r = -a'_{ij}(n \times \omega_i - n \times \omega_j) \tag{2.8}$$

where a'_{ij} is the effective corrected radius calculated as $a'_{ij} = \frac{a'_i a'_j}{a'_i + a'_j}$.
This velocity activates torques on particles working against rolling motion, $q_i^{rolling} = -q_j^{rolling} = a_{ij}(n \times f_r)$ which contains the cross product of the normal vector n with rolling force f_r calculated in analogy to the tangential force. The calculation of this force will be explained later.

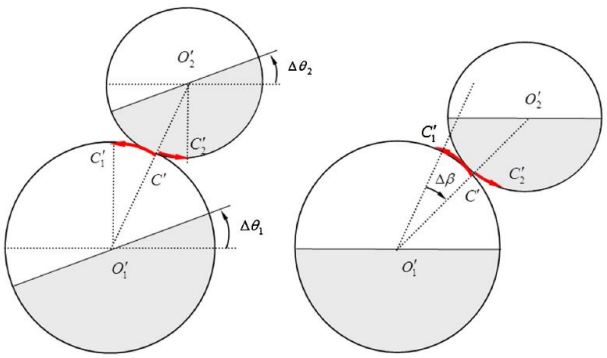

FIGURE 2.2 – Pure sliding (WANG et al. 2015)

In order to calculate the torsion on both particles (see Figure 2.4), it is necessary to consider the spin along the normal axis. The relative displacement resulting from this spin can be determined by employing the torsional velocity:

$$v_o = a_{ij}(n \cdot \omega_i - n \cdot \omega_j)n, \tag{2.9}$$

where a_{ij} is the effective radius calculated as $a_{ij} = \frac{a_i a_j}{a_i + a_j}$.
The torsion acting on both particles is of equal magnitude and applied in opposite

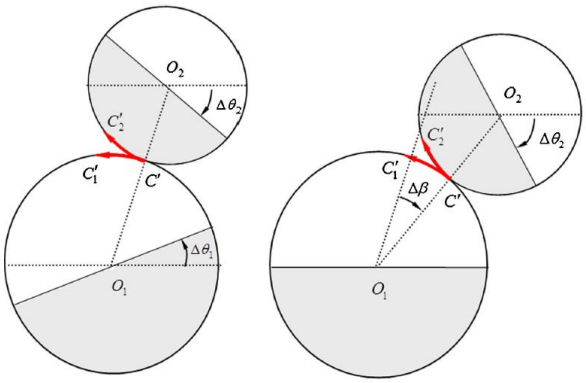

FIGURE 2.3 – Pure rolling (WANG et al. 2015)

directions. Furthermore, it can be calculated in a manner similar to the tangential force, employing the expression: $q_i^{torsion} = -q_j^{torsion} = a_{ij} f_o$.

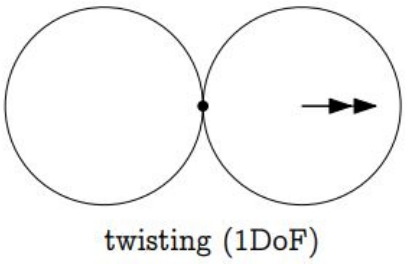

FIGURE 2.4 – Pure torsion (ŠMILAUER 2010)

2.1.4 Calculating tangential forces

According to LUDING 2008, the tangential forces and torques resulting from (i) friction, (ii) rolling, and (iii) torsion resistance applied to the particles can be determined according to a set of instructions. These instructions utilize the relative velocity between the two particles, and the resultant output will be used to calculate these forces as a function of accumulated deformations. When the contact between two particles is active, their tangential spring from the previous time step needs to be transformed to the new frame of reference using the following equation:

$$\xi_t = \xi_t' - n(n \cdot \xi_t'), \tag{2.10}$$

where ξ_t represents the tangential displacement in the current time step, ξ_t' denotes the tangential displacement from the previous time step, n signifies the normal vector, and "." is the dot product between two vectors. If the contact is new the tangential spring is initialized with the displacement of zero. After bringing the displacement to

the current frame of reference, the tangential force is determined:

$$f_t = -k_t \xi_t - \gamma_t v_t, \tag{2.11}$$

where k_t represents the tangential stiffness, γ_t denotes the damping parameter, and v_t signifies the relative sliding velocity obtained from Equation 2.6.

The tangential force, obtained through calculations, is limited to the constraints imposed by Coulomb's friction law, given by $|f_t| \leq \mu_s f_n$. Here μ_s is the friction coefficient. Hence, it can be concluded that:

$$f_t = \begin{cases} sgn(f_t)\mu_s f_n, & \text{if } |f_t| \geq \mu_s f_n \\ f_t, & \text{if } |f_t| < \mu_s f_n \end{cases} \tag{2.12}$$

2.1.5 Calculating moments and torsion

The forces associated with rolling and torsion (f_r and f_o) are computed in a manner similar to the tangential forces described in subsection 2.1.4. In the case of rolling resistance, k_r represents the rolling stiffness, γ_r denotes the rolling damping coefficient, and v_r signifies the rolling velocity obtained from Equation 2.8. Similar to the tangential force f_t the rolling force f_r can be obtained using :

$$f_r = \begin{cases} sgn(f_r)\mu_r f_n, & \text{if } |f_r| \geq \mu_r f_n \\ f_r, & \text{if } |f_r| < \mu_r f_n \end{cases} \tag{2.13}$$

where μ_r is the rolling friction coefficient. The rolling force f_r can be obtained using :

$$f_r = -k_r \xi_r - \gamma_r v_r, \tag{2.14}$$

where ξ_r is the current rolling displacement, which, similar to the tangential displacement ξ_t, is calculated using $\xi_r = \xi'_r - n(n \cdot \xi'_r)$, where ξ'_r is the previous rolling displacement.

Likewise, for torsion, k_o represents the torsional stiffness, γ_o represents the damping coefficient, and v_o denotes the torsional velocity calculated from Equation 2.9. Similar to the rolling force f_r the torsion force f_o can be obtained using :

$$f_o = \begin{cases} sgn(f_o)\mu_o f_n, & \text{if } |f_o| \geq \mu_o f_n \\ f_o, & \text{if } |f_o| < \mu_o f_n \end{cases} \tag{2.15}$$

where μ_o is the torsional friction coefficient. The torsional force f_o can be obtained using :

$$f_o = -k_o \xi_o - \gamma_o v_o, \tag{2.16}$$

where ξ_o is the current torsional displacement, which, similar to the tangential displacement ξ_t, is calculated using $\xi_o = \xi'_o - n(n \cdot \xi'_o)$, where ξ'_o is the previous torsional displacement. In this study, $\mu_r = \mu_o$, and the ratio between μ_r and μ_s is chosen based

on LUDING 2008. Additionally, the ratios between stiffnesses and damping coefficients are selected based on the literature review. These ratios are chosen similarly to the models described by LUDING 2008.

2.1.6 Integration scheme

In DEM, the size of the time step has a significant impact on the accuracy of the simulation. A smaller time step allows the numerical method to capture sudden changes in particle motions. However, in large-scale simulations, these small time steps can be time-consuming and costly. After detecting the forces applied to each particle during each time step, the linear and angular velocities and accelerations for each particle should be updated. In this study, the Velocity Verlet integration scheme, as presented by HOLM 2013, has been used. The illustration of this model can be seen in Figure 2.5. This integration scheme can be narrowed down in the following steps:

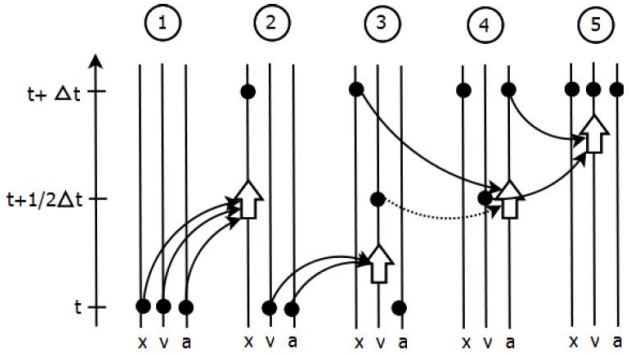

FIGURE 2.5 – Illustration of the Velocity Verlet method with x representing position, v velocity, a acceleration, and t the time step (HOLM 2013)

1. Calculate new position using: $x(t+\Delta t) = x(t) + v(t)\Delta t + 1/2a(t)\Delta t^2$
2. Calculate intermediate velocity using: $v(t+1/2\Delta t) = v(t) + 1/2a(t)\Delta t$
3. Compute the new acceleration using: $a(t+\Delta t) = F/m$
4. Calculate the new velocity using: $v(t+\Delta t) = v(t+1/2\Delta t) + 1/2a(t+\Delta t)\Delta t$

Let x denote the position, v the velocity, a the acceleration, F the force, and m the mass. For each particle at every time step, the position is first updated. Subsequently, an intermediate velocity is calculated for the particle. Using the DEM method discussed in the previous sub-sections, the force F exerted on the particle is determined, leading to the new acceleration. Finally, the new velocity is computed using this updated acceleration.

2.2 Cohesive contact law

The previously described methodology based on the Discrete Element Method (DEM) has proven to be effective in modeling frictional contacts between particles. However, the presence of cohesive bonds between particles introduces additional constraints on their motion. As illustrated in Figure 2.6, when particles are bonded, two points of cohesion, denoted as I_i and I_j, are considered. Initially, during the initial state, these points overlap (contact point of two particles) due to the particles being in close proximity. If relative rotations α_i and α_j appear, they will cause these points to separate. However, particles cannot move away from each other because of constraints imposed by the cohesive bond. In this two-dimensional context, it is crucial to calculate both the normal and tangential displacements of particles.

The normal displacement, denoted as δ_n, can be determined using:

$$\delta_n = \left|\overrightarrow{C_iC_j}\right| - (r_i + r_j), \tag{2.17}$$

where $\overrightarrow{C_iC_j}$ represents the vector connecting the center points of the particles (C_i and C_j), and r_i and r_j denote the radii of the particles (see Fig 2.6). Based on the sign and magnitude of the normal displacement, the bond can go under tension ($\delta_n > 0$) or compression ($\delta_n < 0$). Similar to the frictional model, the calculation of the normal force is performed using Equation 2.4. However, there exists a distinction between bonded contacts and frictional contacts. In the case of bonded contacts, the normal force, denoted as f_n, is computed even if $\delta > 0$, as the bond can experience tension.

Similarly, the tangential displacement, denoted as δ_t, can be calculated using:

$$\delta_t = \left|\overrightarrow{I_iI_j}\right| \cdot \vec{t}, \tag{2.18}$$

where $\overrightarrow{I_iI_j}$ represents the vector connecting points I_i and I_j (points of cohesion bond), and $\vec{t}$ represents the tangential vector perpendicular to the normal vector $\vec{n} = \overrightarrow{C_iC_j} / \left|\overrightarrow{C_iC_j}\right|$. Similar to the frictional model, the calculation of the tangential force can be performed using Equation 2.11. However, it should be noted that in the case of bonded particles, the application of Coulomb's friction law is not considered.

Furthermore, the relative rotation, denoted as α, can be computed as:

$$\alpha = \alpha_i - \alpha_j, \tag{2.19}$$

where α_i and α_j represent the respective rotations of particles i and particle j. The torques and torsion applied to the bonded particles can be calculated in a similar manner as in the case of the frictional model. This involves utilizing rolling and torsional displacements and determining the rolling and torsional forces (f_r and f_o) as explained in subsection 2.1.5.

According to RADJAI and DUBOIS 2011, the cohesion of a contact takes into account the relationship between the displacements ($\delta_n, \delta_t, \alpha$) and the contact forces (f_n, f_t, M),

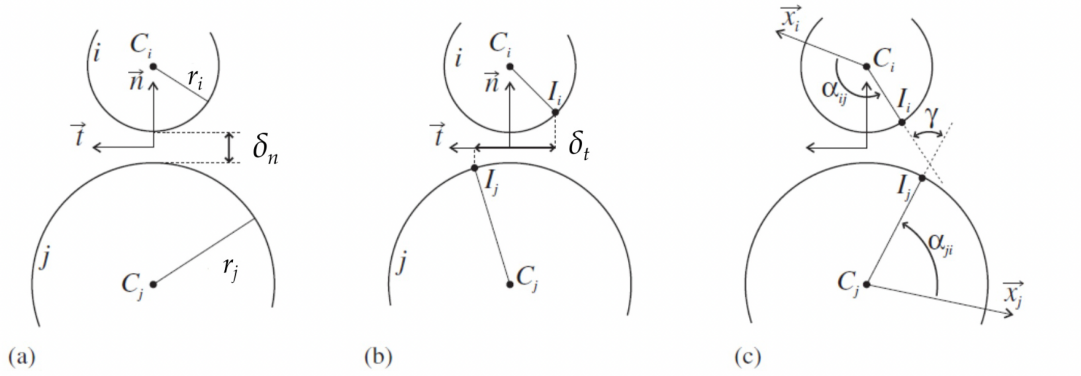

FIGURE 2.6 – Degrees of freedom at the local scale for a 2D contact: (a) local normal displacement (b) tangential displacement, and (c) rotation (DELENNE et al. 2004)

where M represents the torque applied to the contact point. This relationship can be expressed as follows:

$$(f_n, f_t, M) = \psi(\delta_n, \delta_t, \alpha), \tag{2.20}$$

Here, ψ represents the cohesion law, which defines the dependence of contact forces on the corresponding displacements. It characterizes the cohesive behavior between particles.

As the particle interactions progress, there is the possibility for a local failure, resulting in a transition from the cohesive contact law to the frictional contact law. This transition occurs as the cohesive forces are no longer able to maintain the integrity of the contact, leading to the bond breakage and emergence of frictional forces between the particles. The failure of cohesive bonds can occur due to tension, shear, bending, and later torsion is considered. To account for the combined effect of these forces on bond failure, the parabolic shape failure criterion, based on the work of DELENNE et al. 2004, is utilized (see Figure 2.7). This criterion considers the combined effect of each force on the bond failure.

The parabolic shape failure criterion offers a method to determine the bond failure metric by considering the geometric shape (orientation of the bonds), as well as the applied forces. It helps to prescribe the bond's resistance to failure under different loading conditions. As explained before the bond might break because of tension and not compression. According to RADJAI and DUBOIS 2011, the failure thresholds of the bond in compression are significantly higher compared to tension, and it is possible to set the compression threshold to infinity. The parabolic yield surface was found to accurately fit the data utilized in numerical models (RADJAI and DUBOIS 2011). Therefore, the mathematical representation of the yield surface in 2D is given by the equation:

$$\kappa = \left(\frac{f_t}{f_t^c}\right)^2 + \left(\frac{M}{M^c}\right)^2 + \left(\frac{f_n}{f_n^c}\right) - 1, \tag{2.21}$$

As long as the criterion fulfills $\kappa < 0$, this indicates the presence of a cohesive bond

between the considered particles. On the other hand, if $\kappa \geq 0$, the bond between the two particles is considered broken, and starting from that time step, their interaction is treated as purely frictional. In this formula, f_t^c, M^c, and f_n^c represent the bond tangential, torque, and normal thresholds, respectively.

In the 3D case, this study takes into account the influence of torsion in the failure criterion of the bonded particles. In this case, the parabolic hyper surface is used, and Equation 2.21 can be reformulated as follows:

$$\kappa = \left(\frac{f_t}{f_t^c}\right)^2 + \left(\frac{M_r}{M_r^c}\right)^2 + \left(\frac{M_o}{M_o^c}\right)^2 + \left(\frac{f_n}{f_n^c}\right) - 1, \tag{2.22}$$

where M_r, M_o are rolling and torsion moments calculated based on f_r and f_o (explained in subsection 2.1.4) and M_r^c and M_o^c are rolling and torsion thresholds, respectively.

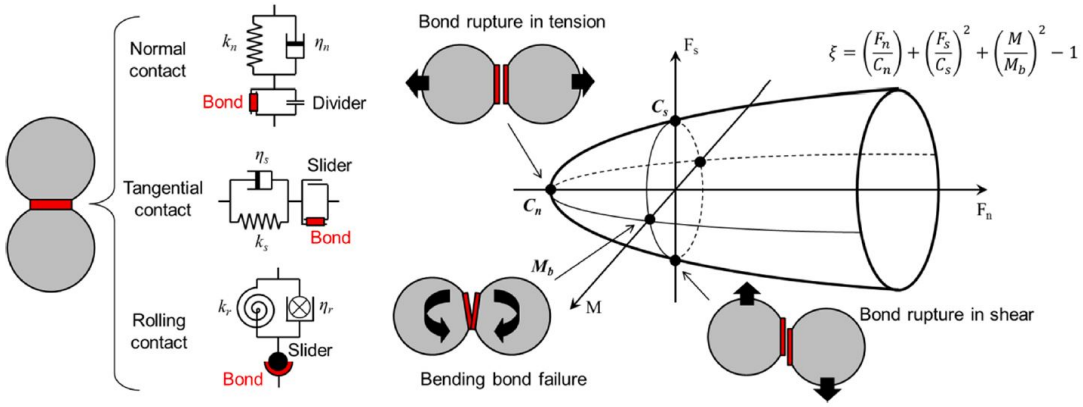

FIGURE 2.7 – Failure criterion of parabolic shape (BENSEGHIER et al. 2020)

2.3 Lattice Boltzmann Method (LBM)

As KRÜGER et al. 2017 describe, the Lattice Boltzmann Method (LBM) is a computational fluid dynamics technique (CFD) widely employed to simulate fluid flows and model complex fluid behaviors. While the equations of fluid mechanics pose challenges for general analytical solutions, numerical methods are better suited for solving cases involving complex boundary conditions. However, implementing and parallelizing numerical schemes for fluid simulations can be difficult and computationally demanding. Nevertheless, the LBM offers advantages in terms of implementation and parallelization compared to other fluid mechanics methods, such as finite element and finite volume. The numerical scheme for the solution of the Boltzmann equation can be easily implemented and parallelized, making it an appealing choice for fluid simulations. Additionally, the Boltzmann equation leads to the equation of fluid dynamics at the macro-scale; thus, by obtaining a solution to the Boltzmann

equation, one can determine a solution to the Navier-Stokes equation. Further details on this topic can be found in KRÜGER et al. 2017. The basic quantity of LBM are the discrete velocity distribution functions also known as PDFs (particle distribution functions). These functions $f_i(x,t)$ represent the density of fluid particles with the velocity $c_i = (c_i x, c_i y, c_i z)$ at the position x and time t. The mass density of the fluid which is simply the sum over all the PDFs can be expressed as:

$$\rho(x,t) = \sum_i f_i(x,t), \tag{2.23}$$

Also the first-order momentum of the fluid can be expressed as:

$$\rho u(x,t) = \sum_i c_i f_i(x,t), \tag{2.24}$$

In these equations, the particle distribution functions, denoted as $f_i(x,t)$, play a crucial role. The index i represents the i-th component of the vector containing the particle distribution functions. c_i represents the i-th discrete velocity. There are several specific lattice structures used in the Lattice Boltzmann Method (LBM) for simulating fluid flows. Among them, the most commonly used velocity sets for solving the Navier-Stokes equation are D1Q3, D2Q9, D3Q15, D3Q19, and D3Q27. According to RETTINGER 2013, the D2Q9 model is commonly employed in 2D simulations, while the D3Q19 model is frequently used in 3D simulations.

The lattice Boltzmann equation can be defined as follows:

$$f_i(x + c_i \Delta t, t + \Delta t) - f_i(x,t) = \Omega_i(x,t), \tag{2.25}$$

In this equation, Ω_i signifies the i-th component of the collision factor, which will be further explained. This equation means that the particle i with particle distribution function $f_i(x,t)$ moves with the velocity c_i to the neighboring cell at $x + c_i \Delta t$ (Figure 2.8). Also it can be seen that the particles are also affected by the collision operator Ω_i which resembles the collision between particles, which will be explained in the following subsection. After selecting the appropriate velocity set (D1Q3, D2Q9, D3Q15, D3Q19, or D3Q27), the simulation comprises two main stages: (i) the collision step and (ii) the streaming step. More information regarding different velocity sets can be found in the next subsection.

2.3.1 Collision step

During this step, the parameter Ω_i is evaluated and used to update the particles distribution functions (f_i), according to the equation:

$$f_i^*(\vec{x}_i, t) = f_i(\vec{x}_i, t) + \Omega_i(\vec{x}_i, t), \tag{2.26}$$

where f_i^* represents the post-collision operator, and $\vec{x}_i$ is the location of the i-th lattice cell. The most renowned collision models include BGK, TRT, and MRT, which

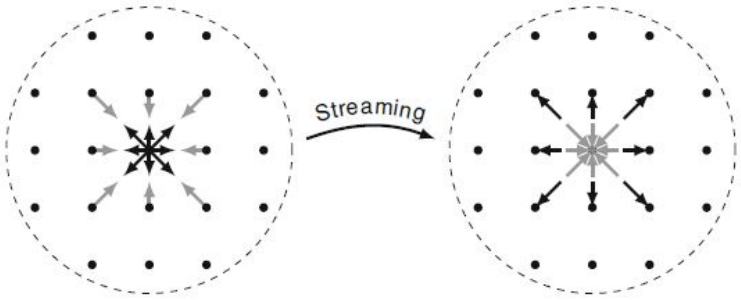

FIGURE 2.8 – The process of moving the particle distribution functions within the lattice from one lattice node to neighboring nodes (KRÜGER et al. 2017)

will be introduced in the following.

2.3.2 Streaming step

During this step the calculated post-collision operator f_i^* will be streamed to the neighboring cells with the velocity c_i:

$$f_i(\vec{x}_i + \vec{c}_i \Delta t, t + \Delta t) = f_i^*(\vec{x}_i, t), \tag{2.27}$$

According to RETTINGER 2013, the calculations for both steps can be performed locally for each lattice cell. They only need to exchange information with neighboring cells, not globally. This feature makes LBM highly optimal for parallel computing, allowing each lattice cell to be passed to different nodes to enhance the model's time efficiency.

2.3.3 Collision operators

2.3.3.1 Bhatnagar-Gross-Krook (BGK) model

The collision operator is utilized to simulate local fluid particle collisions within lattice cells. Various collision models, denoted as Ω, are available. Among these models, the Bhatnagar-Gross-Krook (BGK) operator represents the simplest approach:

$$\Omega_i(f) = -\frac{f_i - f_i^{eq}}{\tau} \Delta t, \tag{2.28}$$

This operator relaxes the population toward the equilibrium f_i^{eq} with the rate determined by the relaxation time, τ. The equilibrium distribution function can be determined as follows:

$$f_q^{eq}(x,t) = w_i \rho(x,t) \left[1 + \frac{u \cdot c_i}{c_s^2} + \frac{(u \cdot c_i)^2}{2c_s^4} - \frac{u \cdot u}{2c_s^2} \right], \tag{2.29}$$

where $c_s = c/\sqrt{3}$ is the speed of sound in the lattice system while $c = \Delta_x/\Delta_t$ is the lattice speed which depends on the specific lattice model chosen (D2Q9, D3Q19). The

relationship between relaxation time, τ and the kinematic viscosity ν can be expressed as:

$$\tau = \frac{\nu}{\Delta t c_s^2} + \frac{1}{2}, \tag{2.30}$$

The density ρ, and velocity u can be determined from Equation 2.23 and Equation 2.24, respectively. Also the fluid pressure can be calculated directly:

$$p = c_s^2 \rho, \tag{2.31}$$

According to RETTINGER 2013 another important aspect of the LBM method is the boundary condition such as bounce-back boundary for simulating steady and moving walls which will be explained briefly in upcoming subsections.

2.3.3.2 Two Relaxation Time (TRT)

According to KRÜGER et al. 2017 , the TRT model proposed by GINZBURG et al. 2008 is based on the decomposition of the lattice population into symmetric and asymmetric parts. In this model for the given velocity c_i there is an opposite velocity $c_{\bar{i}} = -c_i$. Using this notation the distribution functions f_i can be written as:

$$\begin{aligned} f_i^+ &= \frac{f_i + f_{\bar{i}}}{2}, \quad f_i^- = \frac{f_i - f_{\bar{i}}}{2}, \\ f_i^{eq+} &= \frac{f_i^{eq} + f_{\bar{i}}^{eq}}{2}, \quad f_i^{eq-} = \frac{f_i^{eq} - f_{\bar{i}}^{eq}}{2}, \end{aligned} \tag{2.32}$$

Thereby, the distribution functions are decomposed in their symmetric and antisymmetric parts:

$$\begin{aligned} f_i &= f_i^+ + f_i^-, & f_{\bar{i}} &= f_i^+ - f_i^-, \\ f_i^{eq} &= f_i^{eq+} + f_i^{eq-}, & f_{\bar{i}}^{eq} &= f_i^{eq+} - f_i^{eq-}, \end{aligned} \tag{2.33}$$

Similar to the BGK model, for the TRT model the post-collision operator, f_i^*, and distribution function, f_i, can be expressed as follows:

$$\begin{aligned} f_i^* &= f_i - \omega^+ \Delta_t (f_i^+ - f_i^{eq+}) - \omega^- \Delta_t (f_i^- - f_i^{eq-}), \\ f_i(x + c_i \Delta_t, t + \Delta_t) &= f_i^*(x, t), \end{aligned} \tag{2.34}$$

where $\omega^+ = 1/\tau$ and ω^- are constants which need to be tuned in order to find a stable condition of the given simulation (BENSEGHIER 2019). However it can be also determined from a so-called "magic parameter", $\Lambda = (1/\omega^+ - 1/2)(1/\omega^- - 1/2)$. According to GINZBURG et al. 2008 a value of $\Lambda = 1/4$ results in the most stable simulation. The TRT collision operator can be expressed as:

$$\Omega_i^{TRT} = -\omega^+ (f_i^+(x,t) - f_i^{eq+}(x,t)) - \omega^- (f_i^-(x,t) - f_i^{eq-}(x,t)) \tag{2.35}$$

2.3.3.3 Multi-Relaxation Time (MRT)

The Multi-Relaxation Time (MRT) method, as opposed to the conventional LBM methods which use one or two relaxation times to update probability distribution of particles, introduces separate relaxation times for each moment of the distribution function. In contrast to the other methods this method uses moment space instead of applying distribution functions directly. The link between the distribution functions $[f_0, f_1, ..., f_8]^T$ and their moment vector $\vec{m} = [\phi, e, \epsilon, j_x, q_x, j_y, q_y, P_{xx}, P_{xy}]^T$, and invertible transformation matrix M for D2Q9 can be found in Equation 2.36, where ϕ is fluid density, e is the energy, ϵ is related to energy square, $j_{x,y} = \rho u_{x,y}$ are x and y momentum components, P_{xx} and P_{xy} are diagonal and off-diagonal components of stress tensor, and q_x and q_y are x and y components of the energy flux. The relationship between moment vector, $\vec{m}$, and distribution functions (PDFs) can be expressed as:

$$\begin{aligned} \vec{m} &= M\vec{f}, \\ \vec{f} &= M^{-1}\vec{m}. \end{aligned} \tag{2.36}$$

This formula in the matrix format can be written as:

$$\mathbf{m} = \begin{bmatrix} \phi \\ e \\ \epsilon \\ j_x \\ q_x \\ j_y \\ q_y \\ P_{xx} \\ P_{xy} \end{bmatrix}, \quad \mathbf{M} = \begin{bmatrix} 1 & 1 & 1 & 1 & 1 & 1 & 1 & 1 & 1 \\ -4 & -1 & -1 & -1 & -1 & 2 & 2 & 2 & 2 \\ 4 & -2 & -2 & -2 & -2 & 1 & 1 & 1 & 1 \\ 0 & 1 & 0 & -1 & 0 & 1 & -1 & -1 & 1 \\ 0 & -2 & 0 & 2 & 0 & 1 & -1 & -1 & 1 \\ 0 & 0 & 1 & 0 & -1 & 1 & 1 & -1 & -1 \\ 0 & 0 & -2 & 0 & 2 & 1 & 1 & -1 & -1 \\ 0 & 1 & -1 & 1 & -1 & 0 & 0 & 0 & 0 \\ 0 & 0 & 0 & 0 & 0 & 1 & -1 & 1 & -1 \end{bmatrix}, \quad \mathbf{f} = \begin{bmatrix} f_0 \\ f_1 \\ f_2 \\ f_3 \\ f_4 \\ f_5 \\ f_6 \\ f_7 \\ f_8 \end{bmatrix}$$

According to RETTINGER 2013, for the MRT model the collision factor can be described with collision matrix, S, instead of single relaxation time like BGK:

$$\vec{\Omega}_i = -S(\vec{f}_i - \vec{f_i^{eq}}) \tag{2.37}$$

In the BGK model the S matrix can be expressed as $S = 1/\tau I$ where I is the identity matrix. With the help of Equation 2.36, and because $S = M^{-1}\hat{S}M$ the collision parameter can be re-written as:

$$\vec{\Omega}_i = -M^{-1}\hat{S}(\vec{m}_i - \vec{m_i^{eq}}) \tag{2.38}$$

Also, the Lattice Boltzmann equation with multi-relaxation time can be written as:

$$f(x + c_i\Delta t, t + \Delta t) - f(x,t) = -M^{-1}SM[f(x,t) - f^{eq}(x,t)]\Delta t \tag{2.39}$$

where for D2Q9 S can be written as $S = diag[s_1, s_2, s_3, ..., s_8]$. In this model $s_{1,2,4}$ are constants chosen from the range $[0,2]$, $s_{7,8} = 1/\tau$ where τ is the relaxation time from

the BGK model, and $s_{0,3,5}$ are set to zero. More information regarding the MRT model can be found in KRÜGER et al. 2017.

2.3.4 Velocity sets

In 2D cases for the D2Q9 model the nine velocity parameters c_i, as represented in Figure 2.9, are defined as:

$$c_i = \begin{cases} (0,0), & i = 0 \\ (1,0),(0,1),(-1,0),(0,-1), & i = 1,2,3,4 \\ (1,1),(-1,1),(-1,-1),(1,-1), & i = 5,6,7,8 \end{cases}$$

Furthermore, the weights in this model are: $w_0 = 4/9$ and the $w_i = 1/9$ for $||w_i|| = 1$ and $w_i = 1/36$ for $||c_i|| = \sqrt{2}$.

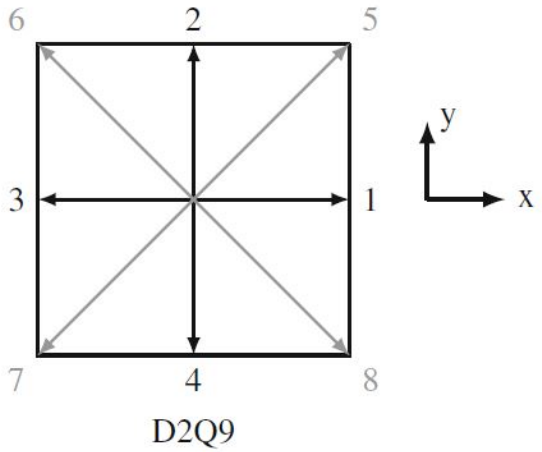

FIGURE 2.9 – D2Q9 velocity sets (KRÜGER et al. 2017)

The most popular 3D models are D3Q15, D3Q19, and D3Q27 (Figure 2.10). The velocity sets for these 3D models can be written as:
For D3Q15:

$$c_i = \begin{cases} (0,0,0), & i = 0 \\ (1,0,0),(-1,0,0),(0,1,0),(0,-1,0), & i = 1,2,3,4 \\ (0,0,1),(0,0,-1),(1,1,1),(-1,-1,-1), & i = 5,6,7,8 \\ (1,1,-1),(-1,-1,1),(1,-1,1),(-1,1,-1),(-1,1,1),(1,-1,-1) & i = 9,10,11,12,13,14 \end{cases}$$

For D3Q19:

$$c_i = \begin{cases} (0,0,0), & i = 0, \\ (1,0,0),(-1,0,0),(0,1,0),(0,-1,0),(0,0,1),(0,0,-1), & i = 1,2,3,4,5,6 \\ (1,1,0),(-1,-1,0),(1,0,1),(-1,0,-1),(0,1,1),(0,-1,-1), & i = 7,8,9,10,11,12 \\ (1,-1,0),(-1,1,0),(1,0,-1),(-1,0,1),(0,1,-1),(0,-1,1) & i = 13,14,15,16,17,18 \end{cases}$$

For D3Q27:

$$c_i = \begin{cases} (0,0,0), & i = 0, \\ (1,0,0),(-1,0,0),(0,1,0),(0,-1,0),(0,0,1),(0,0,-1), & i = 1,2,3,4,5,6 \\ (1,1,0),(-1,-1,0),(1,0,1),(-1,0,-1),(0,1,1),(0,-1,-1), & i = 7,8,9,10,11,12 \\ (1,-1,0),(-1,1,0),(1,0,-1),(-1,0,1),(0,1,-1),(0,-1,1), & i = 13,14,15,16,17,18 \\ (1,1,1),(-1,-1,-1),(1,1,-1),(-1,-1,1),(1,-1,1),(-1,1,-1), & i = 19,20,21,22,23,24 \\ (-1,1,1),(1,-1,-1) & i = 25,26 \end{cases}$$

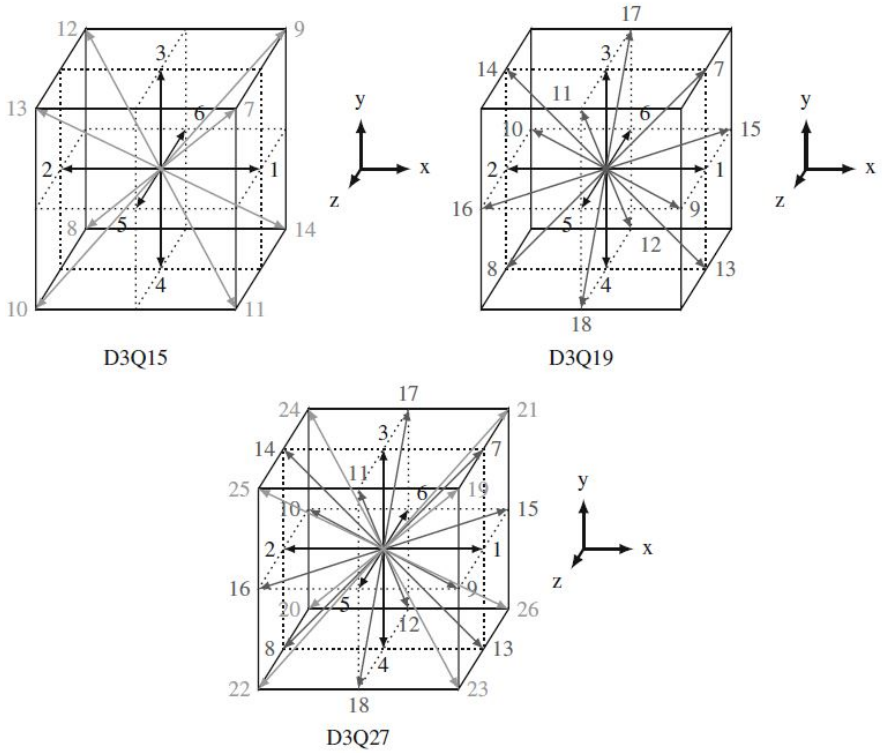

FIGURE 2.10 – D3Q15, D3Q19 and D3Q27 velocity sets (KRÜGER et al. 2017)

In the case of D3Q15, the weighting factors are as follows: when $|c_i| = 0$, the weight w_i is $\frac{2}{9}$; when $|c_i| = 1$, the weight w_i is $\frac{1}{9}$; and when $|c_i| = \sqrt{3}$, the weight w_i is $\frac{1}{72}$.

For D3Q19, the weight values are: when $|c_i| = 0$, the weight w_i is $\frac{1}{3}$; when $|c_i| = 1$, the weight w_i is $\frac{1}{18}$; and when $|c_i| = \sqrt{2}$, the weight w_i is $\frac{1}{36}$.

Lastly, for D3Q27, the weighting factors read: when $|c_i| = 0$, the weight w_i is $\frac{8}{27}$; when $|c_i| = 1$, the weight w_i is $\frac{2}{27}$; when $|c_i| = \sqrt{2}$, the weight w_i is $\frac{1}{54}$; and when $|c_i| = \sqrt{3}$, the weight w_i is $\frac{1}{216}$. The different weighting factors for 3D Lattice models can be also found in Table 2.1.

TABLE 2.1 – Weighting factors for different Lattice models

Lattice Models (D3Q)	**Magnitude** ($|c_i|$)	**Weight** (w_i)
15	0	2/9
	1	1/9
	$\sqrt{3}$	1/72
19	0	1/3
	1	1/18
	$\sqrt{2}$	1/36
27	0	8/27
	1	2/27
	$\sqrt{2}$	1/54
	$\sqrt{3}$	1/216

2.3.5 Boundary conditions

2.3.5.1 Bounce Back

According to MOHAMAD 2011, the bounce-back boundary condition is used for both stationary and moving walls. With this method, particles approaching the solid boundary are bounced back into the flow domain, as illustrated in Figure 2.11. This figure depicts the halfway bounce-back boundary condition, where the boundary wall is assumed to be situated between the solid nodes and the fluid nodes in the lattice grid. The distribution functions f_7, f_4, and f_8 are determined from the streaming process. When they hit the wall, they bounce back into the flow domain, resulting in $f_5 = f_7$, $f_2 = f_4$, and $f_6 = f_8$. This method ensures conservation of energy and momentum at the boundary. Detailed discussions on this boundary scheme can be found in KRÜGER et al. 2017 and MOHAMAD 2011.

2.3.5.2 Velocity boundary condition

The boundary condition with known velocity is commonly used in simulations that involve inlets with imposed velocities. In Figure 2.12, focusing on the west side, the streaming distribution functions $f_{2,3,4,6,7}$ are known and have been streamed to the boundary. The distribution functions $f_{1,5,8}$ now need to be calculated. For calculating the unknown distribution functions, the Equation 2.23 and 2.24 are used with the equilibrium condition at the boundary, for example : $f_1 - f_1^{eq} = f_3 - f_3^{eq}$. A more detailed and comprehensive explanation of the calculation of unknown distribution functions can be found in MOHAMAD 2011.

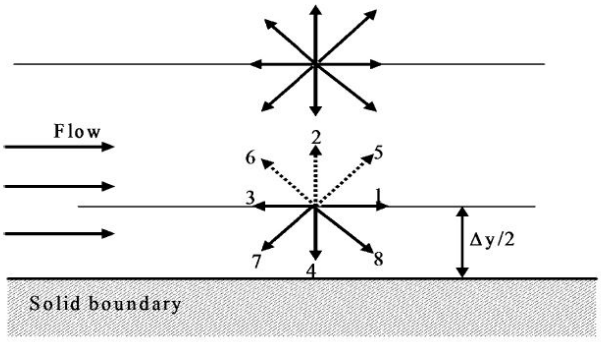

FIGURE 2.11 – Bounce back scheme (MOHAMAD 2011)

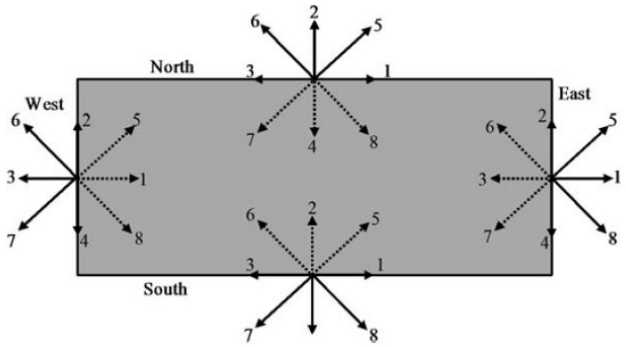

FIGURE 2.12 – Velocity boundary scheme (MOHAMAD 2011)

2.3.5.3 Periodic boundary condition

According to KRÜGER et al. 2017, the aim of the periodic boundary condition is to isolate the repeating flow pattern within a cyclic flow system. This condition is relevant only when the flow is periodic, implying that a flow exiting the domain on one side will re-enter from the opposite side. In Figure 2.13, distribution functions departing the domain from line b will re-enter from line a. This means that the unknown distribution functions at line b, represented by $f_{2,5,6,b}$, are equivalent to $f_{2,5,6,a}$, and the unknown distribution functions at line a, represented by $f_{4,7,8,a}$, are equivalent to $f_{4,7,8,b}$.

2.3.5.4 Pressure difference boundary condition

According to WEINSTEIN and FERNANDES 2020, in the LBM, the pressure is correlated to the fluid density as expressed by Equation 2.31. The imposed pressure difference in this method is established using varying densities, $\Delta\rho$, and the distribution functions f are defined in a manner similar to the velocity boundary condition. It is important to note that LBM simulations are sensitive to large values of $\Delta\rho$ in order to avoid shock propagation into the simulation domain.

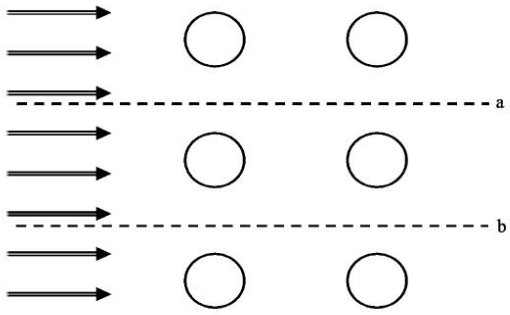

FIGURE 2.13 – Periodic boundary scheme (MOHAMAD 2011)

2.4 Coupling DEM and LBM

According to BENSEGHIER 2019, LBM is highly robust in terms of solid-interaction coupling. In the previous subsections, the interaction between fluid and stationary boundaries was introduced. When the simulation domain is considered as a grid, these boundaries are situated between solid and fluid nodes. It is also crucial to explore how LBM can manage moving boundaries, such as particles. In this context, two methods of solid-fluid coupling are presented: (i) the momentum exchange method and (ii) the partial saturation method (PSM). A shared principle between these methods is the mapping of solid particles onto the fluid domain (Lattice grid).

2.4.1 The momentum exchange method

According to BENSEGHIER et al. 2020, the microscopic fluid-solid interaction between LBM and DEM models can be introduced employing a suitable momentum-exchange algorithm by assuming a regularised non-slip bounce-back boundary condition at solid nodes proposed by BOUZIDI et al. 2001. This approach is modified for curved moving boundary conditions featuring a linear interpolation of post-collision fluid distribution functions using two fluid nodes x_f and x_{ff} (see Fig 2.14).

This scheme consideres two possible interpolation situations based on relative distance $q = |x_f - x_\omega|/|x_f - x_s|$ where x_f is the fluid node, x_s is the solid node, and x_ω is the solid intersection node:

$$f_{\bar{i}}(x_f, t+\Delta t) = \begin{cases} 2q f_i^*(x_f,t) + (1-2q) f_i^*(x_{ff},t) + 2\omega_i \rho_\omega \frac{c_{\bar{i}} u_\omega}{c_s^2}, & \text{for } q < 1/2 \\ \frac{1}{2q} f_i^*(x_f,t) + \frac{(2q-1)}{2q} f_i^*(x_{ff},t) + \frac{1}{q}\omega_i \rho_\omega \frac{c_{\bar{i}} u_\omega}{c_s^2}, & \text{for } q \geq 1/2 \end{cases} \tag{2.40}$$

where the velocity $c_{\bar{i}}$ is in opposite direction of c_i and u_ω is the wall velocity at the fluid-solid intersection point x_ω. This velocity can be obtained from the particle velocity U,

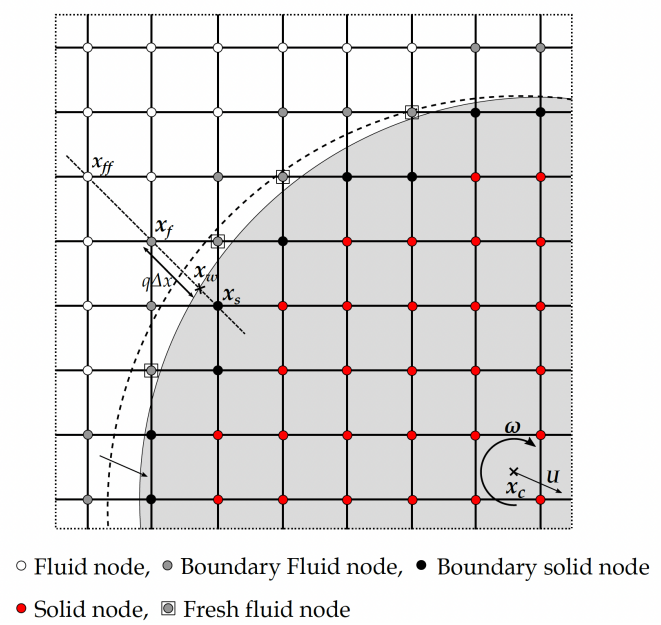

FIGURE 2.14 – Representation of a moving particle where the dashed line represents the previous position of the particle and fresh fluid nodes appear as represented by open squares (BENSEGHIER et al. 2020)

particle angular velocity ω and particle center of the mass x_c:

$$u_\omega = U + \omega \times (x_\omega - x_c) \tag{2.41}$$

One of the issues of this model is where the solid boundary converts to fluid nodes with unknown distribution functions. Based on the work of LALLEMAND and LUO 2003, it was proposed that these fresh fluid nodes can have approximate distribution function of $f_i^{eq}(\rho, u_\omega)$ computed using the average fluid density that fluctuates around 1, and the wall velocity at the specified node position just before it (BENSEGHIER et al. 2020). The total force acting on the particle by the fluid can be calculated using:

$$F = \sum_{x_f} \sum_i \left[f_i^*(x_f, t) + f_{\bar{i}}(x_f, t + \Delta t) \right] c_i, \tag{2.42}$$

Also the total torque acting on the particle from the fluid can be calculated using:

$$T = \sum_{x_f} \sum_i (x_\omega - x_c) \times \left[f_i^*(x_f, t) + f_{\bar{i}}(x_f, t + \Delta t) \right] c_i, \tag{2.43}$$

2.4.2 Partially saturated method (PSM)

Another approach for coupling DEM and LBM is called the Partially saturated method (PSM) proposed by NOBLE and TORCZYNSKI 1998. This method is based on the local solid fraction ε of each lattice cell. The cell can be fluid if $\varepsilon = 0$, solid if $\varepsilon = 1$ or partially

saturated if $0 < \varepsilon < 1$ (see Fig 2.15).

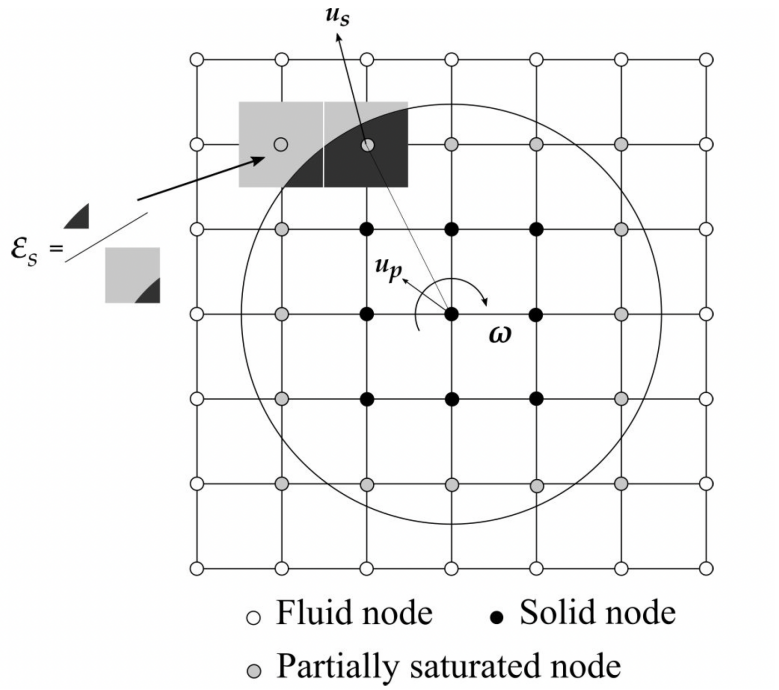

FIGURE 2.15 – Sketch of partial saturated method (BENSEGHIER et al. 2020)

The PSM is based on a modified BGK equation (see Equation 2.25) by introducing the solid fraction associated with a given lattice node and the presence of solid nodes:

$$f_i(x + c_i\Delta t, t + \Delta t) = f_i(x,t) + (1-B)\Omega_i^{BGK} + B\Omega_i^s, \tag{2.44}$$

where Ω_i^s is the collision operator for solid nodes calculated as:

$$\Omega_i^s = \left[f_{\bar{i}}(x,t) - f_{\bar{i}}^{eq}(\rho,u)\right] - \left[f_i(x,t) - f_i^{eq}(\rho,u_s)\right] \tag{2.45}$$

Therein u is the local fluid velocity, the velocity of the solid point x is given by $u_s = u_p + \omega \times (x - x_c)$, and B represents the weighting parameters:

$$B = \frac{\varepsilon_s(\tau - 1/2)}{(1-\varepsilon_s) + (\tau - 1/2)}, \tag{2.46}$$

where ε_s represents the solid fracture of a lattice node ($0 \le \varepsilon_s \le 1$). The force and torque acting on the boundary can be calculated using:

$$F = \frac{\Delta x^2}{\Delta t}\sum_{x_n} B(x_n)\sum_i \Omega_i^s(x_n)c_i, \tag{2.47}$$

$$T = \frac{\Delta x^2}{\Delta t}\sum_{x_n} B(x_n)(x_n - x_c)\times\sum_i \Omega_i^s(x_n)c_i, \tag{2.48}$$

where x_n is a lattice node which is partially or fully solid ($\varepsilon > 0$) and x_c is the center of the mass of the particle. Also, the modified PSM version based on the TRT collision model can be represented as :

$$f_i(x + c_i\Delta t, t + \Delta t) = f_i(x, t) + (1 - B)\Omega_i^{TRT} + B\Omega_i^s, \tag{2.49}$$

2.5 LBM nondimensionalization

According to BENSEGHIER 2019, the key element in working with LBM is using lattice units instead of other physical units. In LBM, both the space and time steps are equal to unity in lattice unit, i.e., $d_x = d_t = 1$. This implies that when working with SI units for simulation parameters, these parameters must be converted to LBM units before being used in an LBM simulation. A detailed explanation of the conversion from physical units to LBM units and vice versa can be found in KRÜGER et al. 2017. In lattice space, the space step is denoted as d_x, the time step as d_t, and ρ_0 represents the fluid density. According to KRÜGER et al. 2017, all physical units can be expressed as a factor of density q_{ρ_0}, space q_l, and time q_t. For instance, velocity has the SI unit of m/s, which means it has $q_l = 1$ and $q_t = -1$. A summary of several variables with their relevant factors is provided in Table 2.2.

TABLE 2.2 – Illustrating the conversion from physical to dimensionless units

Variables	q_{ρ_0}	q_l	q_t	**Factor**
Viscosity	1	0	0	ρ_0
Length	0	1	0	d_x
Time	0	0	1	d_t
Velocity	0	1	-1	d_x/d_t
Kinematic viscosity	0	2	-1	${d_x}^2/d_t$
Force density	1	1	-2	$\rho_0 d_x/{d_t}^2$
Force	1	4	-2	$\rho_0 {d_x}^4/{d_t}^2$
Torque	1	5	-2	$\rho_0 {d_x}^5/{d_t}^2$
Pressure	1	2	-2	$\rho_0 {d_x}^2/{d_t}^2$

Based on the table, to convert a variable from its physical unit to the lattice unit, it should be divided by the factor listed in Table 2.2. For instance, to convert a velocity of 20 m/s in SI units to the lattice unit, and assuming in SI unit $d_x = 2 \times 10^{-4}$ m, $d_t = 5 \times 10^{-5}$ s, and $\rho_0 = 1000\,\mathrm{kg/m^3}$ (which has no contribution in this example), the velocity in lattice units will be equal to $20/4 = 5$.

3 Numerical model implementation and optimization

Contents

3.1 Introduction

In the previous section, the DEM theory was described in detail. This method is highly parallelizable because each particle can be examined individually, and its state can be updated. DEM simulations can be computationally demanding, especially at larger scales and with more refined sized particles. To achieve a realistic simulation with thousands or millions of particles, high-performance computing or the power of GPUs and CPU clusters can be utilized.

In this study, to enhance the potential interaction calculations between granular materials, the fork-join model, OpenMP in CPU and CPU clusters, and CUDA programming to use the power of Graphical Processing Unit (GPU) have been employed, which will be explained in this chapter. Additionally, to detect particle interactions, theoretically each pair of particles within the domain must be considered as potentially overlapped. This approach results in a numerical model with O(N^2) time complexity, where performance is directly related to the square of the input elements' size (number of particles in domain) which in large scale simulations can be excessively time consuming.

This time complexity of the model can be improved by implementing the linked-cell algorithm within the model, which incorporates meshing into the simulation and groups particles with potential overlap into the same or neighboring cells. This grouping can be updated at different intervals. This approach will be explained in detail, including the algorithms used for implementation in this chapter. All of the code developments done within this PhD work are provided in a global repository in GitHub which can be accessed through SANAYEI 2023.

3.2 GPU parallelization

CUDA (Compute Unified Device Architecture) is a platform that grants users access to the GPU (Graphics Processing Unit) using the C/C++ programming language. Through this platform, users can use the substantial number of threads available on the graphics card, enabling the parallel execution of code on numerous threads.

According to CHENG et al. 2014, this architecture operates within a heterogeneous system environment, where both the CPU (Central Processing Unit), referred to as the host, and the GPU, referred to as the device, can work simultaneously and independently. The core concept in this architecture is known as the "kernel". A kernel is a function initialized from the host (CPU) with specified number of blocks and threads and each thread will take of part of the computation within the function. Users can map algorithms to the GPU using kernel functions, and after initializing the kernel, the CUDA platform manages the algorithm's execution on the GPU's threads. Once the kernel is launched, control returns to the host, which can operate independently.

It is important to know that the host and device possess separate memory spaces. Data transfer between the host and device is achievable through built-in memory mapping functions within this platform. In this architecture, the host is responsible for

executing serialized code, while the device (GPU) handles parallel code. When CPU intervention is necessary for data residing in GPU memory, data can be transferred from the device to the host using memory mapping. The CPU can then interact with the data and subsequently transfer it back to the GPU for the continuation of parallel algorithms.

The typical and straightforward process for executing a CUDA code is visualized in Figure 3.1 and described as follows:

- Copying data from the host to the device.
- Initializing the kernel and performing parallel operations.
- Copying the data back from the device to the host.

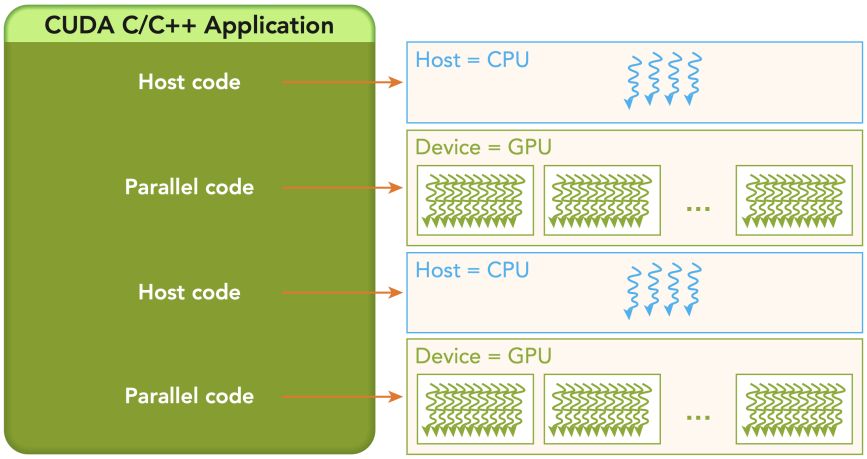

FIGURE 3.1 – Simple architecture of CUDA programming (CHENG et al. 2014)

Threads inside the GPU can be organized using a two-level hierarchy known as blocks and grids. Multiple threads can form a block of threads; however, threads from different blocks cannot cooperate with each other. Typically, a block of threads can accommodate a maximum of 1024 threads. Threads within a block can be indexed in up to three dimensions, denoted as threadIdx.x, threadIdx.y, and threadIdx.z.

If the code execution requires more than 1024 threads, multiple blocks can be initialized. The collection of created blocks is referred to as grids of blocks, and they can also be indexed in three dimensions as blockIdx.x, blockIdx.y, and blockIdx.z.

All threads within a grid have access to the GPU global memory. Furthermore, all threads within the same block have access to the shared memory of that specific block. It is important to note that different blocks do not have access to the shared memory of other blocks. For a visual representation of threads and blocks within a grid, it is referred to Figure 3.2.

In this study, the presented architecture is employed for the generation of particles within the domain, for both small and large scales. Initially, discrete element parameters, such as Young's modulus and friction coefficient, are initialized within the host.

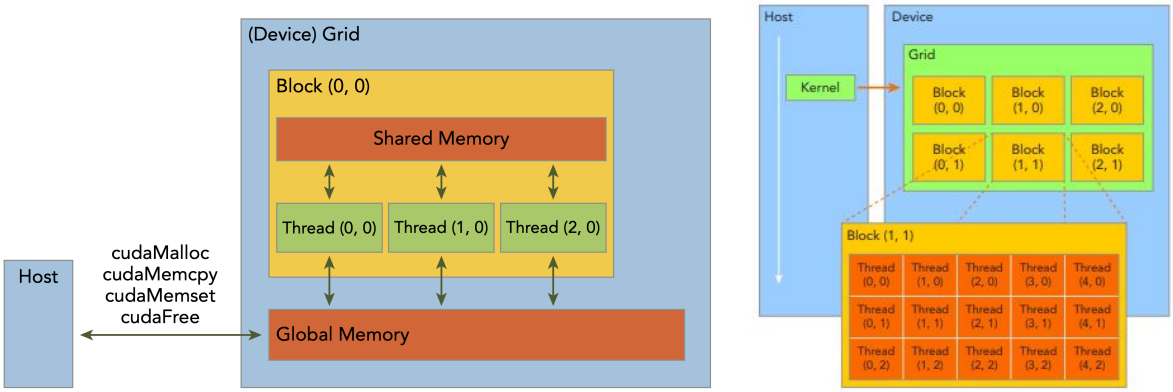

Single block Grid of blocks

FIGURE 3.2 – Illustration of threads and blocks residing inside a grid (CHENG et al. 2014)

Subsequently, these parameters are transferred to the device's global memory using a memory allocation function. Following this, the domain's boundaries, including interior walls, are initialized within the host and similarly mapped to the GPU's global memory.

Inside the host, the initial coordinates and properties of particles are generated for insertion into the domain. These particles are instantiated as instances of a class and are collectively stored within a vector. After this initial generation phase, these particles are copied to an array located in the device's global memory (GPU only can use arrays and have no internal vector). In this study, a configuration of 128 threads is assigned to each block of threads. This number was chosen based on trial and error for having better performance and time efficiency. Depending on the dimensions of the simulation domain and the initialized particles, the number of required blocks is calculated using the following formula in C/C++ syntax:

```
const int nThreadsPerBlocks  = 128;
const int nBlocks = (GRAINS + nThreadsPerBlocks -1)/nThreadsPerBlocks;
```

More information regarding choosing the number of threads in a block and detecting the number of blocks for a simulation can be found in CHENG et al. 2014 and STORTI and YURTOGLU 2015. Furthermore, as discussed in the introduction, the investigation of potential particle overlap is a crucial aspect of this study. To address this, a linked cell algorithm is implemented through meshing of the simulation domain and transferring these data from the host to the device. This algorithm groups particles into specific cells, a process executed at fixed intervals within the host and subsequently mapped to the GPU's global memory.

The interaction between particles and particles and the domain walls is examined within the device. In the device the properties of particles such as positions, velocities, and accelerations, are updated accordingly. During the specified time step, these

properties are synchronized back to the host and recorded for further examinations. Additionally, the new groupings and indexing established by the linked cell algorithm are updated based on the particles' modified positions and are subsequently mapped back to the device to continue the simulation. The code developed in this study using C++/CUDA for generating large-scale samples for the macro test, which will be investigated in the next chapter, is available at SANAYEI 2023.

3.3 Linked cell algorithm

As previously mentioned, one common method for examining particle interactions within the domain is to assess the potential interactions between each pair of particles during every simulation time step. This approach results in a time complexity of approximately $O[N(N-1)/2]$, which is approximately equivalent to $O[N^2]$, where N represents the number of particles present within the domain. While this method works well for simulations with a small number of particles, it can become quite time-consuming as the number of particles within the domain increases.

To address this issue and reduce the time complexity, as suggested by BECKER 2015, a cutoff radius can be introduced. This radius should be slightly larger than the radius of the largest particles found within the domain. As it can be seen from Figure 3.3 all particles located within this cutoff radius, r_{cutoff}, can then be considered as potential candidates for overlapping, and the rest of the particles inside the domain can be ignored.

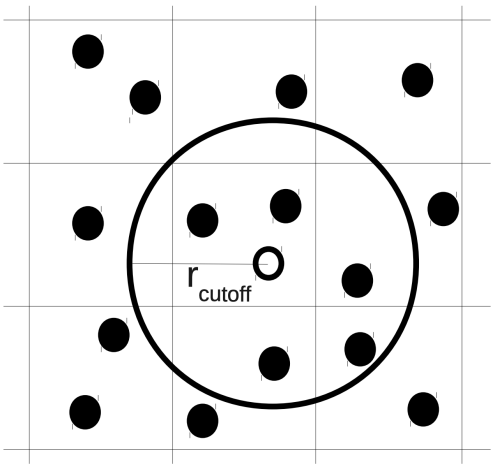

FIGURE 3.3 – Illustration of cutoff radius (ECKHARDT et al. 2013)

As shown in Figure 3.3, the domain is divided into multiple cells, each of which can be indexed as (cellx, celly, cellz). According to BECKER 2015, to implement the linked cell algorithm, two arrays need to be initialized: one named HEAD with a size of ncell (representing the number of cells within the domain), and another named LIST with a size of natom (or nparticle) equivalent to the number of particles within the domain.

The HEAD array serves to maintain references to the first particle identified within each specific cell. By utilizing the LIST index, it becomes possible to point to the remaining particles contained within that particular cell (see Figure 3.4).

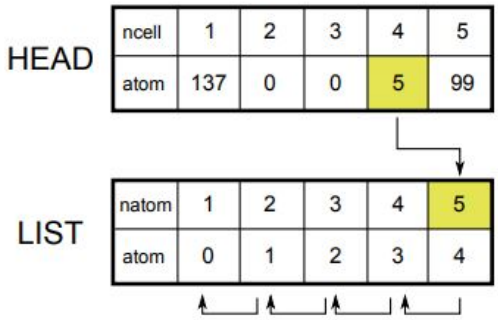

FIGURE 3.4 – Head and List array for detecting all particles residing inside a cell (BECKER 2015)

The sorting algorithm and creating HEAD and LIST arrays can be implemented in following three steps:

1. Creation of HEAD and LIST arrays
2. Assigning particles inside HEAD and LIST
3. Updating arrays in each x time steps (generally 50 time steps as suggested by literature).

These steps can be implemented using the algorithm 1:
In this algorithm $mesh\_resol$ should be chosen slightly larger than the largest particle found withing the domain, $mesh_x, mesh_y, mesh_z$ are the total number of cells considered in x, y, z directions which can be calculated using this code snippet in C/C++ syntax:

```
int mesh_x = floor((x_max - x_min)/mesh_resol) + 1;
int mesh_y = floor((y_max - y_min)/mesh_resol) + 1;
int mesh_z = floor((z_max - z_min)/mesh_resol) + 1;
```

The HEAD and LIST arrays, which have been generated, facilitate the examination of potential interactions between particles at each time step. This approach significantly reduces time complexity from quadratic (O[N^2]) to linear (O[N]). This efficiency is achieved because only particles within the same cell and its neighboring cells are considered for investigation, and they are easily accessible through the HEAD and LIST arrays.
These created arrays are instrumental in implementing the Verlet list (VERLET 1967) which is a list of neighbouring cells for each particle. The Verlet list algorithm restricts the investigation of potential interaction between particles within the same cell index

Algorithm 1 Sorting particles in HEAD and LIST arrays

Require:
$mesh\_resol$: Mesh resolution
$mesh\_x$: Number of cells in the x-direction
$mesh\_y$: Number of cells in the y-direction
$mesh\_z$: Number of cells in the z-direction
Particle data in vector g
x_min, x_max, y_min, y_max, z_min, z_max : Domain boundaries

for $i = 0$ to size$(g) - 1$ **do**
  Calculate cell indices :
  $ix = \lfloor (g[i].x - x\_min)/mesh\_resol \rfloor$
  $iy = \lfloor (g[i].y - y\_min)/mesh\_resol \rfloor$
  $iz = \lfloor (g[i].z - z\_min)/mesh\_resol \rfloor$
  Calculate cell index :
  $ncell = ix + (iy \cdot mesh\_x) + (mesh\_x \cdot mesh\_y \cdot iz)$
  Update linked list :
  $list[i] = head[ncell]$
  $head[ncell] = i$
end for=0

and its neighboring cells. The neighboring cells include those one unit to the left and one unit to the right along each dimension, resulting in a total of 9 cells in 2D and 27 cells in 3D space. The developed algorithm for the Verlet list function can be seen in algorithm 2. In this code, the process begins by calculating the cell index of the investigated particle (i). Subsequently, a triple *for* loop is utilized to explore the 27 neighboring cells. Within this nested loop, using the Head array, particle (j) residing in the same or a neighbouring cell will be detected and it will be passed to "$particles\_interaction$" function for further investigations. $particles\_interaction$ function calculates the overlap (δ) between these particles i, j and as explained before $\delta < 0$ means that the particles are interacting with each other.

In this study, the Linked Cell algorithm is employed to generate large-scale samples using the C++/CUDA code and for the macro traction simulation in C++. The developed algorithm is available in SANAYEI 2023, specifically within the *03-macro-traction-fork-join* folder. The initial algorithm for particle sorting is located in *dependencies/components/sortingParticles.h*, while the Verlet list is located in *dependencies/components/verletList.h*.

3.4 Fork-Join model for CPU parallelization

According to BECKER 2015, with the development of multi-core CPUs, the use of multi-threading and parallelization to enhance algorithm efficiency has become increasingly prevalent. In CPU parallelization, one can use both shared and distributed memory

Algorithm 2 Verlet list algorithm for particle interactions

Require:
Array $head$ containing cell head indices
Array $list$ to store linked list information
$mesh\_resol$: Mesh resolution
$mesh\_x$: Number of cells in the x-direction
$mesh\_y$: Number of cells in the y-direction
$mesh\_z$: Number of cells in the z-direction
Particle data in vector g
$x\_min, x\_max, y\_min, y\_max, z\_min, z\_max$: Domain boundaries

```
0: for i = 0 to size(g) − 1 do
0:   Calculate cell indices :
0:   ix = ⌊(g[i].x − x_min)/mesh_resol⌋
0:   iy = ⌊(g[i].y − y_min)/mesh_resol⌋
0:   iz = ⌊(g[i].z − z_min)/mesh_resol⌋
0:   for z = −1 to 1 do
0:     for y = −1 to 1 do
0:       for x = −1 to 1 do
0:         Calculate neighbor cell indices :
0:         ix_neighbour = ix + x
0:         iy_neighbour = iy + y
0:         iz_neighbour = iz + z
0:         Calculate neighbor cell index :
0:         ncell_neighbour = ix_neighbour + iy_neighbour · mesh_x + mesh_x ·
   mesh_y · iz_neighbour
0:         Initialize j with head[ncell_neighbour]
0:         while j > i do
0:           Calculate particle interactions :
0:           particles_interaction(i, j, dt)
0:           Update j with list[j]
0:         end while
0:       end for
0:     end for
0:   end for
0: end for=0
```

to run multiple threads simultaneously, thereby improving algorithm efficiency. In a distributed memory architecture, nodes can access their own memory quickly but have slower access to the memory of other threads (known as non-uniform memory access or NUMA). In contrast, when using shared memory among threads, all cores connect to memory banks at the same speed (referred to as uniform memory access or UMA).

To implement UMA in the developed algorithm, one can utilize the **OpenMP** li-

brary. This library removes the need for manual synchronization between threads, making it particularly suitable for loop parallelization. Within the algorithm, the most time-intensive task is identifying potential overlaps between particles using nested loops (Verlet list function). To boost model efficiency, a fork-join model can be employed to process multiple particles concurrently, and synchronizing the results at the conclusion. In Figure 3.5, it is evident that a section of the code operates in serial mode. However, when encountering the nested loops, the fork-join model, using multi-threading, distributes tasks across multiple threads, subsequently synchronizing the outcomes with the master thread.

In this study, the macro traction simulation, which will be explained in the next chapter, is developed in C++ and parallelized using the fork-join algorithm. It is further optimized with the Linked Cell algorithm. The source code is available in SANAYEI 2023, specifically within the *03-macro-traction-fork-join* folder.

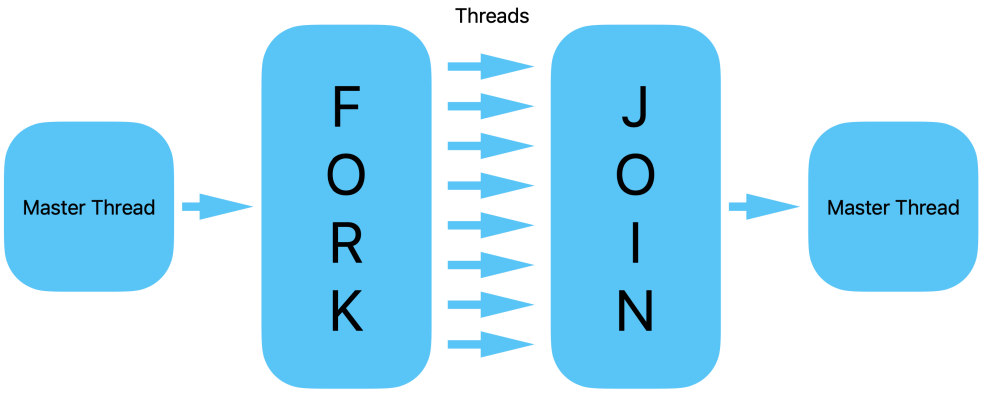

FIGURE 3.5 – Fork Join model illustration (BECKER 2015)

4 Model verification at micro and macro scales

Contents

4.1 3D bond model and comparing the results with Timoshenko Theory

4.1.1 Introduction

In this chapter, the ability of the microscopic bond model to correctly predict the benchmark situation of a cantilever beam made up of a few bonded particles is tested first, before turning to the sample scale via a macroscopic tensile test. In the study by CHEN et al. 2022, the main bond models in DEM are investigated and compared. While there are various bond models in DEM, these are primarily categorized into: (i) spring models, and (ii) beam models. In the spring model, the bond is represented by several parallel uniform springs located at the cross-section of the bond. This model calculates the forces and moments at the particle's contact point. Meanwhile, in the beam model, the bond is visualized as a beam connecting the two particles, and the forces and moments are calculated at the center of each particle (see Figure 4.1). As explained by CHEN et al. 2022, both models have their strengths and weaknesses. The performance of these models was investigated using different test cases. In particular three models were tested for their capability to predict the behaviour of a slender cantilever beam consisting of several particles: (i) parallel bond model (PBM), (ii) Euler-Bernoulli beam bond model (EBBM), and (iii) Timoshenko beam bond model (TBBM). The results were then compared with the theoretical solutions of the Timoshenko theory. Here, the reference test case from CHEN et al. 2022 will be simulated and evaluated using the bond model by DELENNE et al. 2004, see Section 2.2, and the results will be compared with the theory. The source code for this simulation can be found in SANAYEI 2023 in *01-beam-model-python* folder.

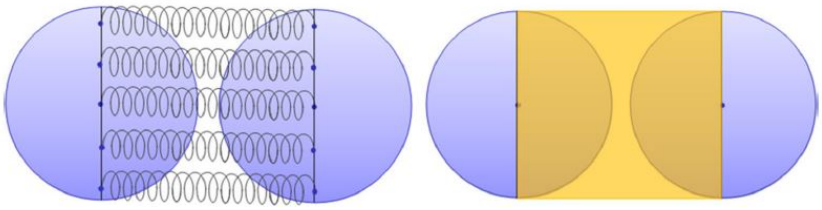

FIGURE 4.1 – Spring bond model (left), and beam bond model (right) (CHEN et al. 2022)

4.1.2 Test case description

In the study of CHEN et al. 2022 , the behavior of different bond models (PBM, TBBM, EBBM) is investigated by modeling a cantilever beam under a point load, as shown in Figure 4.2. In this test case, several particles are bonded together to form a beam. The leftmost particle is fixed, preventing both movement and rotation. A point load is gradually applied to the rightmost particle until an almost linear response from the system is obtained. It is worth noting that the remaining particles can move and rotate

freely. As the particles are bonded at both ends, they deform and deflect under the applied load. This study focuses solely on the reference case, where eleven particles, connected with zero overlap, undergo loading. Their deflection is then compared with the Timoshenko theory:

$$\delta_y = \frac{Fx^2}{6E_bI_b}(3L_0 - x) + \frac{10Fx}{9GA_b} \tag{4.1}$$

Therein F is the applied force, E_b is Young modulus, G is shear modulus, A_b is the cross section area of the beam, I_b is the second moment of area, and x is the beam coordinate in x direction. In the 3D model extended from DELENNE et al. 2004, the bond thresholds parameters must be set to extremely high values to prevent bond breakage. Furthermore, in the bond model from DELENNE et al. 2004 and the extended 3D model, particles with zero overlap are not considered bonded. To accommodate this study, modifications were made to the model, so that particles with overlap of zero are also considered as bonded particles. Note that the radius of the bonds is equal to the particles radius $r_b = R_p$ (Figure 4.3). It should also be mentioned that in this reference test case all eleven particles have the same geometry. The numerical results from CHEN et al. 2022 using PFC3D software and their comparison with the theory are illustrated in Figure 4.4, confirming a good agreement.

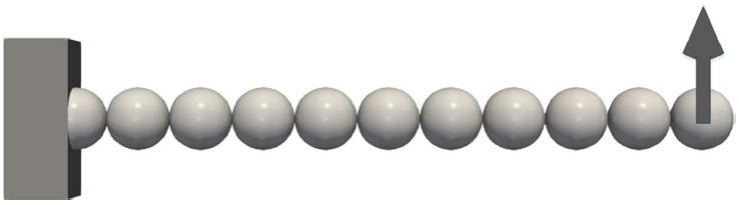

FIGURE 4.2 – Simulated cantilever beam using PFC3D (CHEN et al. 2022)

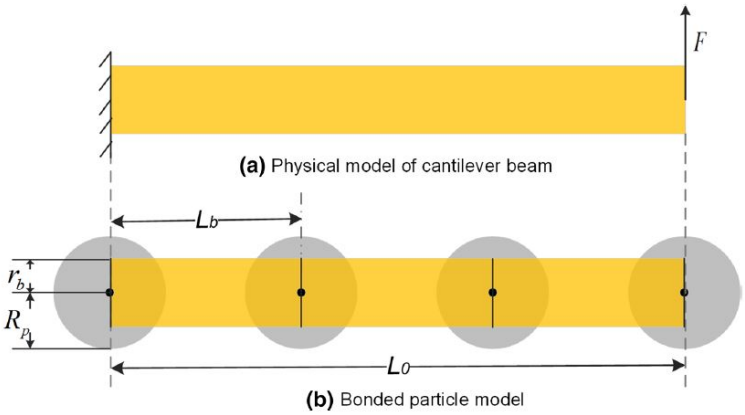

FIGURE 4.3 – (a) Physical model of cantilever beam and (b) bonded particle beam model (CHEN et al. 2022)

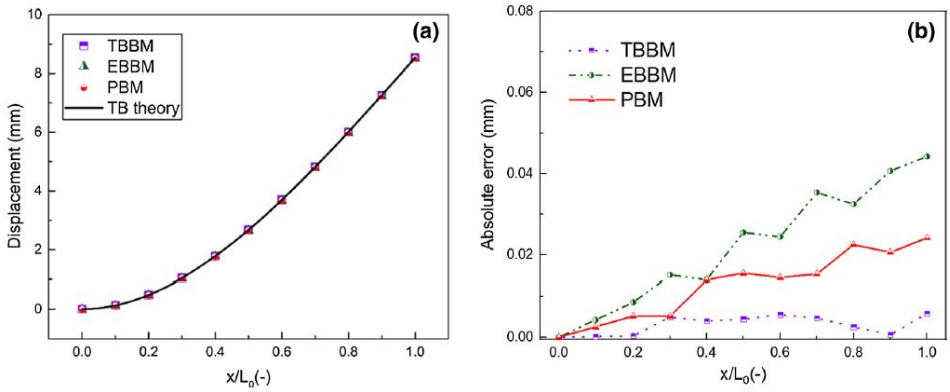

FIGURE 4.4 – Cantilever beam deflection using bond models and comparison with beam bond models where TBBM is Timoshenko beam bond model, EBBM is Euler–Bernoulli beam bond model, PBM is Parallel bond model, and TB theory is Timoshenko beam theory (CHEN et al. 2022)

4.1.3 Results and discussion

As explained in the previous subsection, to compare the cantilever beam test case with beam theory, eleven bonded particles adjacent to each other (using extended 3D model from DELENNE et al. 2004) were subjected to a vertical force apllied at the right end of the beam until an almost linear response from the system is obtained. To ensure the bonds were stiff, the Young's modulus was chosen as $E_b = 2 \times 10^8$ kN/m^2. The simulation ran for 1 second. The DEM properties and particle geometry are listed in Table 4.1.

TABLE 4.1 – Simulation parameters for cantilever beam

Parameter	**Value**
E_b	2×10^8 kN/m^2
K_s/K_n	1
ν_s/ν_n	0.2
μ	0.3
e_n	0.2
Gravity	[0, −9.81, 0] m/s^2
Particle radius (R)	0.2 m
Particle density (ρ)	2600 kg/m^3
Simulation time step (Δt)	1×10^{-5} s
Total time steps	100000

In this table, the parameter $\frac{K_s}{K_n}$ represents the ratio between tangential and normal stiffness. The value of K_n is determined using the formula $E_b \times \frac{A_b}{L_b}$ (CHEN et al. 2022), where A_b is the bond area, calculated with the formula πR^2, and L_b symbolizes the

distance between the centers of two bonded particles. The restitution coefficient, e_n is utilized for calculation of damping between particles using Equation 2.5.

After the linear response from the system is reached, the deflection of the particles was analysed. Figure 4.5 illustrates a comparison between the particle deflection obtained from the numerical simulation and the predictions from Timoshenko's theory. From these results, it is evident that the bond model from DELENNE et al. 2004, once adjusted to model 3D bonds, can reproduce the theoretical results from the models examined in CHEN et al. 2022. According to the theory, the beam maximum deflection should be 8.4890 mm, while the deflection recorded from the last particle was 8.4825 mm, corresponding to an error of 0.42%.

In subsequent steps, the extended bond model will be subjected to the more challenging case of macro traction tests.

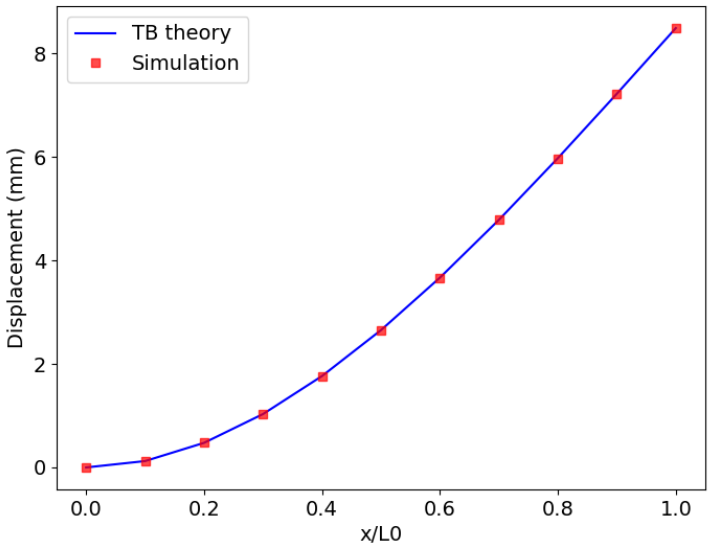

FIGURE 4.5 – Cantilever beam deflection using extended 3D model from DELENNE et al. 2004 and comparison with theory

4.2 Macro traction tests

4.2.1 Introduction

In this section, the existing experimental results and the process used for validating the developed bond model are presented. Next, detailed explanations of the numerical simulations created for these experiments are provided and the numerical and experimental results are compared.

As part of the bilateral COMET project (France-Germany), the present contribution thesis is complemented by a thesis with a strong experimental emphasis, hosted by the Aix Marseille University (RECOVER unit). A series of micro and macro tests were conducted by the PhD student Abbas Farhat using artificial soils made of silicate

glass beads with commercial paraffin as a binder. The procedures and results of the micro tests will be discussed in upcoming subsections. These micro test results will be used to calibrate the initial parameters of the numerical model. Next, the process and results for the macro cone tension tests conducted on three different sample sizes will be described. The numerical simulations developed for these test cases will be presented, and their outcomes will be compared with the experimental data. More information about these experiments can be found in FARHAT et al. 2021, FARHAT 2023, and BRUNIER-COULIN 2016. The first numerical model developed for these test setups and its results are available in SANAYEI et al. 2021.

4.2.2 Materials used in experiments

According to FARHAT 2023, artificial soils composed of glass beads were used in these experiments as a substitute for natural geo-materials (Figure 4.6). The use of glass beads provided better control over particle properties, including size, shape, roughness, and density.

The glass beads used in the experiments were spherical and were made of either silicate glass or borosilicate glass. The densities of these glasses were respectively $\rho = 2230\,\mathrm{kg/m^3}$ and $\rho = 2650\,\mathrm{kg/m^3}$. The silicate beads had diameters $d = 0.60 \pm 0.13\,\mathrm{mm}$, $d = 1.40 \pm 0.15\,\mathrm{mm}$, $d = 3.0 \pm 0.30\,\mathrm{mm}$, and $d = 4.0 \pm 0.30\,\mathrm{mm}$, whereas the borosilicate beads were $d = 5.0 \pm 0.20\,\mathrm{mm}$ and $d = 7.0 \pm 0.30\,\mathrm{mm}$ in diameter. The typical Young's modulus for these beads is estimated to be $E \approx 70\,\mathrm{GPa}$.

FIGURE 4.6 – Spherical glass beads with diameters 3 mm and 4 mm (FARHAT 2020)

Commercial paraffin, with a solid density of $880\,\mathrm{kg/m^3}$ and a Young's modulus of approximately 200 MPa, is used to bond the particles together as a liquid before hardening (Figure 4.7). It is important to mention that the volume reduction of paraffin after cooling is estimated to be less than 10 percent. The marked difference in the Young's modulus between the glass beads and the paraffin suggests that the deformation of the samples under tensile forces will predominantly arise from the deformation of the paraffin rather than the beads themselves.

FIGURE 4.7 – Commercial paraffin used as binder between particles (FARHAT 2023)

4.2.3 Macro tensile tests setup

The macro traction experiments were initially introduced in the work of BRUNIER-COULIN 2016, using a straightforward setup and basic devices. An updated version of these tests was later conducted by FARHAT 2023 in his work.

In Brunier-Coulin's research, as depicted in Figure 4.8, two overlapping conical shapes, meeting at their narrowest horizontal plane, were utilized. These cones were filled with a combination of beads and liquid paraffin. After the samples solidified, a tensile force was exerted on the upper conical shape via a cable and two pulleys while progressively filling a water container, as shown in Figure 4.8. The lower cone remained firmly anchored to the support, and it could not move. When the tensile force caused the two cones to separate, water pouring was halted, and the maximum force was calculated based on the water's weight in the container. Following this, the critical stress around the separation region was computed by dividing the obtained force by the rupture area (the area surrounding the sample's neck).

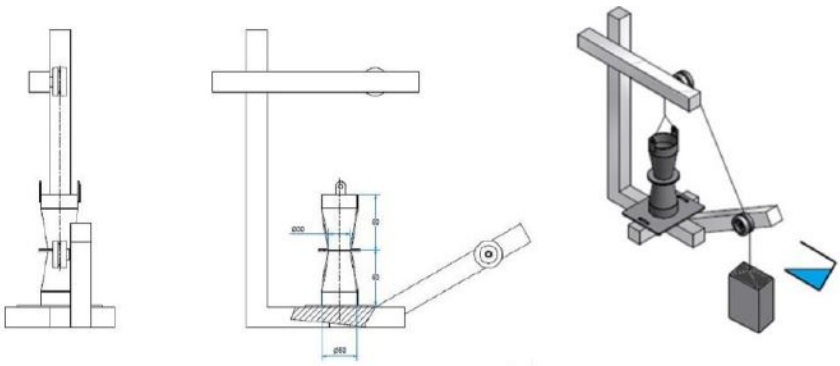

FIGURE 4.8 – Macro tensile test setup by BRUNIER-COULIN 2016

The mentioned device required prior calibration and delicate adjustments; however, its precision was limited. In the study conducted by FARHAT 2023, several modifications were implemented on this testing setup. As illustrated in Figure 4.9, a spring

with a stiffness of 9.52 N/mm is connected to the upper cone, with one end attached to a force sensor. The upper part of the spring can be elevated at a constant rate over time using a load press and computer software. The force applied to the upper cone is recorded by the sensor. The force applied to the sample, due to the elongation of the spring, increases linearly until a sudden drop in recorded force occurs due to the separation between the lower and upper cones. By utilizing the calculated force from the spring, the ultimate stress around the neck of the sample can be determined using the subsequent equation:

$$\sigma_t = \frac{F_t}{A} = \frac{F_t}{\frac{\pi}{4}D^2}, \tag{4.2}$$

Here, F_t represents the spring force recorded by the force sensor and reduced by the upper cone weight, and A denotes the area around the neck of the model with a diameter of D. In this test setup, the spring's elongation rate is maintained at a constant value between 0.1 mm/min and 0.3 mm/min.

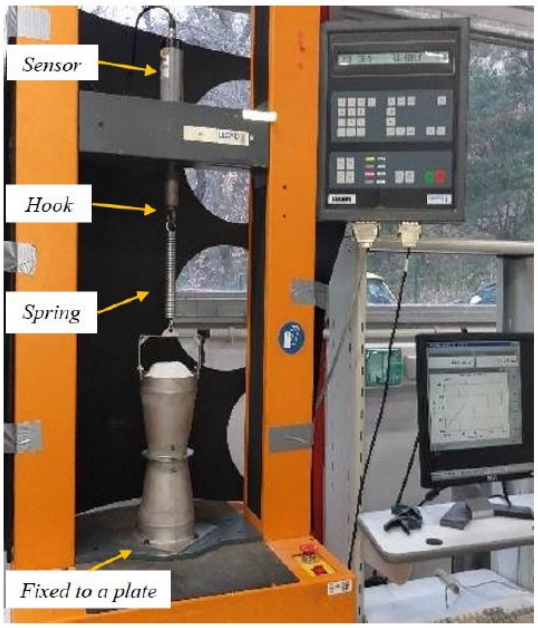

FIGURE 4.9 – Updated macro tensile test setup (FARHAT 2023)

Another enhancement introduced by FARHAT 2023 to the traction test setup was the ability to utilize cones of varying sizes. In his study, three distinct conical sizes—small, medium, and large—were employed. The properties of these cones are depicted in Figure 4.10.

4.2.4 Micro tests setup

In this study, the results from micro-tests conducted by FARHAT 2023 served for the calibration of initial values for the subsequently developed numerical model, which

FIGURE 4.10 – Three differently sized conical devices for tensile traction tests (FARHAT 2023)

will be explained in the following subsections. In Farhat's research, after executing macro traction tests, samples sourced from various sections of the cones were selected and subjected to micro traction, shear, moment, and torsion tests. Figure 4.11 shows the test setup designed for the micro traction test on a sample consisting of a pair of bonded particles. The bottom particle is anchored to a wooden surface, while the top particle is situated between bulldog tweezers. These tweezers are linked to a gentle spring with a stiffness of 0.027 N/mm for particles with diameters of 4 mm or smaller, and 0.31 N/mm for particles of larger dimensions. An inverted scale is further employed to measure the ultimate force exerted on the particles.

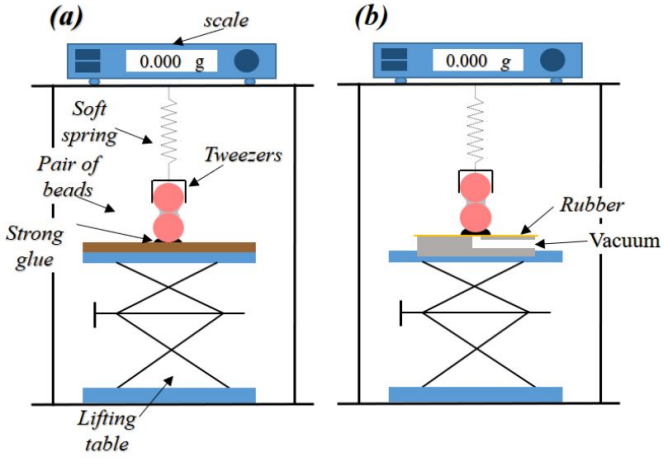

FIGURE 4.11 – Micro traction test setup (FARHAT 2020)

To start the test, the wooden bench below is steadily lowered at a uniform rate until the bond between the particles is separated. The inverted scale is connected to a computer, registering both the displacement and the force applied to the particles. A sharp drop in the recorded force (Figure 4.12) signifies the bond failure between the

two particles. It is worth noting that these micro tests proceed at a slow pace and are quite time-consuming.

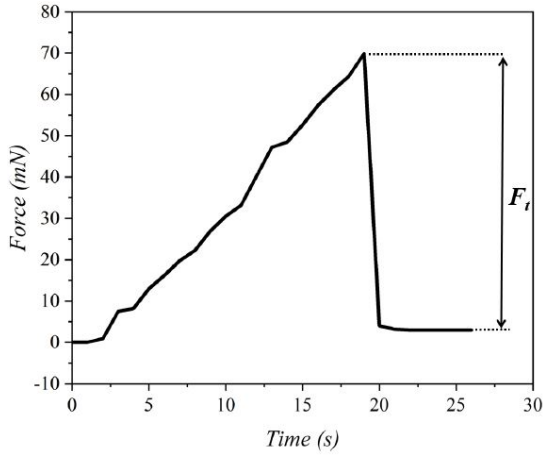

FIGURE 4.12 – Example for the time evolution of force in the micro traction tests (FARHAT 2020)

For different loading types such as shear, bending, and torsion, as illustrated in Figure 4.13, several modifications are made to the previously described setup. The shear setup has a strong resemblance to the traction setup but with a significant difference: the pair of particles is oriented perpendicular to the tweezers. One particle is anchored to the wooden surface, while the other is held between the tweezers, which are connected to both a soft spring and a scale. The surface is then raised until the bond between the particles breaks. To conduct bending and torsion tests, as shown in Figure 4.14, a wooden rod is firmly affixed to one of the particles. This rod is subsequently positioned between the tweezers.

4.2.5 Macro test results

As explained before, a series of traction tests were conducted on multiple samples of three different sizes: small, medium, and large. These tests involved samples of varying levels of paraffin content, namely 0.2%, 0.5%, 0.7%, and 1%. The ultimate traction force required for cones separation was measured using a force sensor, and the ultimate stress was subsequently calculated using Equation 4.2.

The comprehensive results of the macro tensile tests, including the ultimate traction force (recorded spring force minus the weight of the upper cone) and corresponding ultimate stress values for each paraffin content, are presented in Table 4.2.

As it can be seen from Table 4.2, a significant number of tests were conducted using 1% paraffin content, particularly with small and medium samples. Focusing on the results for small samples with 1% paraffin content, it can be observed from Figure 4.15 that the ultimate force varies between 22.2 N and 36.97 N. The mean value for the ultimate force in this configuration is determined to be 29.10 N, with a standard deviation of 6.62 N.

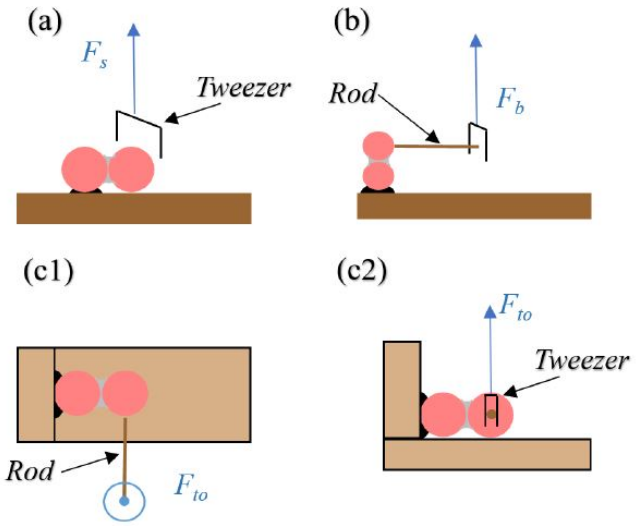

FIGURE 4.13 – The micro test setup for : (a) shear, (b) bending, and (c_1 & c_2) torsion (FARHAT 2023)

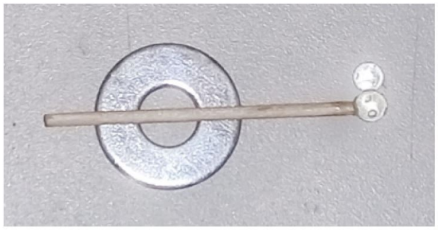

FIGURE 4.14 – Wooden rod glued to a pair of particles for performing micro bending and torsion tests (FARHAT 2023)

Furthermore, considering the results obtained for the medium cone with a paraffin content of 1%, it can be observed that the average force is 72.3 N, with a standard deviation of 25.1 N. These findings indicate a significant dispersion in the recorded ultimate force values. Moreover, referring to the table, it is worth noting that the ultimate force for the small cone with a paraffin content of 0.7% is 47.5 N. This value exceeds the maximum force recorded for small samples with a paraffin content of 1%, suggesting that it may be an outlier.

For each sample size and paraffin content the average ultimate force and average ultimate stress can be seen in Figure 4.16.

From these plots, it can be observed that in the case of the small samples with a paraffin content of 0.7% exhibit the highest ultimate force. In the case of the medium cone, the average force and stress values for both 0.7% and 1% paraffin content are quite similar. It should be mentioned that only a single sample went under the traction test for the 0.7 % content, while the ultimate results for the 1% samples displayed considerable dispersion.

TABLE 4.2 – Macro traction test results for different sample sizes and paraffin percentages

Cone Size	Paraffin %	Ultimate Force (N)	Ultimate Stress (kPa)
Small	0.2%	1.71	2.42
Small	0.2%	4.09	1.66
Small	0.5%	23.75	33.61
Small	0.5%	26.20	37.08
Small	0.7%	47.50	67.23
Small	1%	22.90	32.41
Small	1%	34.34	48.60
Small	1%	36.97	52.32
Small	1%	22.20	31.42
Medium	0.2%	8.24	3.34
Medium	0.5%	46.20	18.76
Medium	0.7%	73.96	30.04
Medium	1%	49.32	20.03
Medium	1%	50.29	20.42
Medium	1%	110.44	44.86
Medium	1%	79.10	32.13
Large	0.2%	69.43	14.17
Large	0.5%	190.68	38.92
Large	0.7%	256.78	52.41
Large	1%	253.79	51.80

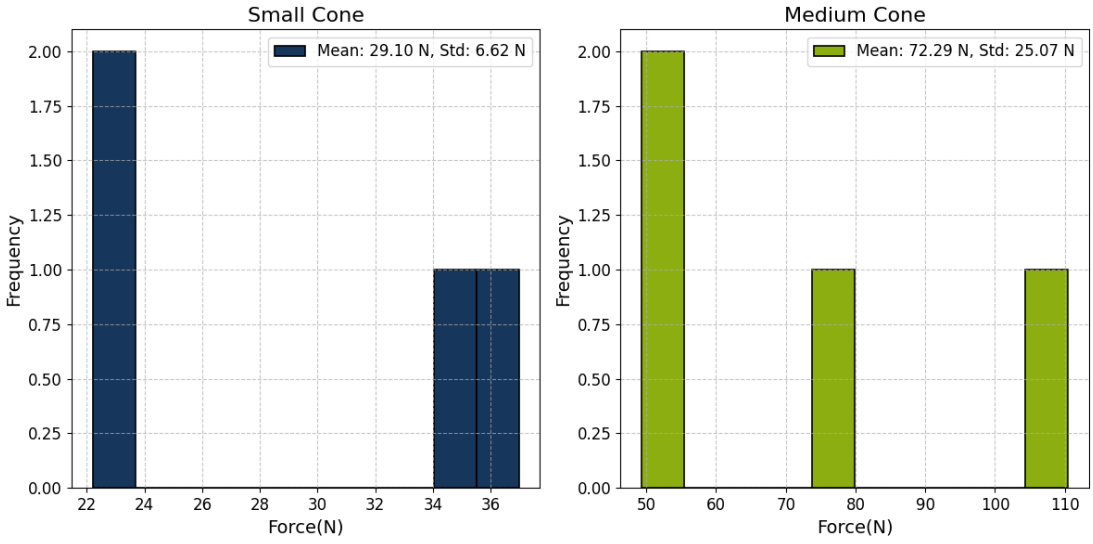

FIGURE 4.15 – Histogram for small and medium samples with 1% paraffin content

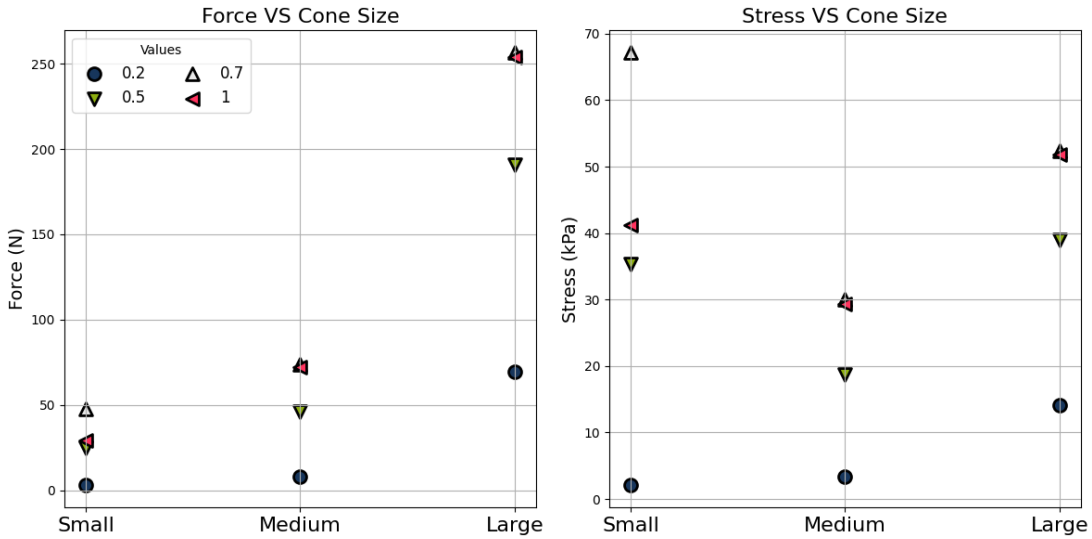

FIGURE 4.16 – The average ultimate force and average ultimate stress for each sample size with different paraffin content

Furthermore, it can be understood that the paraffin content alone does not solely determine the anticipated ultimate force. Other factors such as the compactness of the sample, the geometry and shape of sample settlement around the neck and coordination number, and other environmental factors could significantly influence the ultimate outcome.

In this study, numerical simulations were conducted on small, medium, and large samples with a paraffin content of 0.5% and 1%. These simulations considered both dense and loose samples, and the obtained results will be discussed in detail later.

4.2.6 Micro test results

The micro tests for traction, shear, moment (bending), and torsion were conducted using the experimental setups described in previous subsections. This study investigates the micro test results for two different paraffin content levels: 1% and 0.5%.

For the 1% paraffin content, a total of 20 traction micro tests were performed. As depicted in Figure 4.17, the results exhibit an average ultimate traction froce of 0.41 N and a standard deviation of 0.21 N, indicating a dispersed distribution. The maximum recorded result was 0.89 N, while the minimum was 0.20 N.

Similarly, for shear tests with 1% paraffin content, 10 different tests were carried out. The results exhibit an average shear force of 0.26 N with a standard deviation of 0.10 N, a maximum value of 0.41 N and a minimum value of 0.14 N.

Furthermore, 10 tests were performed for moment (bending), while 13 tests were performed for torsion. The average results for bending and torsion moments are 0.000640 Nm and 0.000517 Nm with the standard deviation of 0.000529 Nm and 0.000242 Nm, respectively. The minimum and maximum values for bending moment

were 0.00006 Nm and 0.00202 Nm, respectively. For torsion, the minimum value recorded was 0.00017 Nm, and the maximum value was 0.0008 Nm.

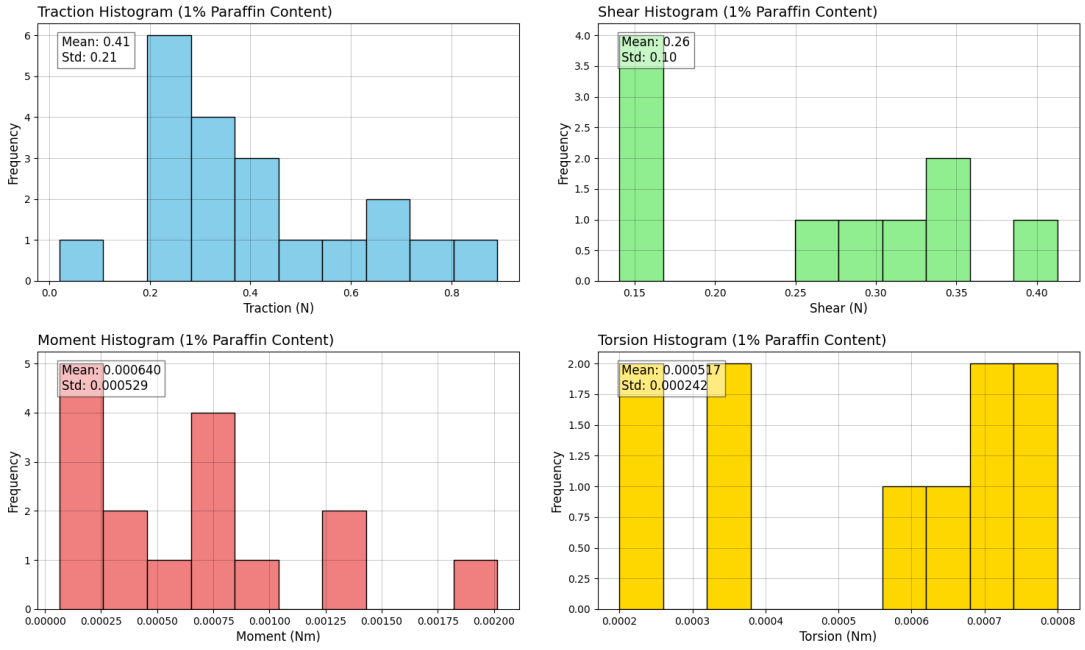

FIGURE 4.17 – Micro test results distributions for 1% paraffin content

In the numerical simulation, for 1% paraffin content the average traction result of 0.41 N is selected as the bond threshold value between particles, denoted as C_n. According to DENG and CARTER 2000 and after subsequent generalization to any particle size by BENSEGHIER et al. 2020 the thresholds for moment and shear can be determined as follows:

$$C_n = \beta \times C_s = \frac{C_m}{\alpha \times d_{\text{mean}}}, \tag{4.3}$$

where α is typically assumed to be 0.25 and β to be 2.0 in the literature. However, based on the average shear results obtained from the available experiments, a shear threshold value of $1/\beta = C_s/C_n = 0.26/0.41 = 0.63$ is chosen instead of the commonly used value of 0.5. Moreover, by considering the average bending and torsion results and employing Equation 4.3, the constant value for bending moment, denoted as α, is revised to 0.39 instead of the standard value of 0.25. Similarly, for torsion, the constant value α is adjusted to 0.31.

These modifications in the selection of threshold values account for the specific characteristics observed in the experimental shear, bending and torsion tests, providing a more accurate representation of the material behavior in the simulations.
Similarly, utilizing the identical experimental setup (see Figure 4.18), twenty micro traction tests were conducted for the 0.5% paraffin content, yielding an average result of 0.16 N. Additionally, ten tests were carried out for shear, with an average value of

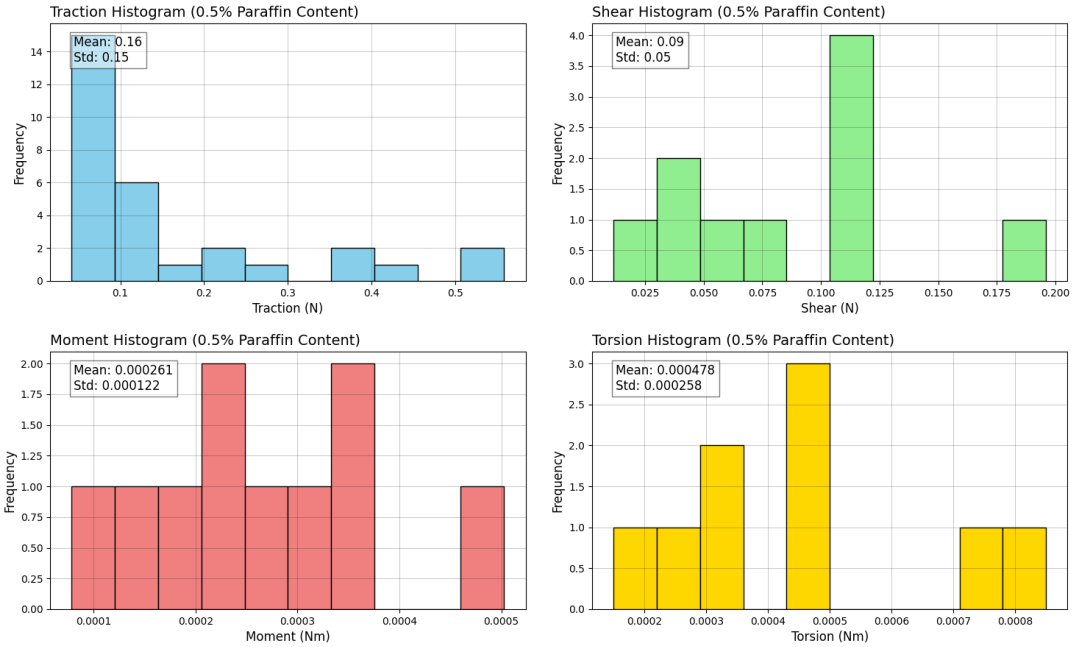

FIGURE 4.18 – Micro test results distributions for 0.5% paraffin content

0.09 N, resulting in a shear threshold ratio of $1/\beta = C_s/C_n = 0.09/0.16 = 0.56$, deviating from the standard value of 0.5.

Moreover, the average values obtained from the moment and torsion tests were 0.000261 Nm and 0.000478 Nm, respectively. Consequently, the corresponding threshold ratios are $\beta = 0.41$ for moment and $\beta = 0.74$ for torsion.

The dispersion of the micro test results for the 0.5 % paraffin content is visually represented in Figure 4.18, highlighting the variability observed in the experimental outcomes.

4.2.7 Numerical model for macro traction test

In this study, numerical simulations on three samples with different sizes and paraffin content of 1% and an average particle diameter of 4 mm (4 ± 0.3 mm) are conducted (Figure 4.19). The samples are created inside two conical shapes that overlap at their smaller radii. The properties of the conical shapes used as the boundaries can be found in Table 4.3. The interaction between particles and conical shaped can be detriment based on their potential overlap. The overlap between a sphere shape and a conical shape can be determined based on the work of FAN and WANG 2020 using the closest distance between a point (center of a sphere) and the cone surface. Initially, dense samples were generated using the CUDA code, with a low friction coefficient of 0.02. This choice of a low friction coefficient facilitated the creation of more compact samples. The first set of simulations focused on small-sized samples with over 3000 particles and paraffin content of 1%, utilizing the micro simulation results from Section

4.2.6 as the initial parameters for cohesive thresholds. Subsequently, different samples were created with a low friction coefficient to investigate the potential influence of different particle geometry around the neck of the sample on the ultimate force. In Table 4.4 the DEM parameters used in sample generation and traction test numerical simulation are listed.

TABLE 4.3 – Sample boundary properties

Sample Size	Small radius (r) (cm)	big radius (R) (cm)	height (h) (cm)
Small	3	5	8.1
Medium	5.6	8.5	10.8
Large	7.9	12	15

TABLE 4.4 – Macro traction simulation parameters

Parameter	**Value**
diameter	4.0 ± 0.3 mm
E	10^6 kgm/s^2
Verlet update in	10 timestep
$C_{n-1\%}$	0.41 N
$C_{n-0.5\%}$	0.16 N
C_s/C_n	0.5
Δt	10^{-5}
g	9.81 m/s^2
e	0.2
μ_s	0.05
μ_r	0.01
K_s/K_n	0.5
ν_s/ν_n	0.2
$K_r/K_n = K_o/K_n$	0.1
ρ_s	2650 kg/m^3

The stiffness of the particles during interaction was calculated based on ŠMILAUER and CHAREYRE 2010. According to this documentation, the stiffness K_n can be calculated as follows:

$$K_n = 2 \times E \times R_{\text{eff}} \tag{4.4}$$

where effective radius is defined as $R_{\text{eff}} = \frac{R_i R_j}{R_i + R_j}$ and E is the Young's modulus. Furthermore, additional simulations were conducted by introducing higher friction coefficients, resulting in looser samples. This was undertaken to examine the impact of sample compactness on the ultimate traction force.

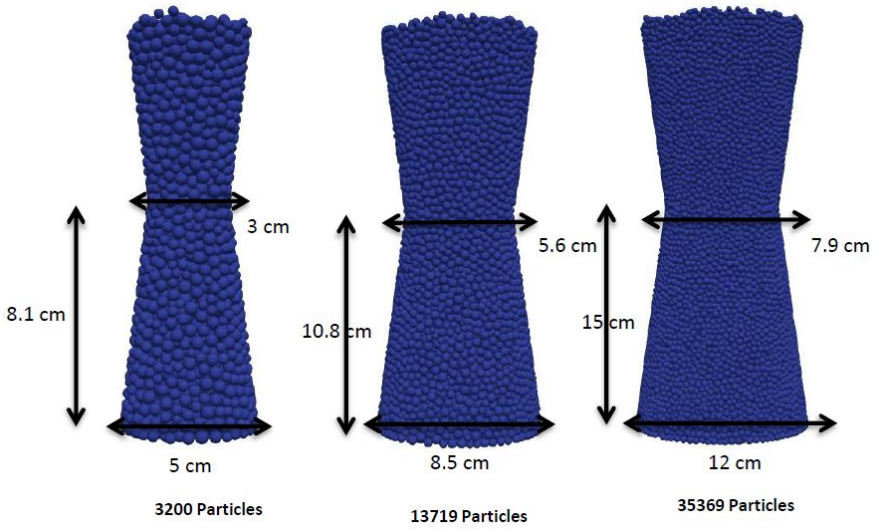

FIGURE 4.19 – Different sized samples for particles with diameter average of 4 mm (4 ± 0.3 mm)

After generating the samples, using the fork-join C++ code, the traction simulations are performed. Initially, during the first time step, particles that have overlap ($\delta < 0$) with each other are identified as bonded particles. Figure 4.20 displays the generated samples and detected bonds within the small-sized sample. Each bond in this figure is represented by a tube connecting the centers of two overlapping particles.

After sample generation, the traction simulation involves moving the upper conical shape upward (see Figure 4.20). The displacement of the upper cone in each simulation time step is determined by calculating the incremental force applied from a spring. Subsequently, the velocity, acceleration, and displacement of the wall are calculated based on this force from the spring in each time step. The displacement of the spring connected to the upper cone is progressively increased in each time step until the bonds surrounding the neck of the samples undergo traction. In model implementation, an incremental displacement, denoted as β, is consistently applied to the spring connected to the upper cone with each time step. Subsequently, the spring force exerted on the upper cone, as well as upper cone's acceleration and velocity, are updated during each of these steps. The spring displacement can be expressed as:

$$\delta_{sp}(t) = \delta_{sp}(t-1) + \beta \times \Delta t \tag{4.5}$$

where Δt is the time step which in this study is set to 10^{-5} seconds. The constant pulling rate α is determined as 1 mm/s, which is significantly higher than the actual pulling rate observed in the experiments, which is 0.3 mm/min. This increased pulling rate in the numerical simulation is implemented to reduce computational costs, particularly for medium and large samples, and the effect of slower pulling rate is not investigated because of the higher computational costs. Then the spring force is given

by:

$$F_t(t) = K \times \delta_{sp}(t) \tag{4.6}$$

where F_t represents the calculated spring force at time step t, and K denotes the stiffness of the spring. In this study, the spring stiffness is set as the actual value used in the experiments, which is 9.52 N/mm. Then the acceleration of the upper cone samples imposed by the spring at time step t is computed as follows:

$$a_t = \frac{F_t - F_i - M \times g - (\nu \times v_{t-1})}{M} \tag{4.7}$$

In this relation, M denotes the mass of the upper cone, g represents the acceleration due to gravity (9.81 m/s^2), ν is the damping coefficient, and v_{t-1} denotes the velocity of the upper cone at time step $t-1$. Using the calculated acceleration, the current velocity of the upper cone is determined by:

$$v_t = 0.5 \times \Delta t \times a_t + v_{t-1} \tag{4.8}$$

This formulation set regarding moving the upper cone upward and imposing spring force to the upper cone is chosen based on a methodology presented in RADJAI and DUBOIS 2011 and personal discussion with my adviser, Dr. Pablo Cuéllar.

The increase in spring displacement will persist until the bonds surrounding the neck of the samples go under traction force, leading to their failure and a sudden drop in bonds incremental force. As depicted in Figure 4.21, there are bonds surrounding the neck that have reached an internal force of 0.40 N at failure, which is the traction threshold determined for the numerical simulation based on the micro experimental results for 4 mm particles with 1% paraffin content. It should be mentioned that not all of the bonds around the neck reach the traction force threshold because the extended 3D model from DELENNE et al. 2004 considers the combined effects of traction, shear, bending and torsion as well. The color red in the image denotes a higher magnitude of the traction force around the neck compared to the other remaining bonds.

4.2.7.1 Small-sized samples with average diameter of 4 mm (4 $\pm$ 0.3 mm)

Three distinct samples with extremely low friction coefficients were created. As explained before the low friction coefficient leads to more compact and dense samples. Since the particles were randomly generated within a specified diameter range, 4.0 ± 0.3 mm, the only differing factors among the generated samples were the arrangement and spacing of particles around the neck of the model (overlapping region of two conical shapes) and the bond coordination number in that area. The coordination number for each particle is defined as the count of bonds to which it belongs. These three samples went under traction simulation with a spring increment of 1 mm/s. Throughout the traction test, the void ratio of the sample, the average coordination number of the entire sample, as well as that of individual sections (lower, neck, and upper), were recorded. Following the separation of the conical shapes, the ultimate force recorded from the spring (F_{spring}) was reduced by the weight of the upper sample (M) in order

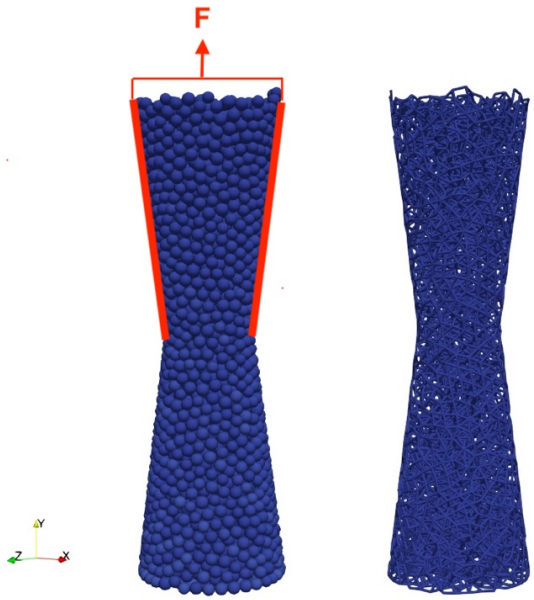

FIGURE 4.20 – (left) Settled particles generated from the CUDA code, (right) cohesive bonds represented as tubes

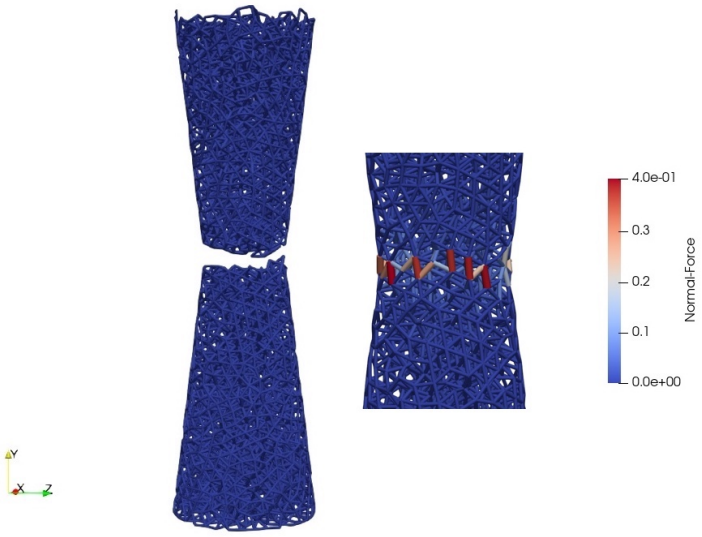

FIGURE 4.21 – (left) Separation of the upper and lower cone, (right) bonds around the neck reach 0.41 N which is the traction threshold based on micro traction tests

to calculate the ultimate force $F_{ultimate}$. To calculate the ultimate stress ($\sigma_{critical}$), the calculated ultimate force was divided by the area of the neck of the sample. In Figure 4.22, the development of the force from the spring and accumulated internal

force from the bonds until the separation of the lower cone from the upper cone is illustrated. As it can be seen from this plot, the ultimate spring force is recorded

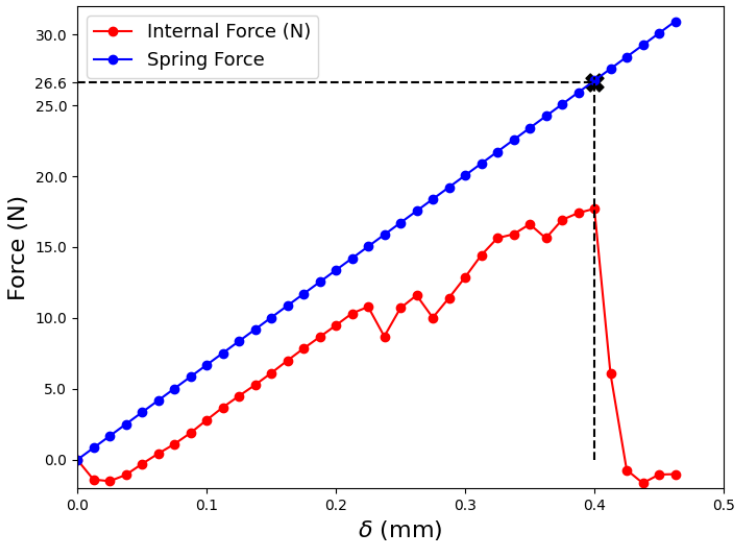

FIGURE 4.22 – Development of the tensile force from the spring and internal force from the bonds during the macro traction test (test No. 1).

as 26.6 N and the accumulated displacement of the sample is 0.4 mm. In this plot the difference between applied spring force and the internal forces is because the spring also must bear the weight of the upper cone plus the upper part of the sample. Furthermore, the presence of minor oscillations within the internal forces is evident. This phenomenon can be attributed to the negative acceleration of the upper cone in the simulated scenario, as indicated by Equation 4.7. Additionally, Equation 4.8 highlights the possibility of negative velocity for the upper cone. This negative velocity results in a downward movement of the upper cone, leading to a reduction in internal forces. Table 4.5 presents the recorded ultimate force and critical stress of the dense samples, while Table 4.6 indicates the coordination number evaluated in the different parts of the samples.

Subsequently, in order to compare the results from the dense samples with more loose samples, two additional samples with higher friction coefficients ($\mu = 1$) were generated and subjected to traction simulation. All simulation properties remained the same except for the friction coefficient. It should be mentioned that, in the traction simulation, the friction coefficient is also set to $\mu = 1$. However, increasing the friction coefficient only slightly changed the ultimate void ratio of the generated samples (see Table 4.5). The ultimate force and stress for these two tests can be observed in Table 4.5, while the bond coordination number evaluated in the different parts of the sample is recorded in Table 4.6. Based on these results, it can be concluded that the average coordination number around the neck influences the ultimate force and

critical stress of the samples. Dense samples exhibit a higher coordination number around the neck, and for tests with a coordination number exceeding 6, the spring force exceeds 26 N. This is attributed to the fact that during the traction test, the bonds around the neck primarily resist the external traction force from the spring, and a higher coordination number indicates a greater number of bonded particles around the neck region, resulting in a higher separation force. However, this effect of density and coordination numbers remains somewhat limited here, with less than 10% reduction for the two slightly looser samples. This is probably because the difference in void ratio is also relatively small, despite the change in friction during preparation. The five generated samples exhibited an average ultimate spring force of 25 N, which was slightly lower than the average experimental result of 29.1 N. As mentioned in the experimental section, the macro traction tests demonstrated high dispersity. In the experiments, for the small sample with 1% paraffin content, four samples were tested. The minimum recorded ultimate force was 22.2 N, while the maximum recorded force was 37 N, with a standard deviation of 6.6 N. Based on these results, and considering the high dispersity observed in the micro tests, slight adjustments to the cohesion variables such as thresholds for normal, shear, rolling, and torsion can help align the numerical results with the experimental ones.

Figure 4.23 depicts the comparison between the numerical simulation results and the corresponding experimental results listed in Table 4.2. The plot illustrates that the experimental results exhibit a greater degree of dispersity in comparison to the numerical results. The average of the experimental results is 29.1 N, while the average numerical result is 22.14 N. For the experimental results, the maximum value is 36.97 N, the upper quartile is nearly 35 N, the median is approximately 29 N, the lower quartile is around 23 N, and the minimum value is 22.2 N. For the numerical results, the maximum recorded force is 23.8 N, the upper quartile is around 23 N, the median is 22 N, the lower quartile is around 21.5 N, and the minimum recorded force is 21.1 N. Despite the disparity in the experimental results and the difference between the average values of the numerical and experimental data, there is a reasonably good overall agreement between the two sets of results.
Through a process of trial and error with variation of several numerical parameters, it was observed that the normal threshold, C_n, of the bonds has a significant influence on the ultimate force outcomes. Subsequently, the tangential threshold, C_t, was identified as the second most influential, followed by the ratio K_s/K_n. By adjusting these parameters, one can potentially align simulation results more closely with experimental findings.

Furthermore, to calibrate model variables, a genetic algorithm can be utilized. This involves generating different samples with varying inputs (cohesion thesholds and stiffness ratios) within a specified range and prescribing them into the model. The ultimate force recorded from the model is then used to create a surrogate model. By utilizing the surrogate model and a genetic optimizer such as particle swarm optimization (PSO), the calibration of the model can be performed. The created surrogate model enables global sensitivity analysis to be conducted on the numerical model, identifying the parameters that have the highest impact on the ultimate force, as well

as those with negligible contributions. The use of genetic algorithms in geotechnical problems has been successfully demonstrated in both research and industry. Further information on utilizing genetic algorithms for geomechanical parameters can be found in ZHAO et al. 2015. Also DEM parameters calibration has been investigated in the work of CHENG et al. 2019 using Bayesian filtering framework.

The bond breaking mode was examined in this study, and it can be concluded that in all of the five samples, the majority of bond failures occurred due to the traction force surpassing the bond threshold for the normal force. Subsequently, the main cause of bond breakage was the tangential force. None of the bond failures in these samples were attributed to bending or rolling, suggesting that these factors do not play a significant role in this particular test setup. In Figure 4.24, it is evident that in test case No. 1, 84.7% of the bond failures can be attributed to traction failure, while 15.3% are a result of tangential failure, and no broken bonds in this figure can be attributed to rolling or torsion failure.

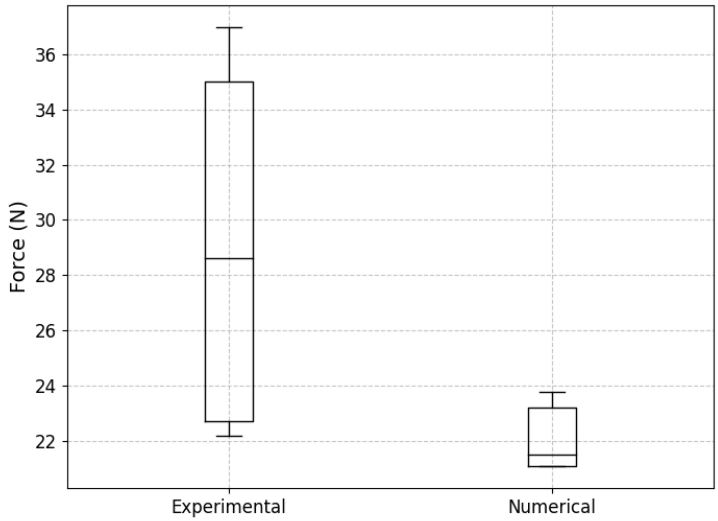

FIGURE 4.23 – Comparison of experimental and numerical results for small-sized sample with 4 mm particles and 1% paraffin content

4.2.7.2 Medium-sized samples with average diameter of 4 mm (4 ± 0.3 mm)

In a next step, several medium sized samples were generated with a friction coefficient of 0.002 and average particle diameter of 4 mm. The choice of this friction coefficient was made to ensure the creation of dense samples. Subsequently, traction simulations were conducted using the fork-join model, for 1%, 0.7 % and 0.5% paraffin content.

In the small samples, the number of bonds created throughout the model was found to be on average 10,035, with 137 of these bonds forming in the neck region.

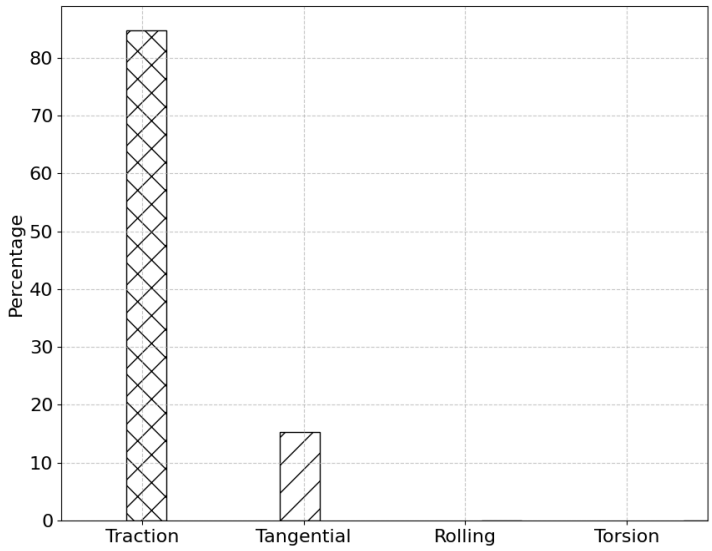

FIGURE 4.24 – Comparison of percentage of different bond breakage modes for numerical simulation of small-sized sample (test No. 1)

TABLE 4.5 – Small-sized sample macro traction simulation results

Test Name	Paraffin (%)	Mass (kg)	Friction (-)	Void ratio (-)	F_{spring} (N)	F_{ultimate} (N)	Ultimate stress (kN/m^2)
Test 1	1%	0.2973	0.002	0.557	26.6	23.8	33.6
Test 2	1%	0.2979	0.002	0.552	24.0	21.1	29.8
Test 3	1%	0.2953	0.002	0.551	26.1	23.2	32.8
Test 4	1%	0.2965	1.0	0.569	24.0	21.1	29.8
Test 5	1%	0.2967	1.0	0.566	24.4	21.5	30.4

TABLE 4.6 – Coordination numbers for generate small-sized samples

Test Name	Lower CN	Neck CN	Upper CN	Sample CN
Test 1	5.96	6.28	5.68	5.61
Test 2	5.96	5.85	5.65	5.59
Test 3	5.93	6.12	5.63	5.57
Test 4	5.91	5.59	5.63	5.55
Test 5	5.92	5.71	5.63	5.54

Similarly, in the medium sized sample, on average, a total of 42,486 cohesive bonds were detected across the entire sample, with 610 of them occurring around the neck

area. This increase in the number of bonds resulted in a higher computational cost, even when employing a pulling rate of 1 mm/s. The simulations were executed on a CPU cluster equipped with more than 20 cores and took over six hours to complete.

A medium-sized sample is illustrated in Figure 4.25, where the tube shapes represent the detected bonds between particles. The generated sample will undergo an incremental traction test until the lower cone is completely separated from the upper section of the sample. First, two simulations were conducted on two different

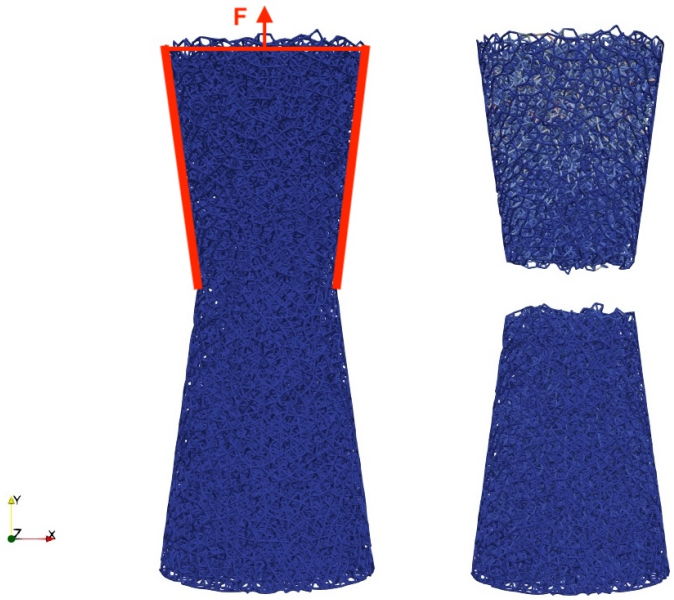

FIGURE 4.25 – Medium-sized sample traction simulation

medium-sized dense samples, both containing 1% paraffin content. Following that, three traction simulations were performed on three different dense samples with 0.5% paraffin content. Lastly, three samples with 0.7% paraffin content were investigated. For 4 mm particles with 0.7 % paraffin content only the results for micro traction tests were available and there was no micro test results for shear, bending, and torsion. The normal threshold for bonded particles with 0.7% paraffin content was set at 0.311 N (average results for micro traction test). Nonetheless, due to the absence of test results for shear, bending, and torsion, the threshold ratios established for simulations with 1% paraffin content were considered for these specific simulations. In Table 4.7 and Table 4.8, the results for these simulations are presented.

In Figure 4.26 the simulation results for the medium-sized samples are plotted, corresponding to the macro traction tests with 0.5%, 0.7%, and 1% paraffin content, as presented in Table 4.7. From these results, it is evident that the ultimate force consistently increases with the bond strength.

In Figure 4.27 comparison has been made between the experimental and simulation results for the medium-sized samples with 1% paraffin content. The findings indicate that despite having only two simulation data points, the numerical results exhibit higher values compared to the experimental outcomes. This disparity could

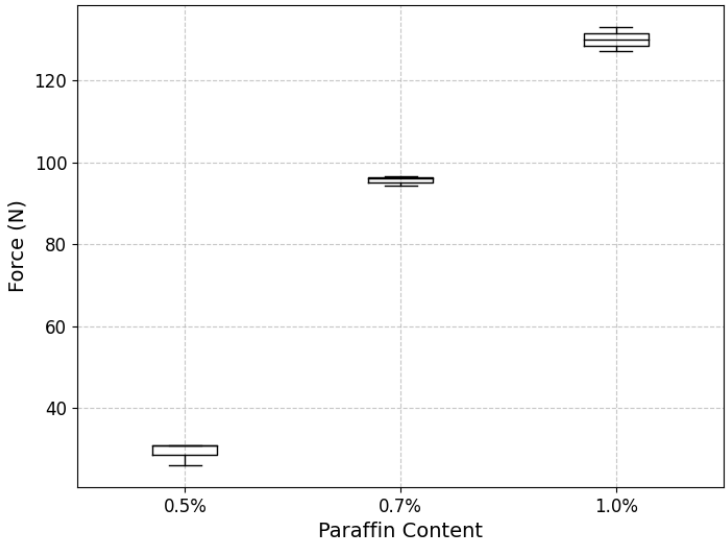

FIGURE 4.26 – Ranges of all simulation results for the medium-sized sample

be attributed to the uniform treatment of thresholds for all bonds surrounding the neck in the simulation (in this study the distribution of the bond threshold is not considered), whereas the experimental data from the micro-scale tests (see Figure 4.17) reveal a dispersion with a standard deviation of 0.21 N and an average value of 0.41 N. Furthermore, only one experimental test was conducted on the medium-sized samples with 0.7% and 0.5% paraffin content, respectively. For the numerical simulations with 0.5% paraffin content, the average result was 29.3 N, displaying a significant difference compared to the single experimental test, which yielded an ultimate force of 46.2 N. Similarly, the average simulation result for 0.7% paraffin content was 95.7 N, surpassing the outcome of the individual experiment which measured 74.0 N. It seems that for 1% and 0.7% paraffin content, the simulations overestimate the experimental ultimate force, while for 0.5% paraffin content, it is the other way around. Furthermore, in Figure 4.28, the breaking modes for a single test simulation of the medium-sized sample are depicted. As observed in Figure 4.28, similar to the small cone, the majority of bond breakages occur due to normal forces, followed by tangential forces. Similar to the small sample, neither rolling nor torsion contribute to the breakage mode.

4.2.7.3 Large-sized samples with average diameter of 4 mm (4 ± 0.3 mm)

In a last series of simulations, large-sized samples comprising over 40,000 particles are generated. The particles are released in batches of 2,000 and allowed to settle before the next batch is released. To achieve a dense sample, a friction coefficient of 0.002 is employed during the generation process. Due to the considerable time it would take to perform traction tests on the large sample, approximately one week per test, only a single simulation is performed.

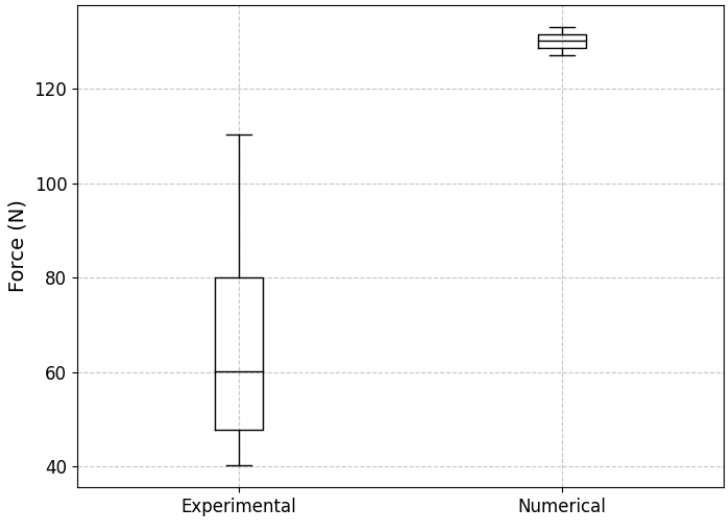

FIGURE 4.27 – Comparison of experimental and numerical results for medium-sized samples with 4 mm particles and 1% paraffin content

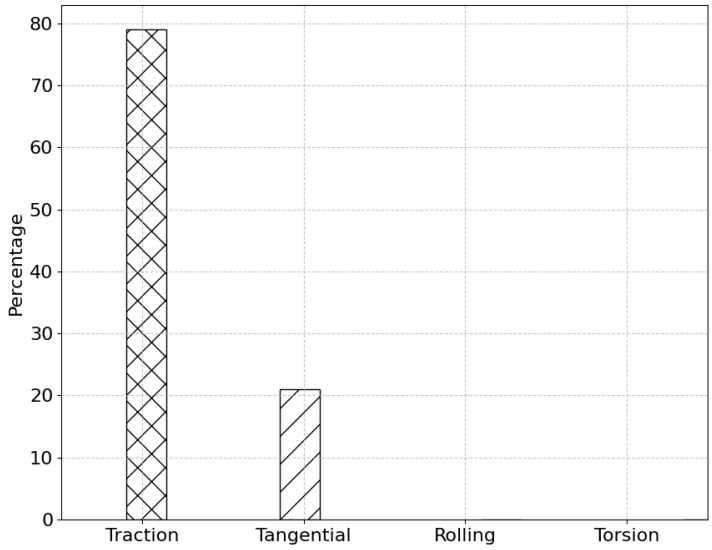

FIGURE 4.28 – Comparison of the percentage of the different bond breakage modes for numerical simulations of medium-sized samples (test No. 1 with 1% paraffin content)

Following the sample generation, it went under traction simulation with a paraffin content of 0.5% (weaker bond is chosen in order to speed up the simulation). The

TABLE 4.7 – Medium-sized macro traction test results

Test	Paraffin (%)	Mass (kg)	Friction (-)	Void ratio (-)	F_{spring} (N)	$F_{ultimate}$ (N)	σ (kN/m^2)
Test 1	1.0	0.5959	0.002	0.530	133.0	127.15	51.62
Test 2	1.0	0.5902	0.002	0.540	138.9	133.11	54.04
Test 3	0.7	0.5995	0.002	0.530	100.2	94.31	38.29
Test 4	0.7	0.5900	0.002	0.540	102.5	96.71	39.26
Test 5	0.7	0.5900	0.002	0.540	101.8	96.01	38.98
Test 6	0.5	0.5995	0.002	0.530	36.8	30.96	12.56
Test 7	0.5	0.5900	0.002	0.540	31.8	26.01	10.56
Test 8	0.5	0.5900	0.002	0.540	36.7	30.92	12.55

TABLE 4.8 – Coordination numbers for generated medium-sized samples

Test	Lower CN	Neck CN	Upper CN	Whole CN
Test 1	6.33	6.11	5.91	5.94
Test 2	6.31	6.05	5.86	5.91
Test 3	6.33	6.06	5.91	5.94
Test 4	6.32	6.10	5.86	5.91
Test 5	6.31	6.05	5.91	5.92
Test 6	6.33	6.06	5.91	5.94
Test 7	6.32	6.10	5.86	5.91
Test 8	6.31	6.05	5.91	5.92

generated large-sized sample is visualized in Figure 4.29 on the left side, while the detected cohesive bonds are shown on the right side. Notably, during the initial time step, more than 135,000 cohesive bonds are detected within this sample and almost 300 bonds are located around the neck region.

In Table 4.9, the coordination numbers for the large-sized sample are listed. The sample was subjected to a traction test using the open-mp C++ code. The ultimate traction force recorded for this sample was 178.1 N (see Table 4.10), which demonstrates a notable similarity to the experimental result of 190.7 N. Furthermore, the breaking modes for this particular test case were also investigated. Similar to the small and medium-sized samples, the breaking events predominantly occur due to normal traction force, followed by tangential force. Again, in this sample, none of the bond breakages were attributed to rolling or torsion action (see Figure 4.30).

TABLE 4.9 – Coordination numbers for generated large-sized sample

Test	Lower CN	Neck CN	Upper CN	Whole CN
Test 1	6.62	6.49	6.26	6.29

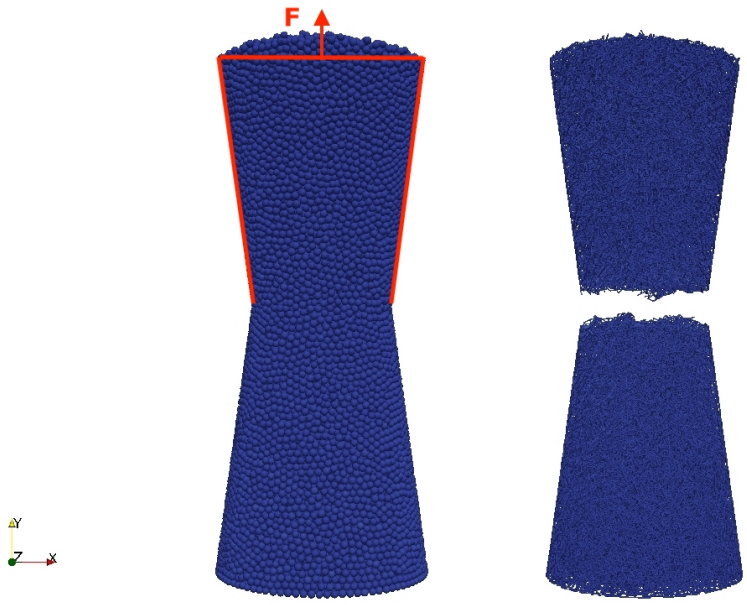

FIGURE 4.29 – Large-size sample traction simulation

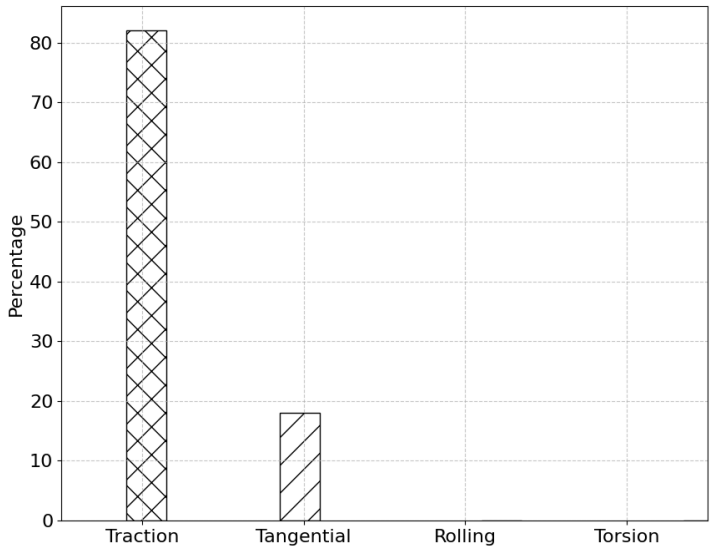

FIGURE 4.30 – Comparison of percentage of different bond breakage modes for numerical simulation of large-sized samples

4.2.8 Summary and conclusion

From the cantilever beam test results, it can be concluded that the 3D cohesion model extension from DELENNE et al. 2004 can accurately reproduce beam deflection,

TABLE 4.10 – Large-sized sample macro traction test result

Test	Paraffin (%)	Mass (kg)	Friction (-)	Void ratio (-)	F_{spring} (N)	F_{ultimate} (N)	σ (kN/m^2)
Test 1	0.5	1.2	0.002	0.540	189.9	178.1	36.33

showing strong agreement with Timoshenko beam theory.

From macro traction test results, it was observed that the void ratio and coordination number have an impact on the ultimate force results. For samples with a higher coordination number, especially around the neck — which indicates more bonds in this region — can withstand some more traction force applied by the spring. Consequently, samples with a greater coordination number around the neck exhibited a larger ultimate force from the spring. From the simulations of the small-sized samples it was evident that the ultimate force is smaller for looser samples due to lower coordination number. However, the observed difference was not more than 10% in ultimate forces.

Regarding the breakage modes, it was observed that in this particular setup, breakage due to the traction failure of the bonds was dominant, followed by the shear mode. In none of the examined samples across the three different sizes bond failures occurred due to bending or torsion. From the results for the small-sized samples, it was observed that the average numerical results were smaller than the average experimental results; however, they had acceptable agreements with each other. From the results for the medium-sized samples, it was noted that the ultimate force from numerical simulations exceeded the average of the experimental results. This discrepancy might arise from considering mono-disperse bonds throughout the sample. As observed in the micro test results, there was significant variability in the traction test results. In the future, it might be beneficial to simulate this setup using polydispersed bond thresholds. It might also be advantageous to test an additional cohesion damage model in this setup. This would entail that, during the test, the bonds affected by the spring would degrade during the simulation. In a real-world scenario, this could represent the effect of micro-cracks occurring in the bond. Such damage model was previously implemented in the 2D Delenne model, as discussed in the work of BENSEGHIER 2019. For the large-sized sample, the simulation result aligns well with the experimental outcome. However, only one experimental test was conducted for 0.5% paraffin content, and there was just one simulation for this content. The agreement between these results should be validated with additional tests and simulations. Additionally, reducing the pulling rate to align more closely with the experimental procedure might be advisable. While these simulations might be more time-consuming, it could enhance result accuracy and mitigate dynamic effects in larger simulations.

Apart from comparison with experimental results, it is also interesting to check whether a unique ultimate tensile stress value can be obtained in the numerical simulations, irrespective of sample size. Clearly, the values provided by the simulations show that this is far from being the case. Traction simulations at 1% paraffin content for

small and medium sample sizes provide values of around 32 kN/m^2 and 53 kN/m^2, respectively. Similarly, for 0.5% paraffin content, approximately 12 kN/m^2 and 36 kN/m^2 was found for the ultimate stress in the medium and large-sized samples. It, therefore, seems that the ultimate tensile stress increases with sample size, suggesting significant edge effects in the separation zone between the two cones, that would require specific investigation.

It was evident from experimental results that the ultimate forces for both micro and macro tests varied considerably. Although the number of simulations carried out here is still small, there seems to be comparatively less dispersion in the final values obtained. Optimizing a model based on such dispersed results will undoubtedly be challenging. However, leveraging optimization techniques like genetic algorithms or Bayesian filtering, as mentioned earlier, could be instrumental in aligning numerical model results more closely with experimental findings.

5 Numerical simulations of suction buckets

Contents

5.1 Introduction

In this chapter, the developed 3D cohesion model is integrated into the open-source software waLBerla and coupled with the fluid. According to BAUER et al. 2021, waLBerla is a framework that supports complex multiphysics simulations, designed to harness the full power of supercomputers. This framework operates with massive parallelism and, when run locally, optimizes the use of available hardware. It employs a distributed data structure, ensuring that each process holds information only about local and adjacent data. Consequently, the memory usage of each process is independent of the overall simulation size, ensuring impressive scalability. For parallelization, waLBerla leverages both MPI (Message Passing Interface) and OpenMP. Although its primary focus is on fluid dynamics simulations using LBM, the framework also includes DEM for particle simulations and a coupled version of LBM and DEM. Additionally, waLBerla employs adaptive meshing, dynamically refining or coarsening the mesh based on simulation requirements within specific regions and domains. The software's first prototype was developed in 2007 and was released as open source in 2017. Further details about waLBerla can be found in BAUER et al. 2021. The cohesion model wasn't previously integrated into waLBerla. This study represents the first effort to introduce it into the open-source framework. While this is a significant step, there are some issues and limitations, discussed later, that future research should address to optimize the performance and capabilities of waLBerla.

5.2 Case study description

In this section, a test case similar to the work of FUKUMOTO et al. 2021 is studied to evaluate the performance of the coupled DEM-LBM approach with a cohesion model in scenarios involving the installation of suction buckets. The test also aims to investigate the occurrence of local piping during the installation process. In Fukumoto's study, a coupled 2D fluid and particle simulation approach is used to explore the occurrence of seepage failure in horizontally oriented ground containing an embedded sheet pile. According to this study, such seepage failures can lead to significant geotechnical hazards, including the potential collapse of dam structures. The test setup in this simulation could also be applicable to suction buckets, assuming that a slice of the bucket wall is simulated. This would allow for the investigation of soil deformation both inside and outside the bucket, with and without cementation in the sand, through the pressure difference between the inside and outside of the bucket.

Firstly, the test setup from Fukumoto's study will be explained. The system examined in this model, as shown in Figure 5.1, consists of a 2D domain with dimensions $200 \times 100\,\text{mm}$ (width × height), enclosed by four walls. A fixed sheet pile wall, with dimensions $65\,\text{mm} \times 5\,\text{mm}$, is positioned in the center of the domain to obstruct water flow. This wall remains undeformed throughout the simulation. Initially, the domain is filled only with particles having a density of $2500\,\text{kg/m}^3$, subjected to gravity, up to a height of 50 mm (with no fluid). The diameter of the particles varied between

D_{min} = 0.5 mm and D_{max} = 0.6 mm considering real-life particle sizes. It should be noted that, in Fukumoto's work, no cementation or cohesive bonds between particles were considered. These particle assemblies were generated with three different void ratios (e_{ini} = 0.18, 0.20, and 0.22) to study the impact of increased spacing between loose particles. The number of particles in these three samples was 38781, 37586, and 36385, respectively. The friction coefficient between particles was assumed to be $\mu = 0.6$, and the stiffness ratio between the normal and tangential forces for the particles was $k_n/k_t = 4$, where $k_n = 5 \times 10^6$. In the next step, these generated samples were coupled with fluid, filling the entire domain. For the study of FUKUMOTO et al. 2021, a lattice spacing of $d_x = 5.0 \times 10^{-5}$ m and a lattice time of $d_t = 5.0 \times 10^{-7}$ s were chosen. The objective of this study was to identify the critical hydraulic gradient needed to create quicksand near the edge of the wall. To investigate this, fluid flow was generated by a difference in hydraulic head, as discussed in ZOU and HE 1997. An inlet was positioned on the upper wall domain at the left side of the sheet pile, and an outlet was located on the right side. The remaining walls of the domain were subject to a non-slip boundary condition. A pressure difference (ΔP) was applied through the inlet and outlet, and the movement of particles adjacent to the wall (10 mm to the left and right) was monitored. The hydraulic gradient i was calculated as follows:

$$i = \frac{1}{\rho_f g} \frac{\Delta P}{L_s}, \tag{5.1}$$

where $g = 9.81\,\mathrm{m/s^2}$ represents the gravitational acceleration, ρ_f is fluid density, and ΔP signifies the pressure difference imposed between the inflow and outflow. In this context, L_s denotes the path length of the seepage flow, which corresponds to the shortest path around the sheet pile. As illustrated in Figure 5.1, this length measures 35 mm (15 mm + 5 mm + 15 mm). At the beginning of the simulation, the system was set in a quiescent state with fluid density $\rho = 1000\,\mathrm{kg/m^3}$ and a fluid velocity of $u = 0\,\mathrm{m/s}$. Subsequently, a pressure difference of $\Delta P = 0 - 1000\,\mathrm{Pa}$ was imposed over a duration of 3 seconds.

According to the results, initially, boiling and heaving emerged near the sheet pile downstream, and after increasing the pressure difference, quicksand emerged within the corner areas of the wall (Figure 5.2). The evolution of average displacement (uplift) as a function of the hydraulic gradient is depicted in Figure 5.3 for the three different samples, each with a distinct void ratio. From these plots, it is evident that quicksand emerged at the edge of the wall for these samples when i (hydraulic gradient) was between 1.5 and 2.0 which means the pressure difference ΔP was between 500 Pa or 690 Pa.

In the current study a 3D test case with general similarity to FUKUMOTO et al. 2021 is chosen for demonstration of the code functionality and for investigation of piping erosion around the wall-tip of a stationary bucket embedded to a certain depth into cemented and non-cemented sands. The model detail will be explained in the next section.

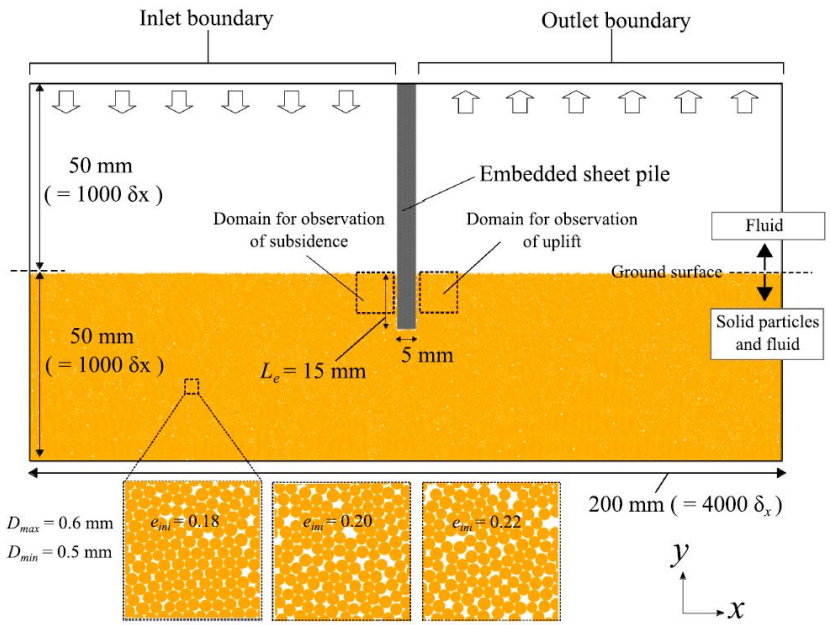

FIGURE 5.1 – Initial configuration of simulation model for seepage failure around embedded sheet pile using coupled LBM-DEM model (FUKUMOTO et al. 2021)

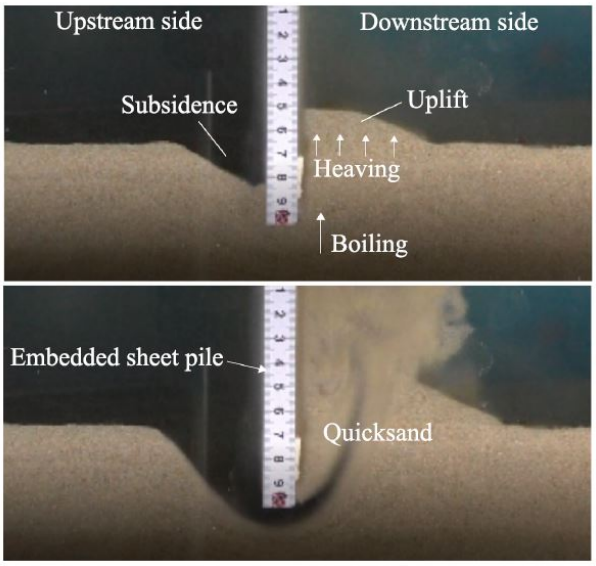

FIGURE 5.2 – Seepage failure of horizontal ground with embedded sheet pile (FUKUMOTO et al. 2021)

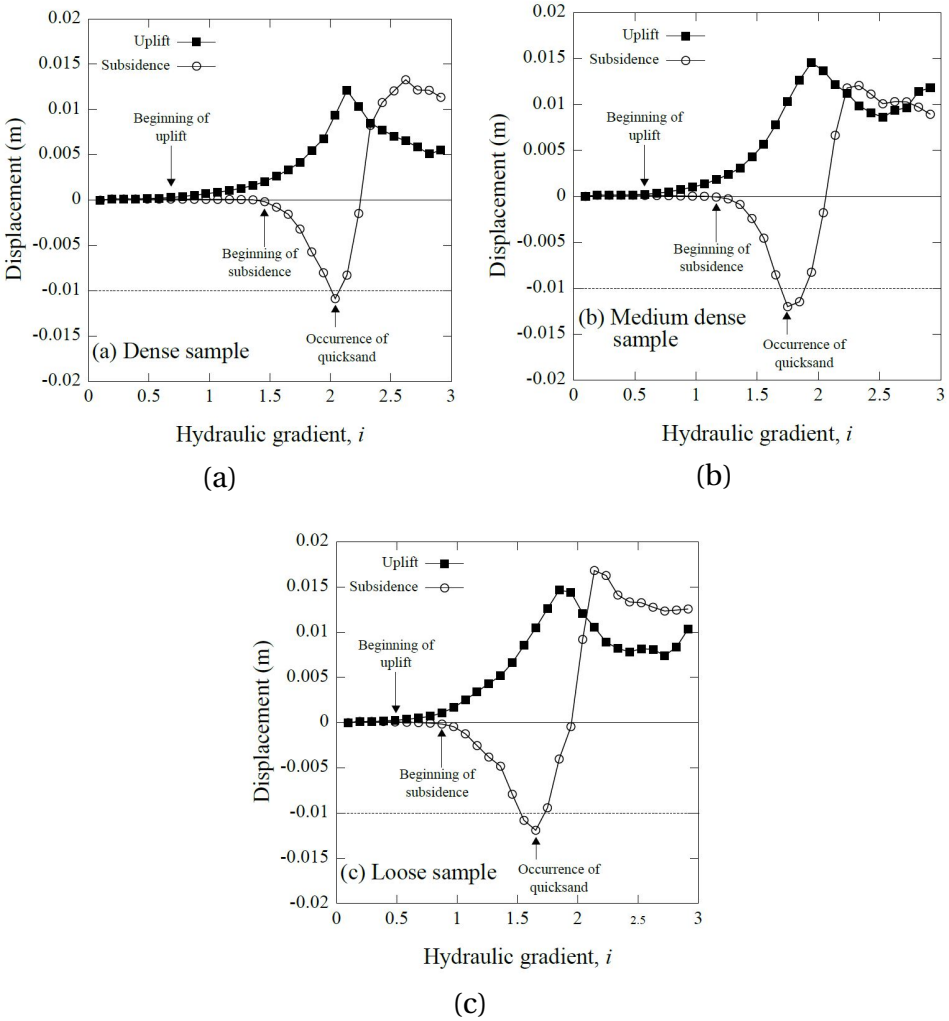

FIGURE 5.3 – Evolution of uplift against hydraulic gradient for (a) $e_{ini} = 0.18$ (b) $e_{ini} = 0.20$, and (c) $e_{ini} = 0.22$ (FUKUMOTO et al. 2021)

5.3 Numerical simulation setup

The setup considered in the present study is illustrated in Figure 5.4. All the simulations were run on a personal laptop (MacBook M1 Plus). To facilitate the running of these simulations on a local computer, several adjustments were necessary. Initially, a domain of size 80 mm × 12 mm × 50 mm was chosen, with a rigid box wall in the middle with dimensions of 80 mm × 12 mm × 35 mm.

In Fukumoto's study, the grain sizes were relatively small ($D_{\text{min}} = 0.5$ mm and $D_{\text{max}} = 0.6$ mm). However, creating particles with these diameters in 3D is both time and memory demanding. Therefore, the diameter of the particles was chosen to be between $D_{\text{min}} = 1.8$ mm and $D_{\text{max}} = 2.2$ mm. Particle packing was created solely under the force of gravity, without fluid with submerged (buoyant) density. The stiffness of the particles during interaction was calculated based on ŠMILAUER and CHAREYRE

2010. According to this documentation, the stiffness K_n can be calculated as follows:

$$K_n = 2 \times E \times R_{\text{eff}} \tag{5.2}$$

where effective radius, $R_{\text{eff}} = \frac{R_i R_j}{R_i + R_j}$ and E is the Young's modulus.

One limitation of the current cohesion kernel in waLBerla is that it does not support a Young's modulus $E > 10^4$ kgm/s^2, leading to errors in the LBM kernel. This issue remains unresolved and must be addressed in future studies. For this study, a Young's modulus $E = 10^4$ kgm/s^2 was selected. The damping ratio between particles is calculated based on Equation 2.5, as described in previous chapters.

Two samples were generated with different void ratios of $e_{\text{ini}} = 0.64$ and $e_{\text{ini}} = 0.67$, comprising 3465 and 3267 particles, respectively. The approach for calculating the void ratio will be briefly explained in the next subsection. The friction coefficient for the dense sample is set to $\mu = 0.5$, while for the looser sample, it is $\mu = 1.0$. Upon generating the samples, the solid-fluid model was initialized. In this study, the lattice space $d_x = 2 \times 10^{-4}$ m, lattice time $d_t = 5 \times 10^{-5}$ s and fluid density of $\rho_f = 1000$ kg/m^3 were chosen. Attempts to refine the lattice space to a smaller value, closer to that in Fukumoto's study, resulted in memory deficiencies on the computer used. For the LBM model the D3Q19 BGK (SRT or single relaxation time) model was used, with a relaxation time $\tau = 0.5006$ and a kinematic viscosity $\nu = 10^{-5}$ (Rettinger and Ruede 2017). To create a flow within the domain, a difference in hydraulic head between the inflow and outflow, similar to Fukumoto's test case, is generated. The rest of the boundaries within the domain are subject to non-slip conditions. Another limitation of this test case, compared to real-life studies, is that the bucket remains stationary and does not penetrate through the sandy bed. Unlike in Fukumoto's study, where the pressure difference between the inlet and outlet, ΔP, was varied from 0 to 1000 Pa over 3 seconds during one simulation, the pressure difference in this study must remain constant throughout each simulation because applying a dynamic pressure difference between the inlet and outlet during one simulation was not possible in waLBerla for the implemented cohesion kernel. To address this, three different values of ΔP are prescribed for each test case: for the first case, $\Delta P = 800$ Pa; for the second, $\Delta P = 1400$ Pa; and for the third, $\Delta P = 1800$ Pa. These three values are chosen based on trial and error with the model.

Each simulation is run until no sudden movements within the particles are detected. This condition is monitored through the average velocity of the particles throughout the simulations. After each simulation, the hydraulic gradient i is calculated based on the pressure difference ΔP, the gravitational constant $g = 9.81$ m/s^2, the fluid density ρ_f, and the length $L_s = L_1 + L_2 + L_3$ (see Figure 5.4). In the case of cohesive sand, a cohesion threshold of $C_n = 0.2$ N is applied to all detected bonds. All the DEM-LBM variables used in these simulations are listed in Table 5.1. The rolling and torsion thresholds are calculated using Equation 4.3 and considering $\alpha = 0.25$.

The numerical simulation for the coupled DEM-LBM is available in Sanayei 2023, within the *04-coupled-model-walberla* folder. The source code for the cohesion kernel and its initialization can be found in the *src/mesa_pd/kernel/* directory, with filenames

CohesionInitialization.h and *Cohesion.h*. The code for sample generation is located in the *apps/showcases/PipingErosion/* directory under the name *BedGenerationPipingErosion.cpp*, while the coupled simulation can be found in the same directory with the filename *PipingErosion.cpp*. For further details regarding waLBerla installation and setup, please refer to its main page at *https: //walberla.net*.

TABLE 5.1 – Bucket simulation parameters

Parameter	**Value**
E	10^4 kgm/s^2
μ_s	0.5
μ_r	0.1
K_s/K_n	0.5
$K_r/K_n = K_o/K_n$	0.1
ρ_s	2500 kg/m^3
ρ_f	1000 kg/m^3
d_x	2×10^{-4}
d_t	5×10^{-5}
τ	0.5006
ν	10^{-5}
DEM sub-cycles	10
C_n	0.2 N
C_s/C_n	0.5

Calculating the average void ratio of the sample

To calculate the void ratio in this sample, the first step is to determine the volume of the region filled with particles. To do this, the maximum particle height on both the left and the right sides of the particle packing are identified, denoted as z_{left} and z_{right} (see Figure 5.5). The average particle height in the domain is then calculated using $z = \frac{z_{\text{left}} + z_{\text{right}}}{2}$. The domain volume V_d is given by $V_d = \mathrm{D}_x \times \mathrm{D}_y \times z$, where D_x and D_y are 80 mm and 50 mm in this simulation setup. The solid volume (the volume occupied by particles) is calculated using $V_s = \sum_{i \to n} \frac{4}{3}\pi r_i^3$, where n is the number of particles. The void volume can be calculated as $V_v = V_d - V_s$. Finally, the void ratio can be determined using $e_{\text{ini}} = \frac{V_v}{V_s}$.

5.4 Results and discussions

In this section, the two generated packing samples with $e_{\text{ini}} = 0.64$ and $e_{\text{ini}} = 0.67$ are tested against three different pressures ($\Delta P = 800\,\text{Pa}$, $\Delta P = 1400\,\text{Pa}$, $\Delta P = 1800\,\text{Pa}$), and the heave inside the bucket is determined at both the beginning and the end of each simulation. Each simulation is set to run for 10 seconds. However, running this test

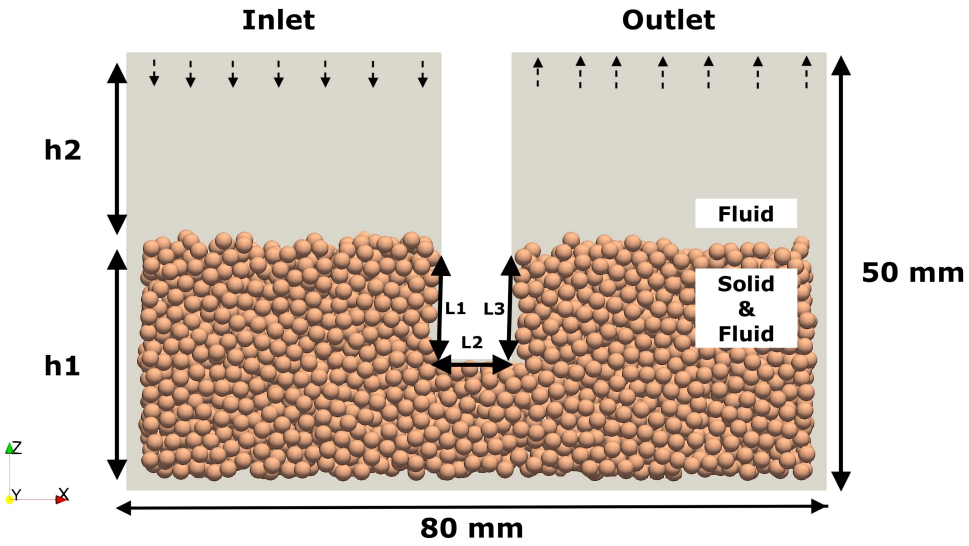

FIGURE 5.4 – Bucket test setup

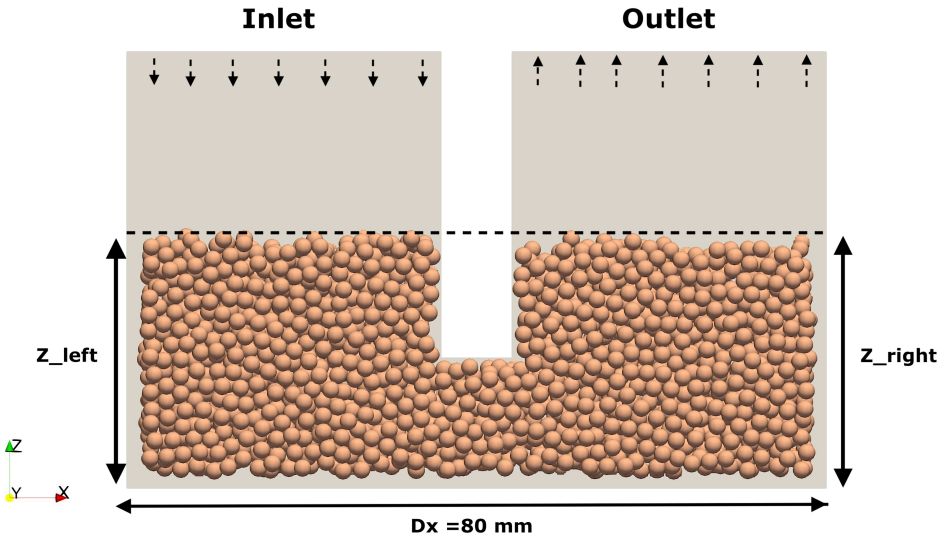

FIGURE 5.5 – Calculating void ratio

setup for 10 seconds on a local computer takes over 3 days for each test case when using an M1 chip, according to waLBerla estimators. Interestingly, it takes up to 20 days on an 8-core laptop with a standard chip. To save time, the motion of the particles

is monitored at fixed intervals during the simulation. The simulation is stopped when the average velocity of the particles reaches nearly zero and does not change for an extended period. After each simulation, the hydraulic gradient and heave inside the bucket are determined. Each generated sample is tested using the parameters listed in Table 5.1, both with and without activated cohesion.

The results are presented in Figure 5.6. In Figure 5.6 (*a*), the evolution of uplift inside the bucket versus the hydraulic gradient for the sample with $e_{\text{ini}} = 0.64$ is demonstrated. In this sample, for a hydraulic gradient of 5.06 (corresponding to $\Delta P = 1800\,\text{Pa}$), piping occurs at the edge of the wall. However, if cohesion is activated, meaning that overlapping particles are considered bonded during the very first time step, no piping occurs. For the other sample with $e_{\text{ini}} = 0.67$, generated by increasing the friction coefficient from $\mu = 0.5$ to $\mu = 1.0$, piping (quicksand) occurs at a lower gradient $i = 3.36$, corresponding to $\Delta P = 1400\,\text{Pa}$ (Figure 5.6 (*b*)). Similar to the previous sample, no quicksand occurrence was detected when cohesion between particles was activated. Figure 5.7 shows the shape of the emerging quicksand for the sample with $e_{\text{ini}} = 0.64$ at $\Delta P = 1800\,\text{Pa}$. Under the same conditions, cohesion prevented the occurrence of quicksand in the bucket.

By comparing the results of the two different samples, it can be concluded that the void ratio and the geometry of the sample near the wall can significantly affect the occurrence of quicksand. In these samples, it was observed that cemented sand in the seabed can prevent the occurrence of piping for a given embedment ratio. However, this should be investigated in greater detail and with a more realistic setup, such as a moving bucket. This is because cementation can resist wall penetration through the seabed, and with slow-rate pumping, as observed in the study by Tran 2005, piping can emerge due to the much higher force required to force the wall to penetrate the seabed. Remaining issues, such as the correct Young's modulus, should be resolved in waLBerla. Moreover, using supercomputers, more refined and realistically-sized samples must be generated to obtain more reliable results. The effect of bucket geometry on heave inside the bucket is also investigated in this study and will be explained in the next section.

5.5 Investigating the impact of bucket geometry on uplift phenomena

As explained in the state of the art, research by Tran 2005 suggests that an increase in bucket thickness leads to a corresponding increase in sand heave within the bucket (see Section 1.5.3). The study was conducted in a cohesionless sandy bed, examining bucket thicknesses of 0.8 mm and 1.6 mm. In another work by Tran 2005, the focus shifted to variations in bucket diameter while keeping the wall thickness constant.

The current study explored sand heave in buckets with wall thicknesses of 1 mm, 4 mm, and 8 mm ($t/D = 1.25\%, 5\%, 10\%$) in cohesive sand. The methodology remained largely the same as in earlier setups. Pressure differences of $\Delta P = 1800\,\text{Pa}$ and $\Delta P = 3200\,\text{Pa}$ were applied to investigate larger uplift values. A sample with a void ratio

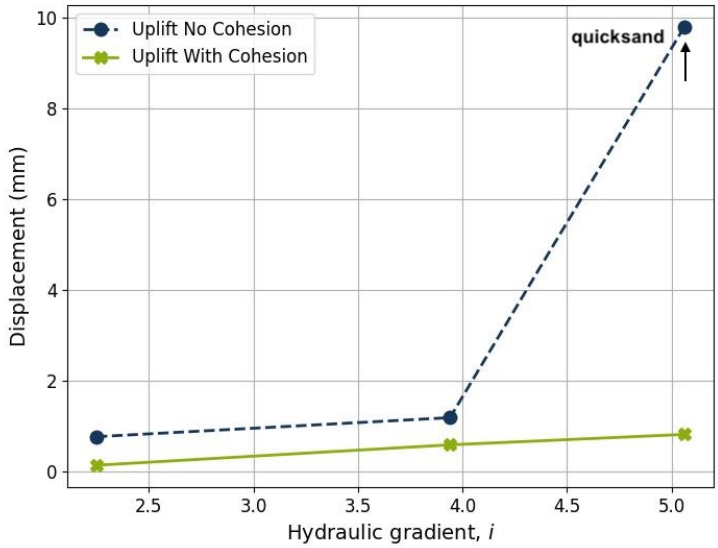

(a) $e_{ini} = 0.64$

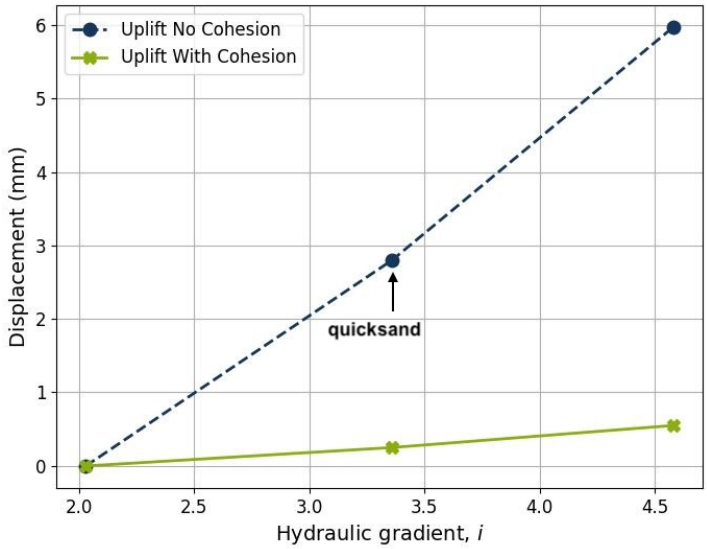

(b) $e_{ini} = 0.67$

FIGURE 5.6 – Evolution of uplift against hydraulic gradient for (a) $e_{ini} = 0.64$ and (b) $e_{ini} = 0.67$

of $e_{\text{ini}} = 0.64$ was used for these simulations. Both the internal uplift and hydraulic gradient were monitored, similar to previous experiments.

The simulations ran on a single computer for 10 seconds simulation time. Given the computational demands, completing the test could take up to three days on a single computer. To streamline the process, the average particle velocity was recorded at

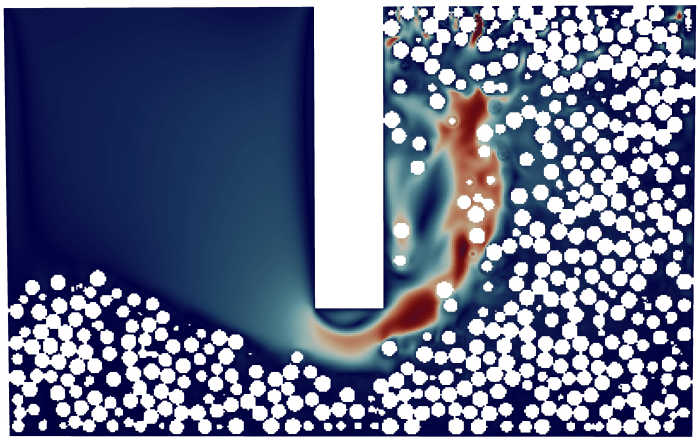

(a) No Cohesion

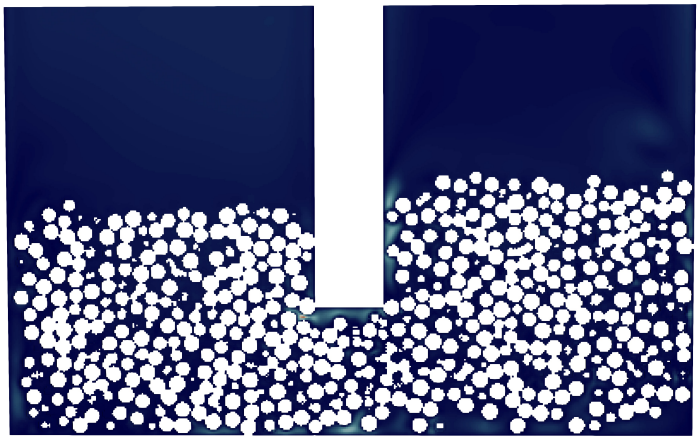

(b) With Cohesion

FIGURE 5.7 – Comparing the simulations with $\Delta P = 1800\,\text{Pa}$ for the sample with $e_{\text{ini}} = 0.64$ with and without cohesion

fixed intervals. The simulation was halted when this velocity approached a near-zero value and remained unchanged for a period.

The outcomes of these simulations are presented in Figure 5.8. The results show no significant differences between the tested scenarios. At $\Delta P = 1800\,\text{Pa}$, all buckets displayed minimal internal uplift, although the 8 mm thick bucket showed a marginally smaller heave. When the pressure difference was elevated to $\Delta P = 3200\,\text{Pa}$, the uplift increased noticeably across all test cases. Quicksand formation was not observed in any of the simulations. However, the 8 mm bucket showed a slightly higher uplift, followed by the 4 mm and then the 1 mm buckets.

Further details on the shape of the uplift across different scenarios can be found in Figure 5.9. To align more closely with Tran's work, future simulations could benefit from allowing bucket penetration through the soil and refining particle sizes with the help of supercomputers. Additionally, adjustments to the Young's modulus in the

current cohesion kernel in waLBerla are necessary to avoid potential inaccuracies.

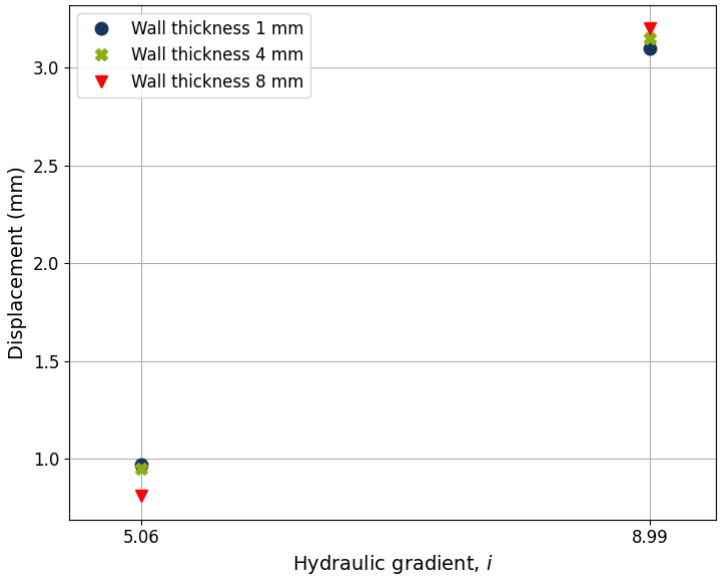

FIGURE 5.8 – Evolution of uplift against hydraulic gradient across walls of varying thickness

5.6 Summary and conclusion

In this section, a test case similar to the investigations by FUKUMOTO et al. 2021 on the seepage effect on sheet piles was used to study piping erosion, and the formation of uplift (heave) inside suction buckets in both non-cohesive and cohesive sands in 3D. Due to limitations in computing power, several adjustments were made to the model, such as increasing the average diameter of the particles within the domain. The current cohesion kernel implemented in waLBerla has some deficiencies, such as errors when using large and realistic Young's modulus values in the simulations. These issues will need to be addressed in future studies.

Based on the current study, it can be concluded that the void ratio has a significant effect on the formation of quicksand (piping erosion) near the bucket walls. It was also observed that cohesion within the sand can prevent the formation of quicksand (piping channels) and failure of the bucket. In scenarios with large pressure differences between the inside and outside of the bucket, it was observed that buckets with thinner walls experience less heave. This is important to note because, as seen in the study by TRAN 2005, jetting techniques may be necessary to mitigate heave and avoid bucket installation failure. Future studies should allow the bucket to penetrate through the soil. Although cohesion helps in avoiding piping erosion in this study, slow wall

movement through the bed (using a small pumping rate) might hinder penetration, as observed in Tran's study, leading to the formation of piping channels or significant heave inside the bucket.

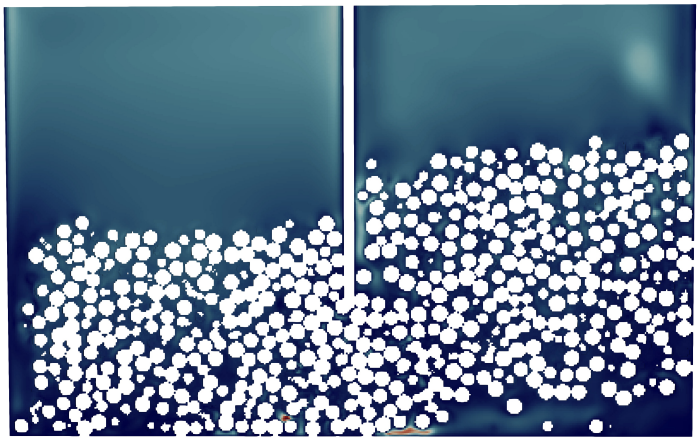

(a) Wall thickness = 1 mm

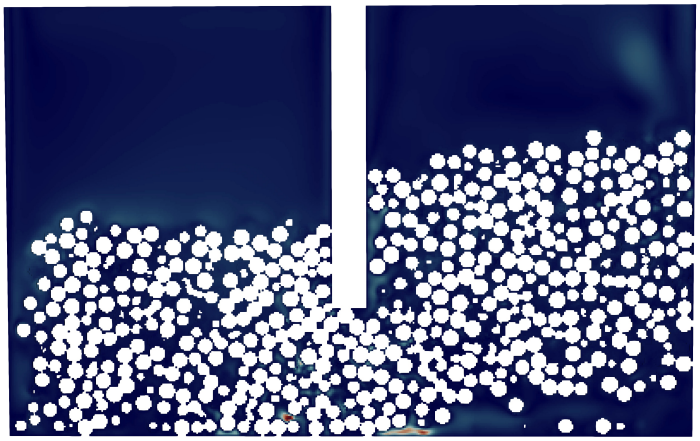

(b) Wall thickness = 4 mm

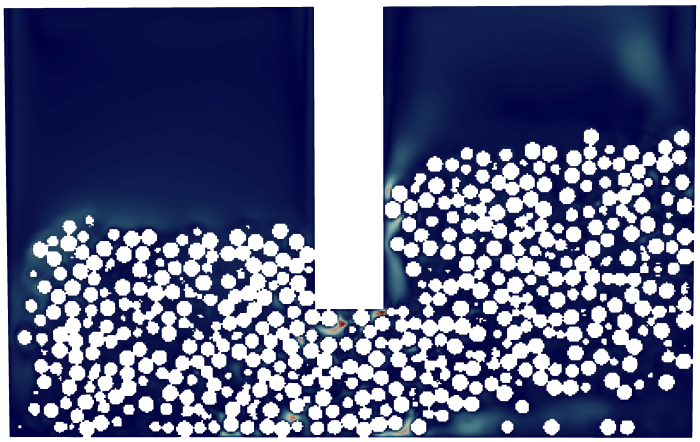

(c) Wall thickness = 8 mm

FIGURE 5.9 – Comparing uplift in a sample with initial void ratio $e_{ini} = 0.64$ across walls of varying thickness.

Conclusion

As observed during this study, the extended 3D cohesion model performed accurately in the cantilever beam deflection test and produced realistic results with good accuracy in the macro traction test. Although the results from the micro and macro traction experiments were quite dispersed, the developed model of the macro traction tests was able to reproduce brittle breakage and the separation of cones from each other. The ultimate forces from the simulations for three different-sized samples were generally in good agreement with the experimental results, however, there is still room for improvement in these test case simulations. These improvements could be achieved by utilizing a damage model or by using poly-disperse bonds, which feature several bonds with different breakage thresholds throughout the sample. Given the dispersion of the micro-test results, it may not be advisable to choose average values for the bond thresholds. Instead, these numbers might be more effectively determined through calibration and optimization techniques such as genetic algorithms. Additionally, transferring traction simulation similar to sample generation to the GPU could improve the model's time efficiency. This could also allow for a reduction in the spring's incremental pulling rate, bringing it closer to real-life rates.

The first version of the coupled DEM-LBM model in waLBerla showed promising results. However, there are still deficiencies in the suction bucket simulations as well as in the cohesion kernel within waLBerla. First, the cohesion kernel cannot handle large Young's modulus, making it unsuitable for simulating rigid contacts. Second, compared to previously developed DEM kernels in waLBerla, the cohesion kernel is relatively slow. These issues suggest that improvements are needed to speed up the solid-part simulations. In the bucket simulations, it is currently not possible to change the internal pressure over time; the pressure remains constant. So, in order to simulate suction buckets effectively, different simulations with varying pressure differences must be employed. Additionally, the bucket needs to penetrate through the soil for a more realistic setup. Addressing these issues and utilizing supercomputers could make it possible to simulate bucket installations more closely aligned with real-life-sized test setups and with finer grains.

Bibliographie

[1] K. ANDERSEN, J. MURFF, M. RANDOLPH, E. CLUKEY, C. ERBRICH, H. JOSTAD, B. HANSEN, C. AUBENY, P. SHARMA and C. SUPACHAWAROTE. « Suction anchors for deepwater applications ». In : *Proceedings of the 1st international symposium on frontiers in offshore geotechnics, ISFOG, Perth*. 2005, p. 3-30 (cf. p. 23).

[2] M. BAUER, S. EIBL, C. GODENSCHWAGER, N. KOHL, M. KURON, C. RETTINGER, F. SCHORNBAUM, C. SCHWARZMEIER, D. THÖNNES, H. KÖSTLER et al. « waLBerla : A block-structured high-performance framework for multiphysics simulations ». In : *Computers & Mathematics with Applications* 81 (2021), p. 478-501 (cf. p. 39, 104).

[3] J. BECKER. « Development and implementation of new simulation possibilities in the CAST program package ». Thèse de doct. Universität Würzburg, 2015 (cf. p. 67-69, 71).

[4] Z. BENSEGHIER. « Etude numérique de l'érosion d'un matériau granulaire cohésif par un écoulement fluide ». Thèse de doct. Aix-Marseille, 2019 (cf. p. 19, 53, 59, 62, 101).

[5] Z. BENSEGHIER, P. CUÉLLAR, L.-H. LUU, S. BONELLI and P. PHILIPPE. « A parallel GPU-based computational framework for the micromechanical analysis of geotechnical and erosion problems ». In : *Computers and Geotechnics* 120 (2020), p. 103404 (cf. p. 50, 59-61, 86).

[6] M. BÖHM, P. SCHAUMANN and E. GHAFOORI. « Shell buckling of suction buckets for offshore wind turbines considering imperfection and soil parameter sensitivity ». In : *Engineering Structures* 302 (2024), p. 117310 (cf. p. 24).

[7] M. BOUZIDI, M. FIRDAOUSS and P. LALLEMAND. « Momentum transfer of a Boltzmann-lattice fluid with boundaries ». In : *Physics of Fluids* 13.11 (2001), p. 3452-3459 (cf. p. 59).

[8] G. A. BROWN and V. A. NACCI. « Performance of hydrostatic anchors in granular soils ». In : *Offshore Technology Conference*. OTC. 1971, OTC-1472 (cf. p. 24).

[9] F. BRUNIER-COULIN. « Etude des mécanismes élémentaires de l'érosion d'un sol cohésif ». Thèse de doct. Aix-Marseille, 2016 (cf. p. 78, 79).

[10] B. BYRNE, G. HOULSBY, C. MARTIN and P. FISH. « Suction caisson foundations for offshore wind turbines ». In : *Wind Engineering* 26.3 (2002), p. 145-155 (cf. p. 24).

[11] X. CHEN, D. PENG, J. P. MORRISSEY and J. Y. OOI. « A comparative assessment and unification of bond models in DEM simulations ». In : *Granular Matter* 24 (2022), p. 1-20 (cf. p. 74-77).

[12] H. CHENG, T. SHUKU, K. THOENI, P. TEMPONE, S. LUDING and V. MAGNANIMO. « An iterative Bayesian filtering framework for fast and automated calibration of DEM models ». In : *Computer Methods in Applied Mechanics and Engineering* 350 (2019), p. 268-294 (cf. p. 94).

[13] J. CHENG, M. GROSSMAN and T. MCKERCHER. *Professional CUDA c programming*. John Wiley & Sons, 2014 (cf. p. 64-66).

[14] P. A. CUNDALL and O. D. STRACK. « A discrete numerical model for granular assemblies ». In : *Géotechnique* 29.1 (1979), p. 47-65 (cf. p. 42).

[15] J.-Y. DELENNE, M. S. EL YOUSSOUFI, F. CHERBLANC and J.-C. BÉNET. « Mechanical behaviour and failure of cohesive granular materials ». In : *International Journal for Numerical and Analytical Methods in Geomechanics* 28.15 (2004), p. 1577-1594 (cf. p. 19, 49, 74-77, 90, 100).

[16] W. DENG and J. CARTER. « Inclined uplift capacity of suction caissons in sand ». In : *Offshore Technology Conference*. OTC. 2000, OTC-12196 (cf. p. 24, 86).

[17] W. ECKHARDT, A. HEINECKE, R. BADER, M. BREHM, N. HAMMER, H. HUBER, H.-G. KLEINHENZ, J. VRABEC, H. HASSE, M. HORSCH et al. « 591 TFLOPS multi-trillion particles simulation on SuperMUC ». In : *Supercomputing : 28th International Supercomputing Conference, ISC 2013, Leipzig, Germany, June 16-20, 2013. Proceedings 28*. Springer. 2013, p. 1-12 (cf. p. 67).

[18] H. FAN and J. WANG. « Dynamic modeling of sphere, cylinder, cone, and their assembly ». In : *Archives of Computational Methods in Engineering* 27 (2020), p. 725-772 (cf. p. 87).

[19] A. FARHAT. *Experimental characterization of the cohesion bonds at Micro and Macroscopic scales*. Technical Report. 2020 (cf. p. 78, 81, 82).

[20] A. FARHAT. « Fluidization and erosion of layered hydraulic earthworks. Experimental characterization and micromechanical simulation ». Thèse de doct. Aix-Marseille, 2023 (cf. p. 78-81, 83).

[21] A. FARHAT, L.-H. LUU, P. PHILIPPE and P. CUÉLLAR. « Multi-scale cohesion force measurements for cemented granular materials ». In : *EPJ Web of Conferences*. T. 249. EDP Sciences. 2021, p. 08008 (cf. p. 78).

[22] Y. FUKUMOTO, H. YANG, T. HOSOYAMADA and S. OHTSUKA. « 2-D coupled fluid-particle numerical analysis of seepage failure of saturated granular soils around an embedded sheet pile with no macroscopic assumptions ». In : *Computers and Geotechnics* 136 (2021), p. 104234 (cf. p. 104-107, 114).

[23] I. GINZBURG, F. VERHAEGHE and D. D'HUMIERES. « Two-relaxation-time lattice Boltzmann scheme : About parametrization, velocity, pressure and mixed boundary conditions ». In : *Communications in Computational Physics* 3.2 (2008), p. 427-478 (cf. p. 53).

[24] J. Z. GONZÁLEZ. « Suction Bucket lid plate design and welding automation ». Mém. de mast. Aalborg Universitet, Master thesis, 2017 (cf. p. 22, 23).

[25] L. GOODMAN, C. LEE and F. WALKER. « The feasibility of vacuum anchorage in soil ». In : *Geotechnique* 1.4 (1961), p. 356-359 (cf. p. 24).

[26] J. HOGERVORST. « Field trails with large diameter suction piles ». In : *Offshore Technology Conference*. OTC. 1980, OTC-3817 (cf. p. 25).

[27] C. HOLM. *Simulation Methods in Physics 1*. 2013. URL : https://www2.icp.uni-stuttgart.de/~icp/mediawiki/images/5/54/Skript_sim_methods_I.pdf (cf. p. 47).

[28] L. B. IBSEN and C. THILSTED. « Numerical study of piping limits for suction installation of offshore skirted foundations and anchors in layered sand ». In : *Frontiers in Offshore Geotechnics, II* (2010), p. 421-426 (cf. p. 33).

[29] M. ISKANDER, S. EL-GHARBAWY and R. OLSON. « Performance of suction caissons in sand and clay ». In : *Canadian Geotechnical Journal* 39.3 (2002), p. 576-584 (cf. p. 24).

[30] R. KELLY, B. BYRNE, G. HOULSBY and C. MARTIN. « Tensile loading of model caisson foundations for structures on sand ». In : *ISOPE International Ocean and Polar Engineering Conference*. ISOPE. 2004, ISOPE-I (cf. p. 24).

[31] J. H. KIM and D. S. KIM. « Soil plug heave induced by suction bucket installation on sand via centrifuge model tests ». In : *Marine Georesources & Geotechnology* 38.10 (2020), p. 1245-1256 (cf. p. 37).

[32] J. H. KIM, S. T. LEE and D. S. KIM. « Observation of sand movement during bucket installation ». In : *International Journal of Physical Modelling in Geotechnics* 19.1 (2019), p. 1-14 (cf. p. 31, 35).

[33] T. KRÜGER, H. KUSUMAATMAJA, A. KUZMIN, O. SHARDT, G. SILVA and E. M. VIGGEN. « The lattice Boltzmann method ». In : *Springer International Publishing* 10.978-3 (2017), p. 4-15 (cf. p. 50-53, 55-58, 62).

[34] P. LALLEMAND and L.-S. LUO. « Lattice Boltzmann method for moving boundaries ». In : *Journal of Computational Physics* 184.2 (2003), p. 406-421 (cf. p. 60).

[35] S. LUDING. « Cohesive, frictional powders : contact models for tension ». In : *Granular Matter* 10.4 (2008), p. 235-246 (cf. p. 42-45, 47).

[36] Z. MA, D. LIU, B. LIU, Y. ZHANG and K. H. ANDERSEN. « Installation of suction bucket foundations in layered soils in Southern China ». In : *ISOPE International Ocean and Polar Engineering Conference*. ISOPE. 2022, ISOPE-I (cf. p. 24).

[37] F. MACKERETH. « A portable core sampler for lake deposits ». In : *Limnology and oceanography* 3.2 (1958), p. 181-191 (cf. p. 23).

[38] A. MOHAMAD. *Lattice boltzmann method*. T. 70. Springer, 2011 (cf. p. 57-59).

[39] D. R. NOBLE and J. TORCZYNSKI. « A lattice-Boltzmann method for partially saturated computational cells ». In : *International Journal of Modern Physics C* 9.08 (1998), p. 1189-1201 (cf. p. 60).

[40] F. RADJAI and F. DUBOIS. *Discrete-element modeling of granular materials*. Wiley-Iste, 2011 (cf. p. 48, 49, 90).

[41] R. RAGNI, B. BIENEN, S. STANIER, C. O'LOUGHLIN and M. CASSIDY. « Observations during suction bucket installation in sand ». In : *International Journal of Physical Modelling in Geotechnics* 20.3 (2020), p. 132-149 (cf. p. 22, 24, 25, 37).

[42] C. RETTINGER. « Fluid flow simulations using the lattice Boltzmann method with multiple relaxation times ». In : *Bachelor Thesis, Friedrich-Alexander-Universität Erlangen-Nürnberg, Germany* (2013) (cf. p. 51-54).

[43] C. RETTINGER and U. RUEDE. « A comparative study of fluid-particle coupling methods for fully resolved lattice Boltzmann simulations ». In : *Computers & Fluids* 154 (2017), p. 74-89 (cf. p. 108).

[44] M. SANAYEI. *PhD developments*. 2023. URL : https://github.com/atmpluss/msanayei_phd_developments (cf. p. 20, 64, 67, 69, 71, 74, 108).

[45] M. SANAYEI, A. FARHAT, L.-H. LUU, L. WERNER, C. RETTINGER, P. PHILIPPE and P. CUELLAR. « Micromechanical framework for a 3D solid cohesion model–implementation, validation and perspectives ». In : *Proceeding-VII International Conference on Particle-Based Methods PARTICLES 2021*. 2021, p. 1-10 (cf. p. 78).

[46] J. SHENG, Y. ZHANG, H. XU, Y. TENG, W. HUANG, H. YAN, B. REN and Y. SU. « Experience from installation of two suction bucket jacket foundations in layered soils ». In : *Marine Georesources & Geotechnology* 42.1 (2024), p. 47-58 (cf. p. 37).

[47] V. ŠMILAUER. « Cohesive particle model using discrete element method on the Yade platform ». Thèse de doct. Czech Technical University, 2010 (cf. p. 45).

[48] V. ŠMILAUER and B. CHAREYRE. « YADE DEM formulation ». In : *YADE Documentation* 393 (2010) (cf. p. 88, 107).

[49] SPTOFFSHORE. *sptoffshore*. URL : https://www.sptoffshore.com (visité le 07/01/2024) (cf. p. 22).

[50] D. STORTI and M. YURTOGLU. *CUDA for engineers: An introduction to high-performance parallel computing*. Addison-Wesley Professional, 2015 (cf. p. 66).

[51] J. M. TING and B. T. CORKUM. « Computational laboratory for discrete element geomechanics ». In : *Journal of Computing in Civil Engineering* 6.2 (1992), p. 129-146 (cf. p. 43).

[52] M. N. TRAN, D. W. AIREY and M. F. RANDOLPH. « Study of seepage flow and sand plug loosening in installation of suction caissons in sand ». In : *ISOPE International Ocean and Polar Engineering Conference*. ISOPE. 2005, ISOPE-I (cf. p. 23).

[53] M. N. TRAN. « Installation of Suction Caissons in Dense Sand and the Influence of Silt and Cemented Layers ». Thèse de doct. The University of Sydney, 2005 (cf. p. 19, 22-38, 111, 114).

[54] L. VERLET. « Computer" experiments" on classical fluids. I. Thermodynamical properties of Lennard-Jones molecules ». In : *Physical review* 159.1 (1967), p. 98 (cf. p. 68).

[55] M. WANG, K. DEMARS and V. NACCI. « Breakout capacity of model suction anchors in soil ». In : *Canadian Geotechnical Journal* 14.2 (1977), p. 246-257 (cf. p. 24).

[56] Y. WANG, F. ALONSO-MARROQUIN, S. XUE and J. XIE. « Revisiting rolling and sliding in two-dimensional discrete element models ». In : *Particuology* 18 (2015), p. 35-41 (cf. p. 44, 45).

[57] B. T. WEINSTEIN and M. C. FERNANDES. *Lattice Boltzmann Method*. 2020. URL : https://sites.google.com/site/latticeboltzmannmethodcs205/home/boundary-conditions (cf. p. 58).

[58] D. WHITE, W. TAKE and M. BOLTON. « Soil deformation measurement using particle image velocimetry (PIV) and photogrammetry ». In : *Geotechnique* 53.7 (2003), p. 619-631 (cf. p. 26).

[59] Y. WU, D. LI, Y. ZHANG and F. CHEN. « Determination of maximum penetration depth of suction caissons in sand ». In : *KSCE Journal of Civil Engineering* 22 (2018), p. 2776-2783 (cf. p. 25).

[60] Y. WU, Y. ZHANG and D. LI. « Solution to critical suction pressure of penetrating suction caissons into clay using limit analysis ». In : *Applied Ocean Research* 101 (2020), p. 102264 (cf. p. 25).

[61] L. ZDRAVKOVIC, D. POTTS and R. JARDINE. « A parametric study of the pull-out capacity of bucket foundations in soft clay ». In : *Géotechnique* 51.1 (2001), p. 55-67 (cf. p. 24).

[62] P. ZHANG, L. MU, Y. LU, M. HUANG and J. SUN. « Microscopic insights into suction bucket installation in sand : Coupled coarse-grained CFD-DEM simulations ». In : *Computers and Geotechnics* 167 (2024), p. 106060 (cf. p. 24, 37).

[63] Y. ZHANG, D. LI and Y. BAI. « Experimental studies on suction-assisted installation of the modified suction caisson in dense sand ». In : *Applied Ocean Research* 124 (2022), p. 103221 (cf. p. 25).

[64] C. ZHAO, A. A. LAVASAN, T. BARCIAGA, V. ZAREV, M. DATCHEVA and T. SCHANZ. « Model validation and calibration via back analysis for mechanized tunnel simulations–The Western Scheldt tunnel case ». In : *Computers and Geotechnics* 69 (2015), p. 601-614 (cf. p. 94).

[65] W. ZHOU, Z. GUO, L. WANG, Y. ZHANG and S. RUI. « Numerical model for suction caisson under axial cyclic loadings ». In : *Ocean Engineering* 240 (2021), p. 109956 (cf. p. 24).

[66] Q. ZOU and X. HE. « On pressure and velocity boundary conditions for the lattice Boltzmann BGK model ». In : *Physics of Fluids* 9.6 (1997), p. 1591-1598 (cf. p. 105).

Schriftenreihe des Instituts für Grundbau, Wasserwesen und Verkehrswesen der Ruhr-Universität Bochum

Herausgeber: H.L. Jessberger

1 (1979) **Hans Ludwig Jessberger**
Grundbau und Bodenmechanik an der Ruhr-Universität Bochum

2 (1978) **Joachim Klein**
Nichtlineares Kriechen von künstlich gefrorenem Emschermergel

3 (1979) **Heinz-Joachim Gödecke**
Die Dynamische Intensivverdichtung wenig wasserdurchlässiger Böden

4 (1979) **Poul V. Lade**
Three Dimensional Stress-Strain Behaviour and Modeling of Soils

5 (1979) **Roland Pusch**
Creep of soils

6 (1979) **Norbert Diekmann**
Zeitabhängiges, nichtlineares Spannungs-Verformungsverhalten von gefrorenem Schluff unter triaxialer Belastung

7 (1979) **Rudolf Dörr**
Zeitabhängiges Setzungsverhalten von Gründungen in Schnee, Firn und Eis der Antarktis am Beispiel der deutschen Georg-von-Neumayer- und Filchner-Station

8 (1984) **Ulrich Güttler**
Beurteilung des Steifigkeits- und Nachverdichtungsverhaltens von ungebundenen Mineralstoffen

9 (1986) **Peter Jordan**
Einfluss der Belastungsfrequenz und der partiellen Entwässerungs-möglichkeiten auf die Verflüssigung von Feinsand

10 (1986) **Eugen Makowski**
Modellierung der künstlichen Bodenvereisung im grundwasserdurchströmten Untergrund mit der Methode der finiten Elemente

11 (1986) **Reinhard A. Beine**
Verdichtungswirkung der Fallmasse auf Lastausbreitung in nichtbindigem Boden bei der Dynamischen Intensivverdichtung

12 (1986) **Wolfgang Ebel**
Einfluss des Spannungspfades auf das Spannungs-Verformungsverhalten von gefrorenem Schluff im Hinblick auf die Berechnung von Gefrierschächten

13 (1987) **Uwe Stoffers**
Berechnungen und Zentrifugen-Modellversuche zur Verformungsabhängigkeit der Ausbaubeanspruchung von Tunnelausbauten in Lockergestein

14 (1988) **Gerhard Thiel**
Steifigkeit und Dämpfung von wassergesättigtem Feinsand unter Erdbebenbelastung

15 (1991) **Mahmud Thaher**
Tragverhalten von Pfahl-Platten-Gründungen im bindigen Baugrund,
Berechnungsmodelle und Zentrifugen-Modellversuche

Schriftenreihe des Instituts für Grundbau der Ruhr-Universität Bochum

Herausgeber: H.L. Jessberger

16 (1992) **Rainer Scherbeck**
Geotechnisches Verhalten mineralischer Deponieabdichtungsschichten
bei ungleichförmiger Verformungswirkung

17 (1992) **Martin M. Bizialiele**
Torsional Cyclic Loading Response of a Single Pile in Sand

18 (1993) **Michael Kotthaus**
Zum Tragverhalten von horizontal belasteten Pfahlreihen aus langen Pfählen in Sand

19 (1993) **Ulrich Mann**
Stofftransport durch mineralische Deponieabdichtungen:
Versuchsmethodik und Berechnungsverfahren

20 (1992) **Festschrift anlässlich des 60. Geburtstages von**
Prof. Dr.-Ing. H. L. Jessberger
20 Jahre Grundbau und Bodenmechanik an der Ruhr-Universität Bochum

21 (1993) **Stephan Demmert**
Analyse des Emissionsverhaltens einer Kombinationsabdichtung im Rahmen der
Risikobetrachtung von Abfalldeponien

22 (1994) **Diethard König**
Beanspruchung von Tunnel- und Schachtausbauten in kohäsionslosem Lockergestein
unter Berücksichtigung der Verformung im Boden

23 (1995) **Thomas Neteler**
Bewertungsmodell für die nutzungsbezogene Auswahl von Verfahren zur Altlastensanierung

24 (1995) **Ralph Kockel**
Scherfestigkeit von Mischabfall im Hinblick auf die Standsicherheit von Deponien

25 (1996) **Jan Laue**
Zur Setzung von Flachfundamenten auf Sand unter wiederholten Lastereignissen

26 (1996) **Gunnar Heibrock**
Zur Rissbildung durch Austrocknung in mineralischen Abdichtungsschichten
an der Basis von Deponien

27 (1996) **Thomas Siemer**
Zentrifugen-Modellversuche zur dynamischen Wechselwirkung zwischen Bauwerken
und Baugrund infolge stoßartiger Belastung

28 (1996) **Viswanadham V. S. Bhamidipati**
Geosynthetic Reinforced Mineral Sealing Layers of Landfills

29 (1997) **Frank Trappmann**
Abschätzung von technischem Risiko und Energiebedarf bei Sanierungsmaßnahmen für Altlasten

30 (1997) **André Schürmann**
Zum Erddruck auf unverankerte flexible Verbauwände

31 (1997) **Jessberger, H. L. (Herausgeber)**
Environment Geotechnics, Report of ISSMGE Technical Committee TC 5 on Environmental Geotechnics

Schriftenreihe des Instituts für Grundbau und Bodenmechanik der Ruhr-Universität Bochum

Herausgeber: Th. Triantafyllidis

32 (2000) **Triantafyllidis, Th. (Herausgeber)**
Boden unter fast zyklischer Belastung: Erfahrung und Forschungsergebnisse (Workshop)

33 (2002) **Christof Gehle**
Bruch- und Scherverhalten von Gesteinstrennflächen mit dazwischenliegenden Materialbrücken

34 (2003) **Andrzej Niemunis**
Extended hypoplastic models for soils

35 (2004) **Christiane Hof**
Über das Verpressankertragverhalten unter kalklösendem Kohlensäureangriff

36 (2004) **René Schäfer**
Einfluss der Herstellungsmethode auf das Verformungsverhalten von Schlitzwänden in weichen bindigen Böden

37 (2005) **Henning Wolf**
Zur Scherfugenbänderung granularer Materialien unter Extensionsbeanspruchung

38 (2005) **Torsten Wichtmann**
Explicit accumulation model for non-cohesive soils under cyclic loading

39 (2008) **Christoph M. Loreck**
Die Entwicklung des Frischbetondruckes bei der Herstellung von Schlitzwänden

40 (2008) **Igor Arsic**
Über die Bettung von Rohrleitungen in Flüssigböden

41 (2009) **Anna Arwanitaki**
Über das Kontaktverhalten zwischen einer Zweiphasenschlitzwand und nichtbindigen Böden

Schriftenreihe des Lehrstuhls für Grundbau, Boden- und Felsmechanik der Ruhr-Universität Bochum

Herausgeber: T. Schanz

42 (2009) **Yvonne Lins**
Hydro-Mechanical Properties of Partially Saturated Sand

43 (2010) **Tom Schanz (Herausgeber)**
Geotechnische Herausforderungen beim Umbau des Emscher-Systems
Beiträge zum RuhrGeo Tag 2010

44 (2010) **Jamal Alabdullah**
Testing Unsaturated Soil for Plane Strain Conditions: A New Double-Wall Biaxial Device

45 (2011) **Lars Röchter**
Systeme paralleler Scherbänder unter Extension im ebenen Verformungszustand

46 (2011) **Yasir Al-Badran**
Volumetric Yielding Behavior of Unsaturated Fine-Grained Soils

47 (2011) **Usque ad finem**
Selected research papers

48 (2012) **Muhammad Ibrar Khan**
Hydraulic Conductivity of Moderate and Highly Dense Expansive Clays

49 (2014) **Long Nguyen-Tuan**
Coupled Thermo-Hydro-Mechanical Analysis: Experimental and Back Analysis

50 (2014) **Tom Schanz (Herausgeber)**
Ende des Steinkohlenbergbaus im Ruhrrevier: Realität und Perspektiven für die Geotechnik
Beiträge zum RuhrGeo Tag 2014

51 (2014) **Usque ad finem**
Selected research papers

52 (2014) **Houman Soleimani Fard**
Study on the Hydro-Mechanical Behavior of Fiber Reinforced Fine Grained Soils,
with Application to the Preservation of Historical Monuments

53 (2014) **Wiebke Baille**
Hydro-Mechanical Behaviour of Clays - Significance of Mineralogy

54 (2014) **Qasim Abdulkarem Jassim Al-Obaidi**
Hydro-Mechanical Behavior of Collapsible Soils

55 (2015) **Veselin Zarev**
Model Identification for the Adaption of Numerical Simulation Models -
Application to Mechanized Shield Tunneling

56 (2015) **Meisam Goudarzy**
Micro and Macro Mechanical Assessment of Small and Intermediate Strain
Properties of Granular Material

57 (2016) **Oliver Detert**
Analyse einer selbstregulierenden interaktiven Membrangründung für Schüttkörper auf geringtragfähigen Böden

58 (2016) **Yang Yang**
Analyses of Heat Transfer and Temperature-induced Behaviour in Geotechnics

59 (2016) **Alborz Pourzargar**
Application of suction stress concept to partially saturated compacted soils

60 (2017) **Hanna Haase**
Multiscale Analysis of Clay-Polymer Composites for Geoenvironmental Applications

61 (2017) **Kavan Khaledi**
Constitutive modeling of rock salt with application to energy storage caverns

62 (2017) **Nina Silvia Müthing**
On the consolidation behaviour of fine-grained soils under cyclic loading

63 (2017) **Elham Mahmoudi**
Probabilistic analysis of a rock salt cavern with application to energy storage systems

64 (2017) **Negar Rahemi**
Evaluation of liquefaction behavior of sandy soils using critical state soil mechanics and instability concept

65 (2018) **Chenyang Zhao**
Numerical Modeling of Mechanized Tunnel Excavation:
Effects of Sub-systems and Advanced Process Simulation

66 (2018) **Tom Schanz (Herausgeber)**
Innovationen im Spezialtiefbau und in der Umweltgeotechnik
Beiträge zum RuhrGeo Tag 2018

67 (2019) **Linzhi Lang**
Hydro-Mechanical Behaviour of Bentonite-Based Materials Used for Disposal of Radioactive Wastes

68 (2019) **Usama Al-Anbaki**
Hydraulic Interaction of Soil and Nonwoven Geotextiles under Unsaturated Conditions

69 (2019) **Abhishek Rawat**
Coupled Hydro-mechanical Behavior of a Compacted Bentonite-Sand Mixture: Experimental and Numerical Investigations

Schriftenreihe des Lehrstuhls für Bodenmechanik, Grundbau und Umweltgeotechnik der Ruhr-Universität Bochum

Herausgeber: T. Wichtmann

70 (2019) **Mahmoud Qarmout**
Tunnel face stability using Kinematical Element Method (KEM)

71 (2021) **Raoul Hölter**
Optimal Experimental Design in Geotechnical Engineering

72 (2022) **Wolfgang Lieske**
Impact of polymer constitution on the hydro-mechanical behaviour of modified bentonite for the application in geotechnical and geoenvironmental engineering

73 (2022) **Patrick Staubach**
Contributions to the numerical modelling of pile installation processes and high-cyclic loading of soils

74 (2022) **Lingyun Li**
On the hydromechanical behaviour of loess and its effect on slope stability under rainfall infiltration

75 (2022) **Debdeep Sarkar**
Influence of particle characteristics on the behaviour of granular materials under static, cyclic and dynamic loading

76 (2023) **Torsten Wichtmann (Herausgeber)**
Umbau des Emscher-Systems – Geotechnische Erfahrungen
Beiträge zum RuhrGeo Tag 2023

77 (2023) **Abbas Farhat**
Fluidization and erosion of cemented granular materials. Experimental characterization and micromechanical simulation

78 (2023) **Andrea Geppetti**
Experimental and numerical investigations on the behaviour of tailing storage facilities under seismic loading

79 (2023) **Mohammad Hassan Sanayei**
Micromechanical modelling for the analysis of piping erosion in cemented soils for suction-assisted offshore foundations